

Precision spectroscopy with trapped $^{40}\text{Ca}^+$ and $^{27}\text{Al}^+$ ions

Dissertation, submitted to the
Faculty of Mathematics, Computer Science and Physics
of the Leopold-Franzens University of Innsbruck
in partial fulfillment
of the requirements for the degree of

Doctor of Philosophy
(Physics)

by

Dipl.-Phys. Michael Guggemos

Innsbruck, February 2017

Abstract

This thesis reports on setting up from scratch a new experimental apparatus with trapped $^{27}\text{Al}^+$ and $^{40}\text{Ca}^+$ ions, including the ion trap and all relevant laser systems for precision spectroscopy. Laser ablation loading of both ion species was implemented and in addition their sympathetic cooling dynamics were investigated. Second, systematic frequency shifts, especially the electric quadrupole shift along $^{40}\text{Ca}^+$ ion strings were calibrated with sub-Hertz resolution by carrying out Ramsey experiments with Ramsey times orders of magnitude longer than the single ion coherence time, correlating the results and evaluating the obtained parity oscillations. Third, the absolute frequency of the $^1\text{S}_0 \leftrightarrow ^3\text{P}_1$, $F = 7/2$ transition in $^{27}\text{Al}^+$ and the Landé g-factor of the excited state $g_{^3\text{P}_1 F=7/2}$ were measured using Ramsey's method of separated fields by quantum logic spectroscopy with a $^{40}\text{Ca}^+$ ion whose $\text{S}_{1/2} \leftrightarrow \text{D}_{5/2}$ electric quadrupole transition was used as a frequency reference. Finally the $^1\text{S}_0 \leftrightarrow ^3\text{P}_0$ clock transition in $^{27}\text{Al}^+$ was observed.

Zusammenfassung

Diese Arbeit berichtet vom Aufbau eines neuen Ionenfallenexperiments inklusive aller relevanten Lasersysteme für die Präzisionsspektroskopie an gespeicherten $^{27}\text{Al}^+$ und $^{40}\text{Ca}^+$ Ionen. Ionen beider Spezies wurden mittels Laser-Ablation geladen und deren mitführendes Kühlverhalten wurde untersucht. Des Weiteren wurden systematische Frequenzverschiebungen, speziell die elektrische Quadrupolverschiebung entlang einer Kette von gefangenen $^{40}\text{Ca}^+$ Ionen mit sub-Hertz Auflösung gemessen. Dazu wurden Ramsey Experimente mit um Größenordnungen längeren Wechselwirkungszeiten als die Kohärenzzeit des einzelnen Ions durchgeführt. Oszillationen des Paritätssignals geben Aufschluss über den Unterschied in den Übergangsfrequenzen der einzelnen Ionen. Darüber hinaus wurde die absolute Frequenz des $^1\text{S}_0 \leftrightarrow ^3\text{P}_1, F = 7/2$ Übergangs in $^{27}\text{Al}^+$ Ionen sowie der Landé g-Faktor des oberen Zustands $g_{^3\text{P}_1, F=7/2}$ mittels Ramsey Spektroskopie bestimmt. Die elektronische Besetzung im Aluminiumion wurde durch Quantenlogik mit einem $^{40}\text{Ca}^+$ Ion nachgewiesen, dessen $\text{S}_{1/2} \leftrightarrow \text{D}_{5/2}$ Quadrupolübergang als Frequenzreferenz diente. Schließlich wurde der $^1\text{S}_0 \leftrightarrow ^3\text{P}_0$ Uhrenübergang im $^{27}\text{Al}^+$ Ion beobachtet.

Contents

Abstract	i
Zusammenfassung	ii
1 Introduction	1
2 Ion trapping fundamentals & theoretical framework	4
2.1 Operation principle of a linear ion trap	4
2.2 Mixed Coulomb ion crystals	6
2.3 Interaction of trapped ions with lasers	10
2.3.1 Interaction of a free two level atom with monochromatic light	10
2.3.2 Quantum mechanical harmonic oscillator	11
2.3.3 Combined system	11
2.3.4 Off-resonant light field	13
2.3.5 Dissipation & decoherence	14
2.3.6 The Bloch sphere	15
2.3.7 Ramsey experiment	16
3 Level structure and radiative transitions in $^{40}\text{Ca}^+$ and $^{27}\text{Al}^+$ ions	18
3.1 Level structure and radiative transitions of $^{40}\text{Ca}^+$	18
3.1.1 Dipole transitions	19
3.1.2 Quadrupole transitions	20
3.2 Level structure and radiative transitions of $^{27}\text{Al}^+$	22
3.2.1 The $^1\text{S}_0 \leftrightarrow ^3\text{P}_1$ intercombination line	23
3.2.2 The hyperfine induced $^1\text{S}_0 \leftrightarrow ^3\text{P}_0$ clock transition	25
3.2.3 Nuclear spin flips	27
4 Experimental setup	29
4.1 Ion trap setup	29
4.1.1 Linear Paul trap	30
4.1.2 Vacuum vessel	34
4.1.3 Magnetic field shielding	37

4.1.4	Imaging system & state detection	38
4.2	Laser systems	40
4.2.1	Lasers for Doppler-cooling, repumping, and photo-ionization	40
4.2.2	Wavelength meter & wavelength control	45
4.2.3	Ultra-stable lasers	47
4.2.4	Frequency comb	61
4.3	Experimental control	68
5	Experimental techniques	70
5.1	Laser ablation loading of ions	70
5.2	Experimental sequence	75
5.3	Locking the 729 nm Laser to the S-D transition	81
5.4	Micromotion compensation	81
5.5	Quantum logic spectroscopy	84
6	Measurements	86
6.1	Sympathetic cooling	86
6.2	Ramsey correlation spectroscopy	91
6.3	Precision spectroscopy on the $^1\text{S}_0 \leftrightarrow ^3\text{P}_1$, $F = 7/2$ transition	99
6.4	Observation of the $^1\text{S}_0 \leftrightarrow ^3\text{P}_0$ clock transition	107
7	Summary and outlook	109
A	Appendix	111
B	Journal publications	112
	Acknowledgements	120

1 Introduction

Thousands of years ago mankind started to observe time based on regular periodic phenomena in nature. Monuments like Stonehenge and devices like the sky disk of Nebra allowed for the observation and prediction of equinoxes and solstices, respectively which was important for early agriculture.

The progression of civilization and the need of synchronizing social events required the observation of time on shorter scales. This led to the development of sundials [1]. The frequency ratio of the earth's orbit and the phases of the moon led to the division of the daylight into twelve parts [1]. However, there are some impractical characteristics of sundials. The length of one hour changes with the latitude of the observer and depends on the season. Moreover sundials simply don't work at night and cloudy days. Other approaches to measure time like water clocks and sandglasses overcame this problem by tracking time based on a constant flow rate.

Development in metal processing led to the invention of pendulum clocks by Christiaan Huygens in 1656, which were the first clocks containing an intrinsic oscillator. Each oscillation period of these pendula corresponds to a temporal period of one second. However, since their oscillation frequency depends on the acceleration, acting on the pendulum, which is not constant on a wavering ship, these clocks turned out to be not accurate enough for nautical navigation. The use of a spring-based oscillator solved this problem.

With the development of electronics and the discovery of the piezo-electric effect [2] at the end of the 19th century quartz clocks came up. With a higher clock speed and independence from external perturbations quartz clocks led to an improvement of one order of magnitude in time keeping with respect to the best pendulum clocks [1]. However, quartz crystals have never identical natural frequencies and in addition they age, resulting in long term frequency drifts.

The idea of using atomic systems for time keeping was conceived in the middle of the 20th century. The first concept of an atomic clock was devised in 1945 by I. I. Rabi [3,4]. It makes use of two atomic energy levels that are coupled by electromagnetic radiation at their resonance frequency which denotes the oscillator. Atoms of the same kind have identical properties (to the current status of knowledge), allowing identical atomic clocks to be built anywhere. The current definition of the second is based on cesium fountain clocks using Ramsey's method of separated fields [5]:

The second is the duration of 9 192 631 770 periods of radiation corresponding to the transition between the two hyperfine levels of the ground state of the cesium 133 atom.

The performance of a clock is characterized by two properties, accuracy and stability. Accuracy is the degree of conformity of the measured time to its definition, which is related to an offset from the ideal value. It depends on the perturbability of the clock. Stability indicates how well an oscillator can produce the same frequency over a given period of time τ and is characterized by the Allan deviation. The instability of a shot-noise limited atomic clock is expressed by [6]

$$\sigma_y(\tau) \sim \frac{1}{\pi Q} \sqrt{\frac{T_c}{N\tau}} \quad (1.1)$$

where T_c is the interrogation time, $Q = \nu_0/\Delta\nu_{FWHM}$ the quality factor as the ratio between oscillation frequency and the spectral width of the atomic transition, N the number of atoms (shot noise) and τ the measurement time. Reduction of Doppler-shifts by laser cooling enable current cesium fountain clocks [7] to reach fractional frequency instabilities in the low 10^{-16} range. From equation 1.1 it can be seen that this can be improved using spectrally narrow transitions with higher frequency.

The invention of optical frequency combs [8] facilitated direct frequency measurements in the optical domain substantially and so optical atomic clocks became a logical consequence. The frequency comb down-converts optical frequencies to the radio frequency domain where they can be handled and distributed by common electronics. Over the last years huge progress was made with optical clocks based on trapped ions [9] and neutral atoms captured in optical lattices [10], which nowadays outperform the cesium fountain clocks by two orders of magnitude in terms of stability and accuracy [9, 10]. Currently the most stable clock is based on neutral strontium atoms in an optical lattice [10]. The stability of these clocks benefits from a high number of atoms that can be investigated simultaneously. However, the accuracy of these clocks suffers from drifting systematic shifts, especially the AC Stark shift resulting from black-body radiation.

Contrary to that, aluminium ions feature a clock transition around 1.121 PHz that is extremely robust to external perturbations which makes it well suited for time keeping, especially in noisy environments. Single ion aluminium clocks already reached amazing stability and accuracy almost a decade ago. The fractional inaccuracy of $8.6 \cdot 10^{-18}$ measured in ref. [9] is limited primarily by uncertainties in the second order Doppler-shift, which could be recently reduced by a factor of 50 [11]. It was proposed that a quantum network of clocks based on aluminium ions has the potential to reach the 10^{-20} level [12]. The only drawback of aluminium ions is that they lack a practical closed transition for Doppler-cooling and state detection. This problem can be overcome by simultaneously trapping another species that

can be directly cooled. So far beryllium and magnesium ions were used as logic ions [9]. The use of $^{40}\text{Ca}^+$ ions as logic ions is advantageous as better cooling results due to a narrower linewidth of the cooling transition and its similar mass to $^{27}\text{Al}^+$ can be achieved [13], reducing the uncertainty in the second order Doppler-shift. A detailed comparison of advantages and disadvantages of relevant atomic and ionic species under investigation for an optical frequency standard can be found in [14].

There are plenty of useful applications for ultra precise clocks. Besides for time keeping, frequency measurements can be used for a more accurate definition of other physical units. Furthermore the resolution of positioning systems like GPS and GALILEO rely on the performance of atomic clocks. Research in the field of general relativity benefited from that progress since a gravitational red-shift from an elevation difference of only 30 cm could be observed by recent clock comparisons [15] and also relativistic time dilatation of ions experiencing different excess micromotion was investigated [15]. The test of fundamental theories and the investigation of the variation of fundamental constants like the fine structure constant [16] are probed by comparing transition frequencies of different atomic species over a long period of time. Furthermore, more precise synchronization of radio telescopes increases the resolution of telescope arrays and interferometric measurements on large baselines which opens up new possibilities in astrophysics.

All these interesting applications and a collaboration with the European Space Agency (ESA) initiated the work on an optical frequency standard in the group of Rainer Blatt in Innsbruck. The key focus of research in the group is on quantum computation and quantum information processing with trapped $^{40}\text{Ca}^+$ ions. Key techniques developed in that context allow one to detect the internal state of the $^{27}\text{Al}^+$ ion via quantum logic spectroscopy (QLS) and can enhance the performance of trapped-ion clocks by deterministic creation of entanglement.

This work lays the foundation of a frequency standard based on trapped $^{27}\text{Al}^+$ and $^{40}\text{Ca}^+$ ions. The thesis is structured as follows. Chapter 2 gives a short theoretical description of all relevant phenomena of trapped ions interacting with light fields. Chapter 3 focuses on the atomic properties of both ion species and the relevant transitions used in this work. A detailed description of the experimental setup that was built can be found in chapter 4. Chapter 5 presents fundamental experimental techniques in ion trapping experiments. The experimental results of this work are presented in chapter 6. Chapter seven concludes the thesis.

2 Ion trapping fundamentals & theoretical framework

This section describes the confinement generated by a linear Paul trap and the resulting classical motion of a charged particle in the potential [17]. Later, the discussion will be extended to describe the collective motion of ions in a mixed ion crystal [18].

2.1 Operation principle of a linear ion trap

A standard linear Paul trap consists of six electrodes, four radial and two axial ones. Respectively two opposing electrodes are kept on the same potential. A schematic drawing of a standard linear Paul trap is presented in figure 2.1.

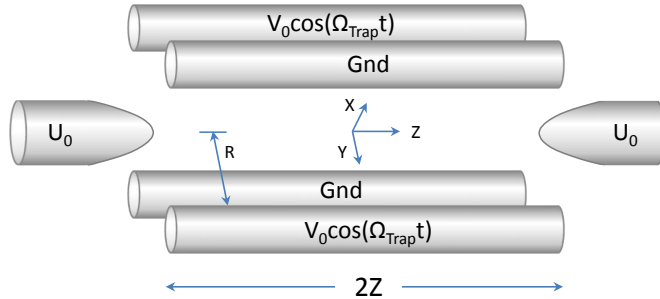


Figure 2.1: Schematic drawing of a standard linear Paul trap.

The radial confinement is created by four cylindrical electrodes. One pair is grounded while a radio frequency (RF) voltage $V = V_0 \cos(\Omega_{Trap} t)$ is applied to the other one. The resulting potential at the center of the trap is expressed by [17]

$$V(x, y, z, t) = \frac{V_0}{2} \left(1 + \frac{\kappa_{rad}(x^2 - y^2)}{R^2} \right) \cos(\Omega_{trap} t) \quad (2.1)$$

with R being the distance from the trap center to the electrodes. $\kappa_{rad} \approx 1$ is a geometrical factor that accounts for the shape of the electrodes (hyperbolic electrodes have $\kappa_{rad} = 1$). At any position off the z axis ($x, y \neq 0$), a charged particle experiences a force $F(x, y, t)$ from

the corresponding electric field. Over one radio frequency period the mean ion position hardly changes and the force averages to $\langle F(x, y) \rangle$. The related pseudopotential well [17] can be calculated by integration $\Phi_{ps} = -\int \langle F(x, y) \rangle$ to

$$\Phi_{ps} = \frac{QV_0^2}{4MR^2\Omega_{trap}^2}, \quad (2.2)$$

where M is the mass and Q the charge of the particle. The axial confinement is created by two endcap electrodes on the trap axis which are kept on a static voltage U_0 . The distance between the endcaps ($2Z$) is the same as the length of the radial electrodes. The resulting static potential is given by

$$U(x, y, z) = \frac{\kappa_{ax}U_0}{Z^2} \left(z^2 - \frac{1}{2}(x^2 + y^2) \right). \quad (2.3)$$

A further geometrical factor $\kappa_{ax} < 1$ accounts for the shape of the endcap electrodes. The motion of a trapped particle in the combined static and RF potential is described by the Mathieu equations

$$\frac{d^2x_i}{dt^2} + \frac{\Omega_{Trap}^2}{4}(a_i + 2q_i\cos(\Omega_{Trap}t))x_i = 0 \quad (2.4)$$

using the dimensionless parameters a_i and q_i which are defined as $a_{x,y} = -a_z/2 = -\frac{4Q\kappa_{ax}U_0}{MZ^2\Omega_{trap}^2}$ and $q_x = -q_y = \frac{2Q\kappa_{rad}V_0}{MR^2\Omega_{trap}^2}$, $q_z = 0$. Stable ion trapping is possible, if the trajectories in all three directions are confined. Parameters that lead to stable solutions are depicted in a stability diagram [17, 19]. Finally the equation of motion can be approximated by

$$x_i(t) \approx A_i\cos(\omega_i t + \varphi_i) \left(1 + \frac{q_i}{2}\cos(\Omega_{Trap}t) \right) \quad (2.5)$$

with the amplitude A_i and phase φ_i depending on the initial conditions. The motion of the particle can be separated in two parts. A harmonic oscillation at frequencies

$$\omega_{x,y} = \frac{1}{2}\Omega_{Trap}\sqrt{a_i + \frac{1}{2}q_i^2} \quad \text{and} \quad \omega_z = \sqrt{\frac{\kappa_{ax}QU_0}{8MZ^2}} \quad (2.6)$$

which is called secular motion and the driven motion due to the trapping field at frequency Ω_{trap} , called micromotion. Additional electric stray fields at the trap can shift the static part of the potential. As a consequence RF and DC null do not necessarily overlap which gives rise to excess micromotion.

2.2 Mixed Coulomb ion crystals

As soon as more ions are confined in the trap, the Coulomb repulsion between the ions needs to be considered. When the kinetic energy of the ions becomes small compared to the Coulomb energy, regular structures are formed which are known as ion crystals. The ions align themselves such that their potential energy is minimum [20]. For sufficiently cold temperatures the ions' motion can be described as a set of collective motional modes around their equilibrium positions [20]. A detailed description of the problem for ions of the same kind can be found in [20]. In order to determine the equilibrium positions and mode frequencies of a mixed ion string the equations derived in [20] need to be generalized for different ion masses. According to [18, 21] this can be done in the following way.

The potential energy of a mixed N-ion string in a static harmonic potential is given by

$$V = \sum_{i=1}^N \sum_{\alpha=x,y,z} \frac{1}{2} m_i \omega_{i,\alpha}^2 r_{i,\alpha}^2 + \sum_{n=1}^N \sum_{m \neq n} \frac{1}{2} \frac{Z^2 e^2}{4\pi\epsilon_0} \frac{1}{|\mathbf{r}_m - \mathbf{r}_n|} \quad (2.7)$$

where m_n is the mass of the n^{th} ion and $\omega_{n,\alpha}$ its oscillation frequency along the direction α . All ions are assumed to have the same charge Z . Introducing the length scale $l^3 = \frac{Z^2 e^2}{4\pi\epsilon_0 m_0 \omega_0^2}$ with the mass m_0 and the oscillation frequency ω_0 of a reference ion ($^{40}\text{Ca}^+$ in this work), allows one to rewrite the potential energy in a dimensionless form

$$V = \frac{1}{2} m_0 l^2 \left(\sum_{i,\alpha} \mu_i \omega_{i,\alpha}^2 \rho_{i,\alpha}^2 + \omega_0^2 \sum_{\substack{n,m \\ n \neq m}} \frac{1}{|\boldsymbol{\rho}_m - \boldsymbol{\rho}_n|} \right) \quad (2.8)$$

with $\rho_i = r_i/l$ and $\mu_i = \frac{m_i}{m_0}$. In the case of a linear ion string the coordinates in the transverse directions are zero ($\rho_{i,x} = \rho_{i,y} = 0$). With the definition $u_i \equiv \rho_{i,z}$ the expression for the equilibrium positions u_i^0 of the ions is given by

$$\begin{aligned} \left. \frac{\partial V}{\partial u_i} \right|_{u_i=u_i^0} = 0 &\iff c_i u_i^0 + \frac{d}{du_i} \sum_{\substack{n \\ n \neq i}} \frac{1}{|u_i - u_n|} \Big|_{u_i=u_i^0} = 0 \\ &\iff c_i u_i - \sum_{n < i} \frac{1}{(u_i^0 - u_n^0)^2} + \sum_{n > i} \frac{1}{(u_i^0 - u_n^0)^2} = 0 \end{aligned} \quad (2.9)$$

with $c_i = \mu_i \left(\frac{\omega_{i,z}}{\omega_0}\right)^2$. This expression can be solved by numerical solvers for nonlinear equations. For two singly charged ions in a static harmonic potential the equilibrium positions are $u_2 = -u_1 = 2^{-\frac{2}{3}}$ and the equilibrium distance is

$$d = \left(\frac{e^2}{2\pi\epsilon_0 m_0 \omega_0^2} \right)^{\frac{1}{3}}. \quad (2.10)$$

The calculation of the motional modes of a mixed ion crystal starts with the Lagrangian, which contains the kinetic and potential energy terms $L = T - V$, and is given by

$$L = \frac{1}{2} \sum_{i,\alpha} m_i \dot{r}_i^2 - V(r_{i,\alpha}) = \frac{1}{2} m_0 l^2 \left[\sum_{i,\alpha} \mu_i \dot{\rho}_{i,\alpha}^2 - \omega_0^2 \left(\sum_{i,\alpha} c_{i,\alpha} \rho_{i,\alpha}^2 + \sum_{\substack{n,m \\ n \neq m}} \frac{1}{|\rho_m - \rho_n|} \right) \right]. \quad (2.11)$$

Approximating the Lagrangian to second order around the equilibrium positions $\rho_m^0 = (0, 0, u_m^0)$ determined above, and rewriting the ion positions as $\rho_m = (q_{mx}, q_{my}, u_m^0 + q_{mz})$ the Lagrangian can be decomposed as $L = L_x + L_y + L_z$ where

$$L_z = \frac{1}{2} m_0 l^2 \left[\sum_i \mu_i \dot{q}_{i,z}^2 - \sum_i \mu_i \omega_{i,z}^2 q_{i,z}^2 - \frac{\omega_0^2}{2} \sum_{i,j} q_{i,z} q_{j,z} \frac{\partial}{\partial q_{i,z}} \frac{\partial}{\partial q_{j,z}} \sum_{\substack{n,m \\ n \neq m}} \frac{1}{|\rho_m - \rho_n|} \Big|_{q_i=0} \right]. \quad (2.12)$$

The expressions for L_x and L_y are similar. Note that a constant offset was subtracted from L . The term $S = \frac{1}{2} \sum_{i,j} q_{i,z} q_{j,z} \frac{\partial}{\partial q_{i,z}} \frac{\partial}{\partial q_{j,z}} \sum_{\substack{n,m \\ n \neq m}} \frac{1}{|\rho_m - \rho_n|} \Big|_{q_i=0}$ can be split into two parts for $i = j$ and $i \neq j$ and yields

$$\begin{aligned} S &= \frac{1}{2} \sum_i q_{i,z}^2 \sum_{\substack{n,m \\ n \neq m}} \frac{2}{|u_m^0 - u_n^0|^3} (\delta_{n,i} + \delta_{m,i}) + \frac{1}{2} \sum_{\substack{i,j \\ i \neq j}} q_{i,z} q_{j,z} \sum_{\substack{n,m \\ n \neq m}} \frac{2}{|u_m^0 - u_n^0|^3} (\delta_{n,i} \delta_{m,j} + \delta_{n,j} \delta_{m,i}) \\ &= \sum_n q_{n,z}^2 \left(\sum_{n \neq m} \frac{2}{|u_m^0 - u_n^0|^3} \right) + \sum_{\substack{n,m \\ n \neq m}} q_{n,z} q_{m,z} \left(\frac{-2}{|u_m^0 - u_n^0|^3} \right). \end{aligned} \quad (2.13)$$

The Lagrangian can be rewritten as [18, 21]

$$L_z = \frac{1}{2} m_0 l^2 \left[\sum_i \mu_i \dot{q}_{i,z}^2 - \sum_{i,j} A_{i,j}^z q_{i,z} q_{j,z} \right] \quad (2.14)$$

where $A_{i,j}^z$ is the coupling matrix (Hessian matrix)

$$A_{i,j}^z = \begin{cases} \mu_i \omega_{i,z}^2 + 2\omega_0^2 \sum_{n \neq i} \frac{1}{|u_i^0 - u_n^0|^3} & i = j \\ -2\omega_0^2 \sum_{n \neq i} \frac{1}{|u_i^0 - u_n^0|^3} & i \neq j. \end{cases} \quad (2.15)$$

Using mass weighted coordinates $\mathbf{q}' = M\mathbf{q}$ with $M_{ij} = \delta_{ij} \sqrt{\frac{m_i}{m_0}}$ the Lagrangian becomes

$$L_z = \frac{1}{2} m_0 l^2 \left[(\mathbf{q}'_z)^t \mathbf{q}'_z - (\mathbf{q}'_z)^t M^{-1} A^z M^{-1} \mathbf{q}'_z \right] \quad (2.16)$$

Inserting the Lagrangian into the Lagrangian equation of motion

$$\frac{d}{dt} \frac{\partial L}{\partial \dot{\mathbf{q}}_i} - \frac{\partial L}{\partial \mathbf{q}_i} = 0 \quad (2.17)$$

leads to the axial modes

$$\ddot{\mathbf{q}}'_z + M^{-1} A^z M^{-1} \mathbf{q}'_z = 0 \quad (2.18)$$

For ions with the same mass the expression reduces to the formula given in [20]. Introducing the symmetric matrix $\tilde{A}^z = M^{-1} A^z M^{-1}$ with its elements

$$\tilde{A}_{ij}^z = \frac{1}{\sqrt{\mu_i \mu_j}} A_{ij}^z = \begin{cases} \omega_{i,z}^2 + \frac{2\omega_0^2}{\mu_i} \sum_{n \neq i} \frac{1}{|u_i^0 - u_n^0|^3} & i = j \\ -\frac{2\omega_0^2}{\sqrt{\mu_i \mu_j}} \sum_{n \neq i} \frac{1}{|u_i^0 - u_n^0|^3} & i \neq j \end{cases} \quad (2.19)$$

the equations of motion become

$$\ddot{\mathbf{q}}'_z + \tilde{A}^z \mathbf{q}'_z = 0. \quad (2.20)$$

Solving the eigenvalue problem $\tilde{A}^z \mathbf{q}'_z = (\lambda^z)^2 \mathbf{q}'_z$ leads to the eigenfrequencies λ^z of the collective modes of motion. The transverse mode frequencies can be calculated by the same approach. The only difference is the second order derivative of the term describing the Coulomb interaction. The corresponding matrix elements are

$$A_{i,j}^x = \begin{cases} \mu_i \omega_{i,x}^2 - \omega_0^2 \sum_{n \neq i} \frac{1}{|u_i^0 - u_n^0|^3} & i = j \\ +\omega_0^2 \sum_{n \neq i} \frac{1}{|u_i^0 - u_n^0|^3} & i \neq j \end{cases} \quad (2.21)$$

that enter into the eigenvalue problem for the transverse mode frequencies λ^x and analogously for λ^y . A comprehensive description of mixed ion crystals can be found in [18].

The motion of a mixed two-ion crystal is described by six motional modes, one in-phase and one out-of-phase mode along the three trap axis. A detailed description of the normal modes

of a Ca^+/Al^+ ion crystal can be found in [13].

2.3 Interaction of trapped ions with lasers

The following section describes the interaction of an ion, confined in a trap, with laser radiation. First a free two-level atom is considered. Second, the confinement is taken into account by the description of the quantum mechanical harmonic oscillator. Subsequently, both Hamiltonians are added up to describe the combined system. Furthermore, carrier and sideband transitions are described as well as off-resonant laser-ion interactions. Next, a change to the density matrix formalism is made which allows one to account for dissipation and decoherence. Last, Ramsey's method of separate oscillatory fields is described.

2.3.1 Interaction of a free two level atom with monochromatic light

To describe the interaction of an atom with a laser field simplifications need to be made. In cases where the driving field is close to resonance to the transition between two atomic levels while other transitions are far detuned, the so called two-level atom is a good approximation to real systems. The Hamiltonian describing the bare atom is

$$\hat{\mathcal{H}}_a = \frac{\hbar\omega_0}{2}\hat{\sigma}_z \quad (2.22)$$

where $\hbar\omega_0$ denotes the energy difference between ground $|g\rangle=|\downarrow\rangle$ and excited $|e\rangle=|\uparrow\rangle$ state and $\hat{\sigma}_z$ is a Pauli spin operator. The perturbation by a classical light field close to resonance with frequency ω_l and phase ϕ_l is described by the Hamiltonian

$$\hat{\mathcal{H}}_l = \hbar\Omega\hat{\sigma}_x\cos(\omega_l t + \phi_l). \quad (2.23)$$

Resonant light leads to population oscillations between ground and excited state at a frequency Ω , known as the Rabi frequency whose strength is set by the electric field strength of the light field and the coupling matrix element of the atomic levels coupled by the light field (see section 3). The combined Hamiltonian $\hat{\mathcal{H}} = \hat{\mathcal{H}}_a + \hat{\mathcal{H}}_l$ is transferred to the interaction picture with respect to $\hat{\mathcal{H}}_a$ via $\hat{\mathcal{H}}_{int} = \hat{\mathcal{U}}_0^\dagger \hat{\mathcal{H}}_l \hat{\mathcal{U}}_0$ using the time evolution operator $\hat{\mathcal{U}}_0 = e^{-iH_a t/\hbar}$ [22]. After a rotating wave approximation, neglecting sum frequency terms, the interaction Hamiltonian denotes

$$\hat{\mathcal{H}}_{int} = \hbar\frac{\Omega}{2} (\cos((\omega_l - \omega_0)t + \phi_l)\hat{\sigma}_x + \sin((\omega_l - \omega_0)t + \phi_l)\hat{\sigma}_y). \quad (2.24)$$

After introducing the electronic raising and lowering operators $\hat{\sigma}_\pm = (\hat{\sigma}_x \pm i\hat{\sigma}_y)/2$ and substituting the detuning $(\omega_l - \omega_0) = \delta$, the Hamiltonian can be rewritten as:

$$\hat{\mathcal{H}}_{int} = \hbar\frac{\Omega}{2} (e^{-i(\delta t + \phi_l)}\hat{\sigma}_+ + e^{i(\delta t + \phi_l)}\hat{\sigma}_-) \quad (2.25)$$

This is the final expression for the interaction of a two-level atom with a laser.

2.3.2 Quantum mechanical harmonic oscillator

So far the position of the particle, interacting with a laser was assumed to be fixed. To account for the influence of the ion motion in the trap, the Hamiltonian for a quantum mechanical harmonic oscillator has to be added. For the sake of simplicity, a one dimensional quadratic potential is assumed.

$$\hat{\mathcal{H}}_{tr} = \frac{\hat{p}^2}{2m} + \frac{1}{2}m\omega_{tr}^2\hat{x}^2 \quad (2.26)$$

The Hamiltonian describes the total energy of a particle with mass m oscillating at a frequency $\omega_{tr}/2\pi$, where \hat{x} and \hat{p} denote position and momentum operators. It is useful to introduce the creation and annihilation operators [23]

$$\hat{a}^\dagger = \sqrt{\frac{m\omega_{tr}}{2\hbar}} \left(\hat{x} - \frac{i}{m\omega_{tr}}\hat{p} \right) \quad \text{and} \quad \hat{a} = \sqrt{\frac{m\omega_{tr}}{2\hbar}} \left(\hat{x} + \frac{i}{m\omega_{tr}}\hat{p} \right). \quad (2.27)$$

Hence the position and momentum operators can be represented as

$$\hat{x} = (\hat{a} + \hat{a}^\dagger)x_0 \quad \text{and} \quad \hat{p} = i(\hat{a}^\dagger - \hat{a})\frac{\hbar}{2x_0} \quad (2.28)$$

where $x_0 = \sqrt{\hbar/(2m\omega_{tr})}$ denotes the spatial extent of the ground state wave function. In terms of the creation and annihilation operators the Hamiltonian can be expressed as

$$\hat{\mathcal{H}}_{tr} = \hbar\omega_{tr}(\hat{a}^\dagger\hat{a} + \frac{1}{2}) = \hbar\omega_{tr}(\hat{n} + \frac{1}{2}). \quad (2.29)$$

The number operator \hat{n} has eigenstates $|n\rangle$ that correspond to the number of motional quanta (phonons) contained in the oscillator.

2.3.3 Combined system

In order to describe the interaction of a trapped two-level atom with a laser field equation (2.25) has to be modified with an additional term $e^{ik\hat{x}} = e^{i\eta(\hat{a}+\hat{a}^\dagger)}$ that accounts for the ion's position. The resulting Hamiltonian yields [24]

$$\hat{\mathcal{H}}_1 = \hbar\frac{\Omega}{2}(\hat{\sigma}_+ + \hat{\sigma}_-)(e^{i\eta(\hat{a}+\hat{a}^\dagger)}e^{-i(\delta t - \phi_l)} + e^{-i\eta(\hat{a}+\hat{a}^\dagger)}e^{i(\delta t - \phi_l)}) \quad (2.30)$$

with η being the Lamb-Dicke parameter. It is the product of the angular wavenumber of the laser field k with the spatial extent of the ion's ground state wave function and the angle between the laser and the direction of motion.

$$\eta = kx_0 \cos(\Theta) = k \sqrt{\frac{\hbar}{2m\omega_{tr}}} \cos(\Theta) \quad (2.31)$$

In the case of a mixed ion crystal (see section 2.2) the Lamb-Dicke parameter is given by

$$\eta_{i\alpha} = k \sqrt{\frac{\hbar}{2m_i\omega_\alpha}} V_{i,\alpha} \quad (2.32)$$

where $V_{i,\alpha}$ is the matrix element of the matrix V diagonalizing the matrix $A = VDV^\dagger$ (with $D = \tilde{A}^z$ or $D = \tilde{A}^x$). The elements $V_{i,\alpha}$, $i = 1, \dots, N$ are the normal mode contributions to the mass weighted coordinate vector \mathbf{q}' normalized to 1. A rotating wave approximation and transforming the Hamiltonian to the interaction picture with respect to the Hamiltonian of the unperturbed system $\hat{\mathcal{H}}_0 = \frac{\hbar\omega_0}{2} \hat{\sigma}_z + \hbar\omega_{tr}(\hat{a}^\dagger \hat{a} + \frac{1}{2})$ leads to:

$$\hat{\mathcal{H}}_{int} = \hbar\Omega(\hat{\sigma}_+ e^{i\eta(\hat{a}e^{-i\omega_l t} + \hat{a}^\dagger e^{i\omega_l t})} e^{-i(\delta t - \phi_l)} + h.c.) \quad (2.33)$$

If the extension of the wave function is small compared to the laser wavelength, the inequality $\eta^2(2\bar{n}+1) \ll 1$ holds, which is known as the Lamb-Dicke regime. In this regime the Hamiltonian can be Taylor-expanded to first order to

$$\hat{\mathcal{H}}_{int}(t) = \hbar\Omega\hat{\sigma}_+(1 + i\eta(\hat{a}e^{-i\omega t} + \hat{a}^\dagger e^{i\omega t}))e^{-i(\delta t - \phi_l)} + h.c.. \quad (2.34)$$

The approximation holds for transitions that change the motional state by zero or one quanta. The ion motion in the trap leads to an oscillating Doppler shift of the laser frequency. From the ion's point of view this translates into a frequency modulation of the laser. As a consequence sideband transitions show up that allow for manipulation of the ion's internal and motional state. Three different types of resonant transitions can be identified. The carrier transition only couples the internal states and leaves the motional state unchanged. Its Hamiltonian is given by:

$$\hat{\mathcal{H}}_{car} = \hbar \frac{\Omega_{n,n}}{2} \left(e^{i\phi_l} \hat{\sigma}_+ + e^{-i\phi_l} \hat{\sigma}_- \right). \quad (2.35)$$

Deep within the Lamb-Dicke regime, the coupling strength of the carrier transition is independent from its motional state. When considering up to second order in η the coupling strength scales as $\Omega_{n,n} = (1 - \eta^2 n)\Omega$. A process that changes the internal state and lowers the motional state by one quantum is called red sideband transition with the corresponding Hamiltonian

$$\hat{\mathcal{H}}_{rsb} = i\hbar\eta \frac{\Omega_{n,n-1}}{2} \left(e^{i\phi_l} \hat{a} \hat{\sigma}_+ - e^{-i\phi_l} \hat{a}^\dagger \hat{\sigma}_- \right). \quad (2.36)$$

The opposite process adds a phonon to the system and is called blue sideband transition and described by

$$\hat{\mathcal{H}}_{bsb} = i\hbar\eta\frac{\Omega_{n,n+1}}{2} \left(e^{i\phi_l}\hat{a}^\dagger\hat{\sigma}_+ - e^{-i\phi_l}\hat{a}\hat{\sigma}_- \right). \quad (2.37)$$

The coupling strengths on red and blue sideband transitions are $\Omega_{n-1,n} = \eta\sqrt{n}\Omega$ and $\Omega_{n,n+1} = \eta\sqrt{n+1}\Omega$ respectively. Comparing Rabi frequencies on carrier and sideband transitions allows one to extract the Lamb-Dicke parameter. Sideband transitions allow one to couple internal and external degrees of freedom and therefore enable:

1. Coupling of internal and external degrees of freedom
2. Frequency-resolved sideband cooling (see section 5.2)
3. Quantum logic spectroscopy (see section 5.5).

The mean phonon number can be determined by comparing the relative coupling strengths of red and blue sideband. Typically the ion's motional state after laser cooling is described by a thermal state with Fock state populations $p_n(\bar{n}) = \frac{1}{\bar{n}+1} \left(\frac{\bar{n}}{\bar{n}+1} \right)^n$. Thus carrier Rabi oscillations contain frequency components weighted by the thermal distribution.

$$|c_\uparrow|^2 = \sum_{n=0}^{\infty} p_n(\bar{n}) \sin^2 \left(\frac{\Omega_{n,n} t}{2} \right) \quad (2.38)$$

Consequently Rabi oscillations damp faster with increasing \bar{n} and the oscillation period becomes longer.

2.3.4 Off-resonant light field

As the light is tuned away from the atomic resonance Rabi oscillations become faster with a decreasing amplitude. The upper state population $|c_\uparrow|^2$ can be calculated by solving the optical Bloch equations [25]

$$|c_\uparrow|^2 = \frac{\Omega^2}{\Omega^2 + \delta^2} \sin^2 \left(\frac{1}{2} \sqrt{\Omega^2 + \delta^2} t \right). \quad (2.39)$$

For a large detuning $\delta \gg \Omega$ the population transfer is greatly suppressed, but the presence of the light field shifts the atomic energy levels, which is known as the AC-Stark effect. The perturbation causes new eigenenergies of the two-level atom. The AC-Stark shift of the transition is given by

$$\Delta_{Stark} = \frac{\Omega^2}{2\delta} \quad (2.40)$$

while the lower level is shifted by $-\Omega^2/4\delta$ and the upper level by $\Omega^2/4\delta$.

2.3.5 Dissipation & decoherence

So far the coherent interaction of a trapped two-level atom with a laser field was considered. In real quantum systems dissipation and decoherence are always present. Such effects stochastically change the quantum state. In the case of spontaneous emission the populations change due to a stochastic decay of the atom from the excited state to the ground state. Since the quantum system exchanges energy with the environment, it is said to be open. A quantitative treatment of open quantum systems is possible by the use of the density matrix formalism [25, 26]. The generalized form of the Schrödinger equation, the Von Neumann equation, is

$$\frac{d}{dt}\hat{\rho} = -\frac{i}{\hbar} [\hat{\mathcal{H}}, \hat{\rho}] \quad (2.41)$$

where $\hat{\rho} = \sum_i p_i |\psi_i\rangle \langle \psi_i|$ is the density matrix with probabilities p_i . Including dissipative processes described by a Liouvillian $\hat{\mathcal{L}}$ that takes into account system-environment interactions, the master equation becomes

$$\frac{d}{dt}\hat{\rho} = -\frac{i}{\hbar} [\hat{\mathcal{H}}, \hat{\rho}] + \hat{\mathcal{L}}\hat{\rho}. \quad (2.42)$$

Using the Lindblad notation [27], the Liouvillian describing spontaneous emission can be re-expressed in terms of the electronic raising and lowering operators as

$$\frac{d}{dt}\hat{\rho} = -\frac{i}{\hbar} [\hat{\mathcal{H}}, \hat{\rho}] - \frac{\Gamma}{2} [\hat{\rho}\hat{\sigma}_+\hat{\sigma}_- + \hat{\sigma}_+\hat{\sigma}_-\hat{\rho} - 2\hat{\sigma}_-\hat{\rho}\hat{\sigma}_+] \quad (2.43)$$

with the decay rate Γ of the excited state. The master equation of a coherently driven two level system including spontaneous emission can be explicitly written where energy conserving and dissipative terms are separated. The time dynamics of the density matrix elements for a two-level system ($|g\rangle, |e\rangle$) is given by the optical Bloch equations:

$$\dot{\rho}_{ee} = +\frac{i}{2}\Omega(\rho_{eg} - \rho_{ge}) - \Gamma\rho_{ee} \quad (2.44)$$

$$\dot{\rho}_{gg} = -\frac{i}{2}\Omega(\rho_{eg} - \rho_{ge}) + \Gamma\rho_{ee} \quad (2.45)$$

$$\dot{\rho}_{eg} = +\frac{i}{2}\Omega(\rho_{ee} - \rho_{gg}) + i\delta\rho_{eg} - (\Gamma/2)\rho_{eg} \quad (2.46)$$

$$\dot{\rho}_{ge} = -\frac{i}{2}\Omega(\rho_{ee} - \rho_{gg}) - i\delta\rho_{ge} - (\Gamma/2)\rho_{ge}. \quad (2.47)$$

An analytical expression describing the upper state population (with $|\rho_{ee}(t=0)|^2 = 0$) of a resonantly driven two level atom including dissipation is given by [26]

$$|\rho_{ee}(t)|^2 = \frac{\Gamma^2}{\Gamma^2 + 2\Omega^2} \left[1 - \frac{2\Omega^2}{\Gamma} e^{-(3\Gamma/4)t} \left\{ \cosh(\zeta t) + \frac{(3\Gamma/4)}{\zeta} \sinh(\zeta t) \right\} \right] \quad (2.48)$$

where $\zeta = \sqrt{(\Gamma/4)^2 - \Omega^2}$.

2.3.6 The Bloch sphere

To gain a graphical understanding of coherent operations on a two-level atom it is useful to introduce the Bloch sphere representation of the two-level system which is depicted in figure 2.2.

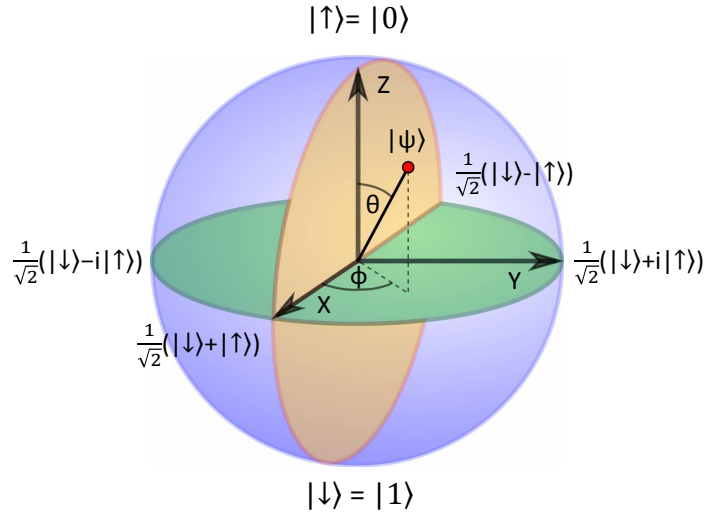


Figure 2.2: Bloch sphere representation of a two-level system. Any pure quantum state $|\psi\rangle = \alpha|\downarrow\rangle + \beta|\uparrow\rangle$ with $\alpha^2 + \beta^2 = 1$ can be represented as a vector (Bloch vector), pointing on the surface of a three dimensional unit sphere. Ground and excited state correspond to north and south pole of the sphere, respectively. Two pairs of orthogonal superposition states lie in the equatorial plane. Interior points correspond to mixed states.

Ground and excited state of the two-level system correspond to the north and the south pole of the sphere, respectively. Superposition states lie in the equatorial plane. Coherent manipulations of the two-level system are described by the Pauli matrices $(\sigma_x, \sigma_y, \sigma_z)$ [23, 25] and correspond to rotations of the Bloch vector around the corresponding coordinate axis. A laser pulse with $\Omega t = \pi$ is called π pulse and rotates the Bloch vector by 180° and therefore inverts the population of ground and excited state. Decoherence of the quantum state can be seen as a decay of the Bloch vector along the z-axis towards the ground state. More detailed information can be found in numerous textbooks and theses [23, 25, 28–30].

2.3.7 Ramsey experiment

So far the interaction of an atom with a continuous laser field was considered. In practice, the interaction time between the laser field and the atom is limited to a duration τ . For a set of different frequency detunings of the laser field from the atomic resonance, an excitation profile can be observed which corresponds to the Fourier transform of the excitation pulse [25]. This is known as Rabi spectroscopy. The spectral line width is limited by the interaction time τ .

Ramsey's method of separate oscillatory fields [5] is an alternative method to interrogate an atomic transition. Contrary to simple Rabi spectroscopy the interrogation consists of two laser pulses, separated by a waiting time τ_R . Starting in the electronic ground state $|0\rangle$, a resonant $\pi/2$ - pulse on the transition creates the superposition state $|\psi\rangle = \frac{1}{\sqrt{2}}(|\downarrow\rangle + |\uparrow\rangle)$. During the waiting time τ_R the state vector evolves freely $|\psi\rangle = \frac{1}{\sqrt{2}}(|\downarrow\rangle + ie^{-i\omega_0\tau_R} |\uparrow\rangle)$ at the optical frequency ($\omega_0/2\pi \approx 10^{15}$ Hz), that corresponds to the energy separation of both involved atomic states. It is useful to change into a co-rotating frame in order to see the influence of the second pulse. The state vector now becomes $|\psi'\rangle = \frac{1}{\sqrt{2}}(|\downarrow\rangle + ie^{-i(\omega_l - \omega_0)\tau_R} |\uparrow\rangle)$, which remains unchanged for a resonant laser field. Depending on its optical phase with respect to the first pulse, the second $\pi/2$ - pulse rotates the Bloch vector either up to the excited state $|1\rangle$ for $\Delta\varphi = 0^\circ$ or back to the ground state $|1\rangle$ for $\Delta\varphi = 180^\circ$. A detuning of the laser from the atomic resonance causes the Bloch vector to rotate around the z axis by $\phi = (\omega_l - \omega_0)\tau_R$, which gets mapped onto the observable σ_z by the second $\pi/2$ pulse. Precise knowledge of τ_R allows one to infer the detuning of the laser from the transition. This calculation is valid, if the duration of the $\pi/2$ - pulses is negligibly short compared to τ_R , otherwise an effective Ramsey time has to be considered. If the experiment is repeated for different laser detunings, a fringe pattern is observed (Ramsey pattern [5]). The spectral width of the fringes scales as $1/\tau_R$ in frequency. If the spectral resolution is limited by the finite interaction time between the laser and the ion, this method outperforms Rabi spectroscopy by roughly a factor of two in terms of frequency resolution [31].

If more than one ion is interrogated simultaneously, their transition frequencies can be slightly different due to external perturbations (see section 6.2). As already mentioned, dissipation and decoherence are always present in real quantum systems which are the limiting factors for the lifetime of the atom's quantum state (coherence time) [25]. Therefore the frequency resolution limit of the Ramsey experiment described above is set by the single ion coherence time which makes it hard to resolve transition frequency differences on the Hz scale or below. From Ramsey experiments with Ramsey times well beyond the single ion coherence time no useful information can be directly obtained from the excited state populations, but there are still correlations between the ions, which are known as quantum discord [32]. These correlations can be observed in the time evolution of the parity signal between two ions. The parity signal P is the product of the Pauli σ_z operators obtained by the excited state

populations p_j .

$$P = \sum_{j=0}^n (-1)^j p_j \quad (2.49)$$

The parity rescales the co- or anti-aligned z-components of the Bloch vectors to the interval $[-1, 1]$. Time-dependent oscillations in the parity signal represent a relative transition frequency difference between the ions. More information about this method can be found in section 6.2.

3 Level structure and radiative transitions in $^{40}\text{Ca}^+$ and $^{27}\text{Al}^+$ ions

This chapter describes the relevant energy levels of $^{40}\text{Ca}^+$ and $^{27}\text{Al}^+$ and the radiative transitions between them. The calcium ion has been used for a long time and its properties are described in detail in various theses [19, 29, 33–35]. However, for $^{27}\text{Al}^+$, there is no thesis containing a summary of its relevant properties. The available information is spread over various publications and theses. In terms of completeness a summary of the most important facts on $^{40}\text{Ca}^+$ is presented. Since this thesis is the first that reports on $^{27}\text{Al}^+$ in this group, a detailed description of the level structure and the relevant radiative transitions between them is presented. Furthermore a condensed version of a theoretical calculation of the decay rates of both relevant optical transitions according to [36] is given.

3.1 Level structure and radiative transitions of $^{40}\text{Ca}^+$

Singly charged Ca^+ has a single electron in the 4s shell. Therefore, its electronic structure is similar to hydrogen. A detailed level diagram of its lowest energy levels is presented in figure 3.1. The next orbital higher in energy than the ground state is the metastable 3d state that consists of two fine structure components, the $D_{3/2}$ and $D_{5/2}$ states with lifetimes of ~ 1.2 s and 1.149(4) s [37] respectively. They are linked to the ground state via an electric quadrupole transitions. The $S_{1/2} \leftrightarrow D_{5/2}$ transition is of interest as a frequency standard at a transition frequency of 411 042 129 776 393.2(1.0) Hz [38], which was measured by our group. There are three other absolute frequency measurements of this transition where one value agrees with the value above [39], while the other two are about 5 Hz [40] and 8 Hz [41] higher in frequency. The g-factors of ground and excited states are $g_{S_{1/2}} = 2.002\,256\,64(9)$ [42] and $g_{D_{5/2}} = 1.200\,3340(3)$ [38]. For the purpose of quantum computation and quantum simulation [28–30, 32, 33] a qubit / pseudo-spin can be encoded in the $S_{1/2}$ and $D_{5/2}$ Zeeman sub-states in a non-zero magnetic field. The frequency deviations from the line center of the ten possible transitions within the Zeeman manifolds can be calculated from the linear Zeeman effect

$$\Delta\nu_{S\leftrightarrow D} = \frac{\mu_B}{h} \left(g_{D_{5/2}} \cdot m_f - g_{S_{1/2}} \cdot m_i \right) \cdot B \quad (3.1)$$

where μ_B is the Bohr magneton, m_i and m_f are the magnetic quantum numbers of initial and final state and B is the amplitude of the magnetic field defining the quantization axis¹.

Again higher in energy is the short lived P orbital that consists of two fine structure components, the $P_{1/2}$ and $P_{3/2}$ state. Both levels are connected to the ground state and the D states via strong dipole transitions.

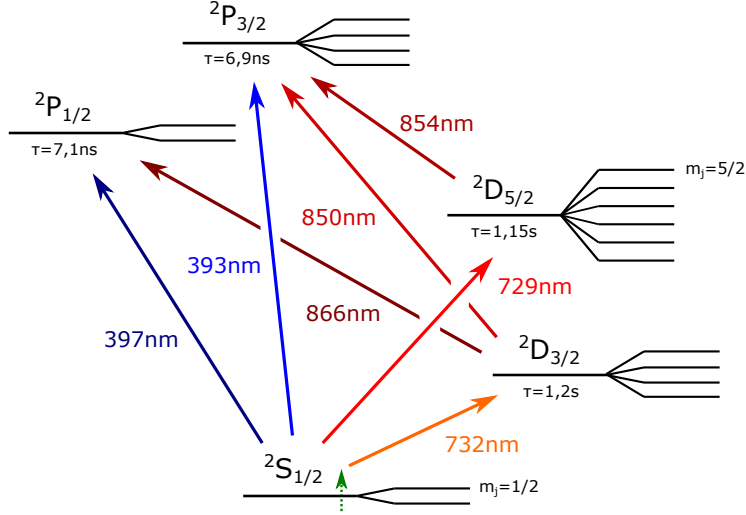


Figure 3.1: Detailed level diagram showing all relevant orbitals including the Zeeman sub-levels of $^{40}\text{Ca}^+$. Laser light at 397 nm is used for Doppler-cooling, state detection and optical pumping. The S-D electric quadrupole transition is driven by an ultra-stable laser at 729 nm. Since the P levels can decay to the D states, repumping lasers at 854 nm and 866 nm are required.

The $S_{1/2} \leftrightarrow P_{1/2}$ transition is used for Doppler-cooling and state detection. Because of a probability of 6.435(7) % [43] to decay to the $D_{3/2}$ state, a laser at 866 nm is used for repumping. For the purpose of repumping from the $D_{5/2}$ states after each experiment as well as for quenching while sideband-cooling [44, 45] a laser at 854 nm is used. A detailed overview of natural abundances of calcium isotopes, branching ratios of the transitions in figure 3.1 and transition wavelengths can be found in [29] and references therein.

3.1.1 Dipole transitions

The Rabi frequency Ω of an electric dipole transition is related to the dipole matrix element

$$\Omega = \frac{1}{\hbar} \langle S | \vec{d} \cdot \vec{E} | P \rangle \quad (3.2)$$

¹ $\mu_B/h \approx 1.3996385 \text{ MHz/G}$

with the maximum electric field amplitude \vec{E} at the position of the ion and the electric dipole moment $\vec{d} = e \cdot \vec{r}$. The decay rate of the excited state is given by

$$\Gamma = \frac{\omega^3 |\langle S | \vec{d} \cdot \vec{E}_{vac} | P \rangle|^2}{3\pi\epsilon_0 \hbar c^3} \quad (3.3)$$

where \vec{E}_{vac} is the vacuum electric field amplitude at the position of the ion, ϵ_0 is the vacuum permittivity and c the speed of light.

3.1.2 Quadrupole transitions

Electric quadrupole transitions like the $S_{1/2} \leftrightarrow D_{5/2}$ transition in $^{40}\text{Ca}^+$ are orders of magnitude weaker than the dipole transitions mentioned above. The excited state lifetime of 1.149 s and the corresponding natural linewidth of $2\pi \cdot 139$ mHz allows for encoding a qubit or a pseudo spin for the purpose of quantum computation and quantum simulation [28–30, 32, 33]. In addition, it can be used as an optical frequency standard [38–40]. The Hamiltonian $H = \nabla \mathbf{E}^{(2)}(t) \Theta^{(2)}$ [46] describing the transition consists of the tensor for the gradient of the electric part of the laser radiation $\nabla \mathbf{E}(t)$ and the induced quadrupole moment tensor $\Theta^{(2)}$. The resulting Rabi-frequency of this transition is given by [19, 20]

$$\Omega = \left| \frac{eE_0}{2\hbar} \langle S, m_S | (\boldsymbol{\epsilon} \cdot \mathbf{r}) (\mathbf{k} \cdot \mathbf{r}) | D, m_D \rangle \right| \quad (3.4)$$

where \mathbf{r} is the electrons position operator with respect to the center of mass, \mathbf{k} indicates the light propagation direction and $\boldsymbol{\epsilon}$ is the polarization vector of the light field. The decay rate of the excited state is given by

$$\Gamma = \frac{c\alpha k^5}{90} \left| \langle S_{1/2} | r^2 C^{(2)} | D_{5/2} \rangle \right|^2 \quad (3.5)$$

with $\langle S_{1/2} | r^2 C^{(2)} | D_{5/2} \rangle$ being the reduced matrix element [20]. For different transitions within the Zeeman manifold the matrix element $\langle S, m_S | (\boldsymbol{\epsilon} \cdot \mathbf{r}) (\mathbf{k} \cdot \mathbf{r}) | D, m_D \rangle$ in (3.4) can be replaced by the reduced matrix element and the Clebsch-Gordan coefficients $\Lambda_{J,J'}(m, m')$. To account for a specific geometry the equation describing the Rabi frequency needs to be multiplied by a factor $g^{(\Delta m)}(\varphi, \vartheta)$ [19, 20, 35] with ϑ being the angle between the polarization and the projection of the magnetic field onto the incident plane, while φ is the angle between the magnetic field and \mathbf{k} . Thus the Rabi frequency can be rewritten as

$$\Omega = \frac{\epsilon}{2\hbar} \sqrt{\frac{15}{c\alpha}} E_0 \sqrt{\frac{\Gamma}{k^3}} \Lambda_{J,J'}(m, m') g^{(\Delta m)}(\varphi, \vartheta) \quad (3.6)$$

with the fine structure constant α . A detailed treatment of the geometrical factor can be found in [19]. The selection rules $\Delta m = 0, \pm 1, \pm 2$ for electric quadrupole transitions allow for

five different transitions starting in a particular Zeeman level of the $S_{1/2}$ ground state. The corresponding Clebsch-Gordan coefficients are listed in table 3.1.

m'	$-\frac{3}{2}$	$-\frac{1}{2}$	$\frac{1}{2}$	$\frac{3}{2}$	$\frac{5}{2}$
$\Lambda(1/2, m')$	$\sqrt{\frac{1}{5}}$	$\sqrt{\frac{2}{5}}$	$\sqrt{\frac{3}{5}}$	$\sqrt{\frac{4}{5}}$	1

Table 3.1: Clebsch-Gordan coefficients $\Lambda(m, m')$ for $S_{1/2}, m_j = 1/2 \leftrightarrow D_{5/2}, m'$ transitions. In the case of starting in $S_{1/2}, m_j = -1/2$ the sign of the target states m' is inverted.

3.2 Level structure and radiative transitions of $^{27}\text{Al}^+$

^{27}Al is the only stable aluminium isotope. With two valence electrons in the 3s shell, the electronic structure of $^{27}\text{Al}^+$ is similar to Helium. It has a nuclear spin of $I = 5/2$ and therefore shows hyperfine structure. A detailed overview of the level structure is presented in figure 3.2. The magnetic dipole moment of the nucleus is $3.6415069(7) \mu_N$ [47] ($\mu_N = \frac{e\hbar}{2m_p}$) and its electric quadrupole moment is $0.1466(10) \cdot 10^{-28} \text{em}^2$ [47]. The next orbital above the ground state is the 3p level, which consists of three fine-structure components. The lowest one is the $^3\text{P}_0$ state with a natural lifetime of $20.6(1.4) \text{s}$ [48] which results in a natural linewidth of $2\pi \cdot 7.6 \text{mHz}$. It is linked to the ground state via a hyperfine-induced [36] transition at 267.4 nm. This transition is doubly forbidden with respect to dipole transition selection rules since the spin state changes and the angular momentum state does not. Because of its low sensitivity to magnetic field fluctuations, electric field gradients [49, 50] and black body radiation [51], it is well suited for an optical frequency standard. The exact transition frequency was measured to be $1\,121\,015\,393\,207\,857.4(7) \text{Hz}$ [52] and the g-factors are $g_{1\text{S}_0} = -0.00079248(14)$ and $g_{3\text{P}_0} = -0.00197686(21)$ [48].

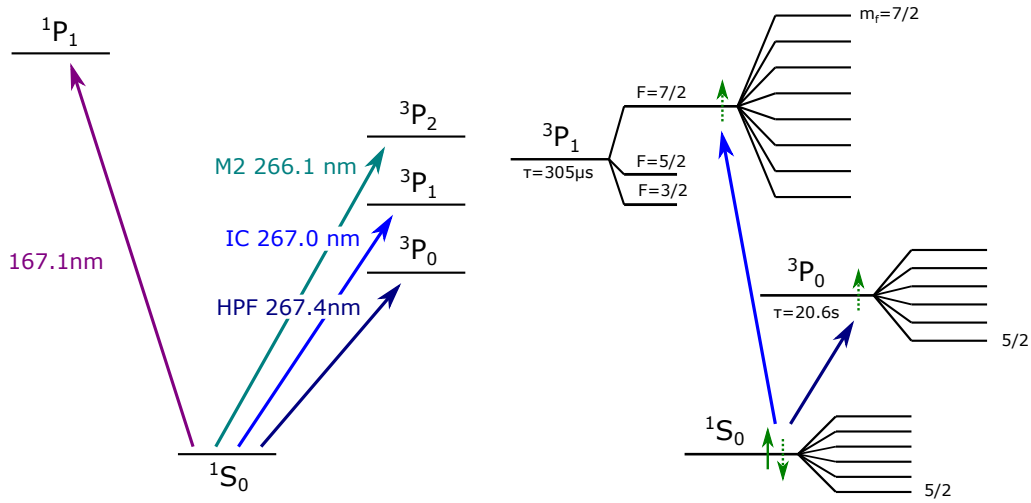


Figure 3.2: *Left: Overview of the energy levels of $^{27}\text{Al}^+$ and transitions indicated by colored arrows. See main text for further information. Right: Detailed level diagram of the relevant orbitals and their Zeeman sub-levels. An ultra-stable laser at 267.0 nm is used to drive the intercombination transition for optical pumping to the stretched Zeeman states and for quantum logic state mapping. Another ultra-stable laser at 267.4 nm is used to drive the hyperfine-induced clock transition.*

This results in a relatively small sensitivity with respect to the magnetic field of only a few kHz/G. The line center shifts because of the quadratic Zeeman shift by $-0.71988(48) \text{Hz/G}^2$ [48]. A detailed discussion of systematic frequency shifts of a single aluminium ion

clock can be found in [14, 48]. The $^3\text{P}_1$ level can be reached from the ground state via a spin forbidden intercombination [36] transition at 267.0 nm. The upper state lifetime is 305 μs [53] and the corresponding natural linewidth is $2\pi \cdot 520$ Hz. It can be used for optical pumping and state mapping but is not strong enough for efficient Doppler-cooling. Again higher in energy is the $^3\text{P}_2$ state that can be reached from the ground state via a magnetic quadrupole transition at 266.1 nm [54]. The natural lifetime of the $^3\text{P}_2$ state is about 5 min [54]. The strong $^1\text{S}_0 \leftrightarrow ^1\text{P}_1$ dipole transition at 167.1 nm [54] lies in the vacuum ultraviolet (VUV) range. Even though current laser technology makes excitation of this transition possible, its spectral width of $2\pi \cdot 224$ MHz [54] prevents efficient Doppler-cooling to the Lamb-Dicke regime. Nevertheless it could be used for fluorescence detection, but has the disadvantage that the light source and the detection unit need to be in vacuum because of the low transmissivity of air at this wavelength. In contrast to the case of $^{40}\text{Ca}^+$ there is no strong transition that can be used for repumping from the long lived states.

Since both transitions used in this work behave like dipole transitions, the corresponding Rabi frequencies can be estimated by using the expression for dipole transitions with a lower decay rate. Calculations of the level energies and decay rates for the $^3\text{P}_0$ and $^3\text{P}_1$ states are quite sophisticated. Nevertheless a short guideline of the mathematical treatment according to [36] is given. Since this is only a brief summary, showing the main results of an extensive theory the reader is referred to [55–58] where a detailed treatment of the problem is presented.

The mathematical approach is the same for both transitions. The P states are not considered to be pure electronic states anymore but are constructed as mixed electronic states with mixing coefficients c_i , i.e.

$$|{}^{\gamma}JIF\rangle = \sum_i c_i |\gamma_i J_i I F\rangle \quad (3.7)$$

with quantum numbers for the nuclear spin I and the total angular momentum $F = J + I$. The notation ${}^{\gamma}JIF$ represents the dominant part of the eigen-vectors that construct the state. γ represents the mean quantum numbers to fully specify the state. Thus the state ${}^{\gamma}JIF$ contains admixtures from other states $\gamma_i J_i I F$ and their properties like a finite transition probability to the ground state. The coupling mechanisms that introduce the mixing of the wave-functions can have different origins like relativistic interaction or hyperfine interaction. The cases of the intercombination line $^1\text{S}_0 \leftrightarrow ^3\text{P}_1$ and the hyperfine induced transition $^1\text{S}_0 \leftrightarrow ^3\text{P}_0$ will be considered in the following.

3.2.1 The $^1\text{S}_0 \leftrightarrow ^3\text{P}_1$ intercombination line

The intercombination transition in $^{27}\text{Al}^+$ is spin-forbidden with respect to dipole transition selection rules ($\Delta S = 0$). It's finite probability to decay to the ground state via a single photon

process is induced by relativistic interaction between $^1\text{P}_1$ and $^3\text{P}_1$ states which is described by the Breit-Pauli Hamiltonian [36, 55, 58]. Since the Breit-Pauli Hamiltonian is extremely complex, the reader is referred to the corresponding references for more detailed information.

A first order expression of the transition moment $S^{1/2}(3s3p^3\text{P}_1 \rightarrow ns^2^1\text{S}_0)$, which is defined as the square root of the line strength S , is expressed by the dipole matrix element $\langle 3s3p^3\text{P}_1 | \mathbf{D}^{(1)} | 3s^2^1\text{S}_0 \rangle$ [36]

$$S^{1/2}(3s3p^3\text{P}_1 \rightarrow ns^2^1\text{S}_0) = \langle 3s3p^3\text{P}_1 | \mathbf{D}^{(1)} | 3s^2^1\text{S}_0 \rangle$$

$$\propto \frac{\Delta E_{FS}}{\Delta E_{term}} \langle 3s3p^1\text{P}_1 | \mathbf{D}^{(1)} | 3s^2^1\text{S}_0 \rangle \quad (3.8)$$

where $\mathbf{D}^{(1)} = \mathbf{d} \cdot \mathbf{E}$ is the electric dipole operator [55, 58], ΔE_{FS} is the fine-structure splitting between $^3\text{P}_1$ and $^3\text{P}_0$ levels and ΔE_{term} is the energy separation of the $^1\text{P} - ^3\text{P}$ terms. The decay rate can be calculated from the transition moment [36] to

$$\Gamma(3s3p^3\text{P}_1 \rightarrow ns^2^1\text{S}_0) = \frac{e^2 a_0^2 \omega^3}{9\pi \epsilon_0 \hbar c^3} \left| S^{1/2}(3s3p^3\text{P}_1 \rightarrow 3s^2^1\text{S}_0) \right|^2. \quad (3.9)$$

The intercombination transition is induced by the strong $^1\text{S}_0 \leftrightarrow ^1\text{P}_1$ dipole transition. Consequently, possible transitions between the Zeeman manifolds of ground and excited state are subject to selection rules for electric dipole transitions ($\Delta m_f = 0, \pm 1$). The transition manifold is depicted in figure 3.3.

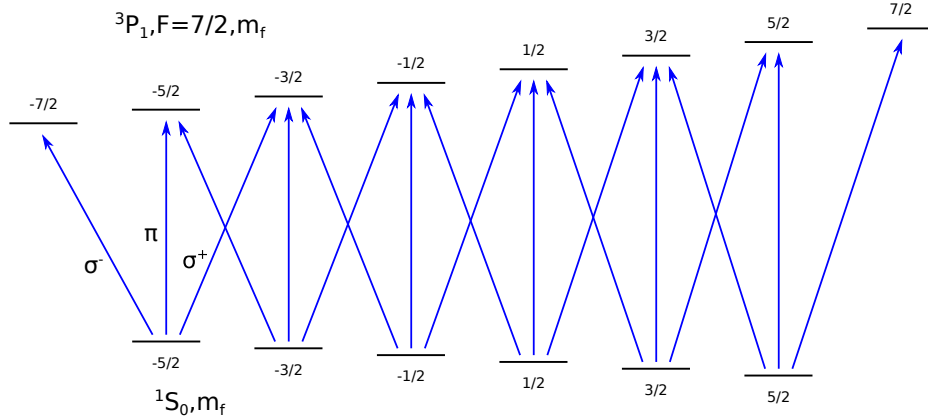


Figure 3.3: A finite magnetic field lifts the degeneracy of the $^1\text{S}_0$ and $^3\text{P}_1, F = 7/2$ Zeeman states. Consequently six π ($\Delta m_f = 0$) and twelve σ ($\Delta m_f = \pm 1$) transitions are possible.

Clebsch-Gordan coefficients for specific transitions within the Zeeman manifolds are listed in tables 3.2 and 3.3.

$^1\text{S}_0 m_f \leftrightarrow ^3\text{P}_1 m_f$	$-\frac{5}{2} \leftrightarrow -\frac{3}{2}$	$-\frac{3}{2} \leftrightarrow -\frac{1}{2}$	$-\frac{1}{2} \leftrightarrow \frac{1}{2}$	$\frac{1}{2} \leftrightarrow \frac{3}{2}$	$\frac{3}{2} \leftrightarrow \frac{5}{2}$	$\frac{5}{2} \leftrightarrow \frac{7}{2}$
Λ	$\sqrt{\frac{1}{21}}$	$\sqrt{\frac{1}{7}}$	$\sqrt{\frac{2}{7}}$	$\sqrt{\frac{10}{21}}$	$\sqrt{\frac{5}{7}}$	1

Table 3.2: Clebsch-Gordan coefficients for $\Delta m = +1$ transitions. For the case of $\Delta m = -1$ the sign of initial and final m_f states have to be flipped.

$^1\text{S}_0 m_f \leftrightarrow ^3\text{P}_1 m_f$	$-\frac{5}{2} \leftrightarrow -\frac{5}{2}$	$-\frac{3}{2} \leftrightarrow -\frac{3}{2}$	$-\frac{1}{2} \leftrightarrow -\frac{1}{2}$	$\frac{1}{2} \leftrightarrow \frac{1}{2}$	$\frac{3}{2} \leftrightarrow \frac{3}{2}$	$\frac{5}{2} \leftrightarrow \frac{5}{2}$
Λ	$\sqrt{\frac{2}{7}}$	$\sqrt{\frac{10}{21}}$	$\sqrt{\frac{4}{7}}$	$\sqrt{\frac{4}{7}}$	$\sqrt{\frac{10}{21}}$	$\sqrt{\frac{2}{7}}$

Table 3.3: Clebsch-Gordan coefficients for $\Delta m = 0$ transitions.

3.2.2 The hyperfine induced $^1\text{S}_0 \leftrightarrow ^3\text{P}_0$ clock transition

Single photon transitions between pure electronic states $J = 0 \leftrightarrow J' = 0$ are strictly forbidden by any electric/magnetic multipole order [14]. In ions or atoms with nonzero nuclear spin hyperfine (HFS) interaction introduces a mixing between wave-functions with different J quantum numbers with mixing coefficients c_i . The corresponding hyperfine Hamiltonian is given by $\mathbf{H}_{hfs} = -ec\boldsymbol{\alpha} \cdot \mathbf{A}(\mathbf{r}) + e\phi(\mathbf{r})$, with the Dirac matrix $\boldsymbol{\alpha}$, the magnetic vector potential $\mathbf{A}(\mathbf{r}) = \frac{\mu_0}{4\pi} \frac{(\boldsymbol{\mu} \times \mathbf{r})}{r^3}$ and the nuclear quadrupole moment tensor $\phi(\mathbf{r}) = \frac{1}{4\pi\epsilon_0} \sum_{ij} \frac{x_i x_j}{2r^5} \int d^3r (3x_i x_j - r^2 \delta_{ij}) \rho(\mathbf{r})$. Since the hyperfine hamiltonian is quite complex, it is useful to express it in a multipole expansion $\mathbf{H}_{hfs} = \mathbf{H}_{hfs}^{M1} + \mathbf{H}_{hfs}^{E2} + \dots$ [36].

As the clock transition is induced by interactions with $J = 1$ levels [36], only the first part of the expansion is of interest. It represents the interaction between the nuclear magnetic dipole moment and the electronic field at the nucleus. Consequently, the excited mixed state can be written as [36]

$$|{}^3s3p\ ^3\text{P}_0\rangle = |3s3p\ ^3\text{P}_0\rangle + \sum_i c_i |\gamma_i J_i = 1\rangle. \quad (3.10)$$

Thus the state $|{}^3s3p\ ^3\text{P}_0\rangle$ contains admixtures from other states $\gamma_i J_i = 1$ and their properties like a finite transition probability to the ground state. In view of the weakness of the hyperfine interaction compared to the relativistic interaction inducing the intercombination transition, the radiative decay rates are expected to be significantly lower ($\mathcal{O}(c_i^2) \approx 10^6$) than the one from the associated intercombination line (see above). The size of the mixing coefficients is given by [36]

$$c_i \approx \frac{\langle \gamma_i J_i = 1 | \mathbf{H}_{hfs}^{M1} | 3s3p\ ^3\text{P}_0 \rangle}{E(3s3p\ ^3\text{P}_0) - E(\gamma_i J_i = 1)} \quad (3.11)$$

where \mathbf{H}_{hfs}^{M1} is the magnetic dipole part of the hyperfine operator [55, 58]. Decoupling the

nuclear and electronic part of $\mathbf{H}_{hfs}^{M1} = \mathbf{T}^{(1)} \cdot \mathbf{M}^{(1)}$ by using the spherical electronic and nuclear tensor operators $\mathbf{T}^{(1)}$ and $\mathbf{M}^{(1)}$ [55, 58], respectively followed by a lengthy mathematical transformation yields [36]

$$c_i \approx \frac{\mu_I(1 + I^{-1})^{1/2}}{\sqrt{3}} \frac{\langle \gamma_i J_i = 1 | |\mathbf{T}^{(1)}| | 3s3p^3P_0 \rangle}{E(3s3p^3P_0) - E(\gamma_i J_i = 1)} \quad (3.12)$$

where μ_I is the nuclear magnetic moment and I the nuclear spin. This is the final result for the mixing coefficient to first order in the presence of hyperfine interaction. For the calculation of the transition rate only the electric dipole contribution needs to be considered [36] since the decay rate of the $^1S_0 \leftrightarrow ^3P_2$ magnetic quadrupole transition is at least 4-5 orders of magnitude lower than the decay rate of the intercombination line. The decay rate of the 3P_0 state is given by

$$\Gamma(3s3p^3P_0 \rightarrow 3s^2^1S_0) = \frac{e^2 a_0^2 \omega^3}{9\pi \epsilon_0 \hbar c^3} \left(\sum_i c_i \langle \gamma_i J_i = 1 | |\mathbf{D}^{(1)}| | 3s^2^1S_0 \rangle \right)^2 \quad (3.13)$$

with the electric dipole operator $\mathbf{D}^{(1)}$. Inserting the mixing coefficients leads to the final expression for the decay rate of the 3P_0 level [36].

$$\Gamma(3s3p^3P_0 \rightarrow 3s^2^1S_0) \approx \mu_I^2 (1 + I^{-1}) \frac{e^2 a_0^2 \omega^3}{27\pi \epsilon_0 \hbar c^3} \left| \sum_i \frac{\langle \gamma_i J_i = 1 | |\mathbf{T}^{(1)}| | 3s3p^3P_0 \rangle}{E(3s3p^3P_0) - E(\gamma_i J_i = 1)} \langle \gamma_i J_i = 1 | |\mathbf{D}^{(1)}| | 3s^2^1S_0 \rangle \right|^2. \quad (3.14)$$

The transition is induced by the $^1S_0 \leftrightarrow ^3P_1$ intercombination transition which is represented as the reduced matrix element of the electric dipole operator $\mathbf{D}^{(1)}$. This is weighted by the ratio of the reduced matrix element of the hyperfine $\mathbf{T}^{(1)}$ operator and the energy separation of the atomic levels involved. The complete nuclear contribution to the decay rate is governed by the term $\mu_I^2(1 + I^{-1})$.

Possible transitions according to the selection rules for dipole transitions between the Zeeman manifolds of ground and excited state are depicted in figure 3.4. Clebsch-Gordan coefficients for the transition manifold are listed in tables 3.4 and 3.5.

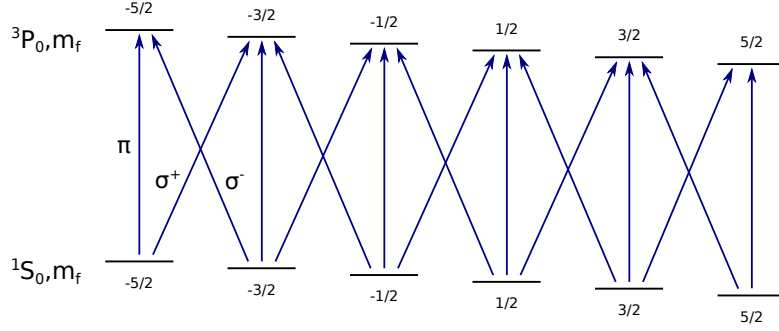


Figure 3.4: The degeneracy of the $^1\text{S}_0$ and $^3\text{P}_0$ Zeeman states is lifted by a finite magnetic field. Consequently six π - and ten σ - transitions can be driven.

$^1\text{S}_0 m_f \leftrightarrow ^3\text{P}_0 m_f$	$-\frac{5}{2} \leftrightarrow -\frac{5}{2}$	$-\frac{3}{2} \leftrightarrow -\frac{3}{2}$	$-\frac{1}{2} \leftrightarrow -\frac{1}{2}$	$\frac{1}{2} \leftrightarrow \frac{1}{2}$	$\frac{3}{2} \leftrightarrow \frac{3}{2}$	$\frac{5}{2} \leftrightarrow \frac{5}{2}$
Λ	$-\sqrt{\frac{5}{7}}$	$-\sqrt{\frac{9}{35}}$	$-\sqrt{\frac{1}{35}}$	$\sqrt{\frac{1}{35}}$	$\sqrt{\frac{9}{35}}$	$\sqrt{\frac{5}{7}}$

Table 3.4: Clebsch-Gordan coefficients for $\Delta m = 0$ transitions.

$^1\text{S}_0 m_f \leftrightarrow ^3\text{P}_0 m_f$	$-\frac{5}{2} \leftrightarrow -\frac{3}{2}$	$-\frac{3}{2} \leftrightarrow -\frac{1}{2}$	$-\frac{1}{2} \leftrightarrow \frac{1}{2}$	$\frac{1}{2} \leftrightarrow \frac{3}{2}$	$\frac{3}{2} \leftrightarrow \frac{5}{2}$
Λ	$-\sqrt{\frac{6}{21}}$	$-\sqrt{\frac{16}{35}}$	$-\sqrt{\frac{18}{35}}$	$-\sqrt{\frac{16}{35}}$	$-\sqrt{\frac{6}{21}}$

Table 3.5: Clebsch-Gordan coefficients for $\Delta m = +1$ transitions. For the case of $\Delta m = -1$ flip the sign of initial and final m_f states.

3.2.3 Nuclear spin flips

Transitions between the hyperfine ground state levels can be induced by an AC magnetic field perpendicular to the quantization axis, that couples to the magnetic dipole moment of the nucleus. The coupling strength is given by:

$$\Omega = \left| \frac{1}{2\hbar} \langle ^1\text{S}_0, m_F | \vec{\mu}_I \cdot \vec{B} | ^1\text{S}_0, m_{F'} \rangle \right| \quad (3.15)$$

where $\vec{\mu}_I$ is the nuclear magnetic moment and \vec{B} the AC magnetic field. The transition wavelength is on the order of 100 km for laboratory conditions and the resulting Lamb-Dicke parameter is on the order of 10^{-12} . Consequently only carrier transitions can be driven. Nuclear transitions within the Zeeman manifold of the electronic ground state are depicted in figure 3.5. The Clebsch-Gordan coefficients for transitions between the six ground state levels of $^{27}\text{Al}^+$ are listed in table 3.6.

These nuclear spin flips can be used to characterize the efficiency of optically pumping (see section 5.2) the aluminium ion to the outermost Zeeman states (stretched states). At a

finite magnetic field the degeneracy of the six ground state levels is lifted. This results in six equidistantly spaced energy levels with Zeeman splittings of ~ 1.1 kHz/G. The same approach can be used to drive transitions between the two ground state levels of $^{40}\text{Ca}^+$. In this case, the magnetic field couples to the spin of the valence electron [35].

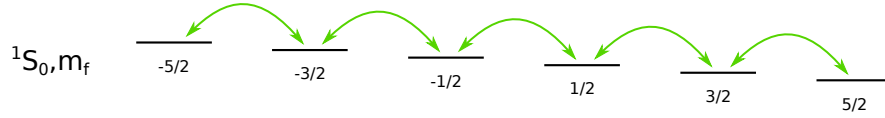


Figure 3.5: Zeeman structure of the 1S_0 ground state of $^{27}\text{Al}^+$ in a finite magnetic field. Six equidistantly spaced Zeeman levels emerge due to a nuclear spin of $I = 5/2$ which can be coupled by an AC magnetic field.

$^1S_0 m_f \leftrightarrow ^1S_0 m_f$	$-\frac{5}{2} \leftrightarrow -\frac{3}{2}$	$-\frac{3}{2} \leftrightarrow -\frac{1}{2}$	$-\frac{1}{2} \leftrightarrow \frac{1}{2}$	$\frac{1}{2} \leftrightarrow \frac{3}{2}$	$\frac{3}{2} \leftrightarrow \frac{5}{2}$
Λ	$\sqrt{\frac{2}{7}}$	$\sqrt{\frac{16}{35}}$	$\sqrt{\frac{18}{35}}$	$\sqrt{\frac{16}{35}}$	$\sqrt{\frac{2}{7}}$

Table 3.6: Clebsch-Gordan coefficients for $\Delta m = \pm 1$ transitions.

4 Experimental setup

The main part of the experiments presented in this work was carried out in a newly set up laboratory (lab 2) located at the Institute of Quantum Optics and Quantum information (IQOQI) in Innsbruck. It hosts a new vacuum chamber including the ion trap, designed for the purposes of a semi-portable optical frequency standard and all required laser systems. The ion trap and most of the lasers were set up on a non-magnetic optical table and on breadboards mounted below the table. The high-finesse resonators for all three stable light sources are located in the basement of the building and are linked to the lasers via optical fibers.

4.1 Ion trap setup

For the new setup a modified version of the standard Innsbruck blade-shaped linear Paul trap [29, 33] was designed. A sectional view of the vacuum chamber, which contains the ion trap, and the optical beam paths is presented in figure 4.1.

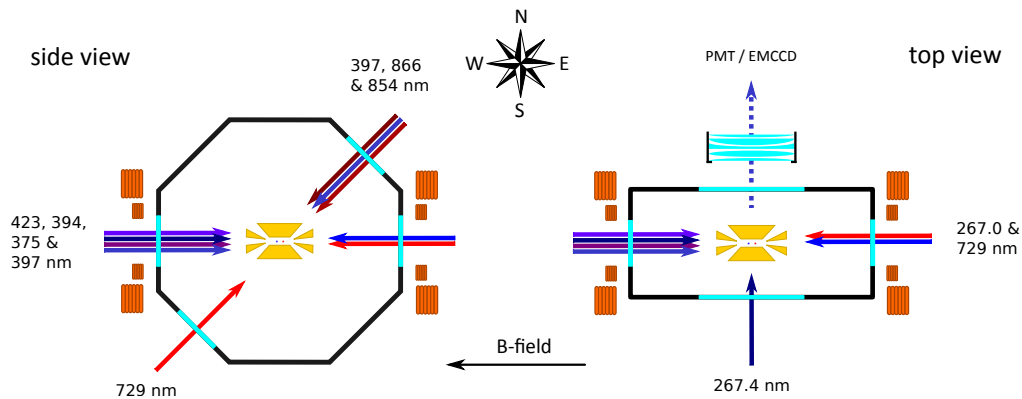


Figure 4.1: Sectional view of the octagon showing optical access and the imaging path. The coils that provide the quantization magnetic field along the trap axis are indicated in orange. Laser beams are presented as colored arrows. The compass indicates the orientation of the chamber in the laboratory.

A technical drawing, which shows the trap electrodes, the isolating parts and the compensation electrodes is presented in figure 4.2. In figure 4.7 a more detailed drawing of the chamber is presented, which also shows the parts attached to the vacuum chamber like the helical resonator, magnetic field coils, the vacuum pumps and so on. The vacuum chamber is mounted

to an optical breadboard which rests on electrically isolated posts, that are mounted to the optical table.

To optimize the new trap setup for the operation as a frequency standard, the main focus was to keep the influence of external perturbations and the corresponding systematic frequency shifts as small as possible. A crucial point is the stability of the magnetic field, which is improved by a magnetic shielding enclosure. In view of the AC-Stark shift caused by black-body-radiation, the trap temperature should be kept low, which required a different choice of materials compared to other traps in our group. With regard to portability, the compactness of the vacuum chamber played a role. During this work two nearly identical ion trap setups were built.

4.1.1 Linear Paul trap

The new linear Paul trap consists of four blade-shaped electrodes that are symmetrically aligned within the radial plane. Pairs of opposite blades are kept on the same potential, with one pair connected to RF and the other pair grounded or kept on a low DC voltage (1.5 V battery) to break the symmetry of the resulting trap potential. This creates the pseudopotential in the radial direction. To confine the ions along the axis, two endcap electrodes are held at a positive voltage. To allow for the compensation of stray fields two stainless steel pairs of electrodes parallel to the trap axis are attached. The radial electrode to ion distance is about 555 μm , the endcap separation is 4.5 mm. The radius of curvature at the end of the blades is 135 μm . Holes in the endcaps with a diameter of 0.5 mm provide optical access along the trap axis.

Former traps which were made of stainless steel and Macor reached temperatures up to 150 $^{\circ}\text{C}$ during their operation [34]. This is a drawback for optical frequency standards because of the increased AC Stark shift caused by black-body radiation at elevated temperatures. To reduce the heating of the new trap significantly, different materials were chosen. In the new setup sapphire is used as the electrically isolating part (see figure 4.2). Its heat conductivity of about 24 W/mK is a factor of ~ 17 higher¹ and its RF loss tangent of about $5 \cdot 10^{-5}$ an order of magnitude smaller² compared to Macor. In order to directly measure the trap temperature a resistor³ was attached to the sapphire. Figure 4.3 displays the dependence of the trap temperature on the RF power that is sent into the helical resonator. To match the thermal expansion coefficient of sapphire, gold-plated titanium electrodes were used. Since titanium has a native oxide on its surface, which reduces electrical conductivity especially in the radio frequency domain, the titanium was coated with a 10 μm thick layer of gold by

¹Comparison of mean values found on websites of different manufacturers in the World Wide Web

²Comparison of mean values found on websites of different manufacturers in the World Wide Web

³Allectra PT 100-C2

electroplating⁴. Consequently less electrical power gets dissipated in the trap electrodes, which reduces the trap temperature and makes it insensitive against RF power changes. Furthermore, low power consumption⁵ is for instance important for satellite applications.

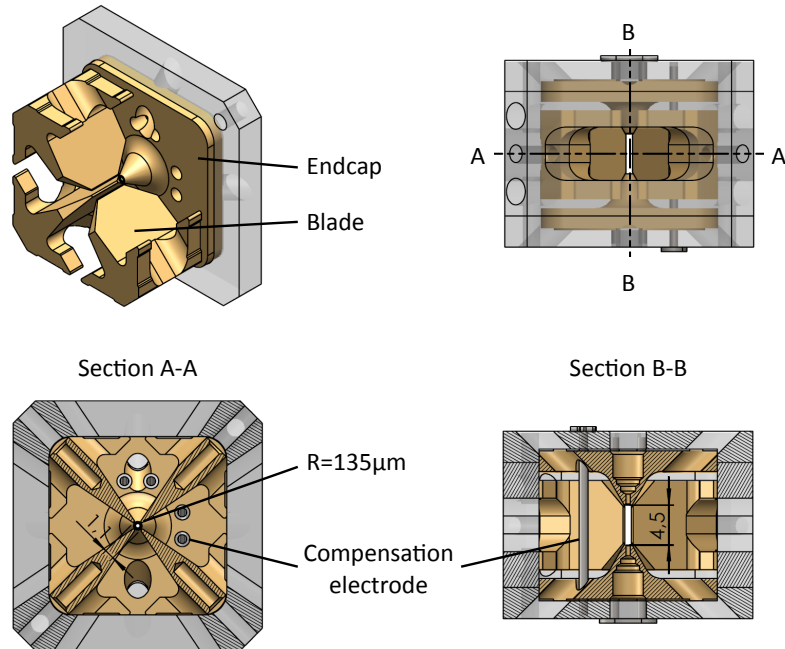


Figure 4.2: Drawing of the linear Paul trap. Intersections are shaded. The golden electrodes in the center create the trapping field. The electrodes are held by three surrounding sapphire parts (light grey). The four steel rods off axis are the compensation electrodes. The trap is held in place by a titanium support with a solid state spring which is not shown. Screws and electrical connections are also not shown.

A second advantage is the higher work function of (polycrystalline) gold of 5.1 eV [59] compared to stainless steel (4.4 eV [59]). These values correspond to photon energies of radiation at 243 nm and 282 nm respectively. This will reduce the creation of photo-electrons during illumination with 267 nm light as long as no other contaminants are on the electrode surfaces. The size and shape of the electrodes (see figure 4.2) is almost identical with the trap described in [29]. Electrostatic finite element simulations⁶ of the trapping potential were carried out. The static potential of the new trap along the trap axis for a voltage of 1 V applied to both endcap electrodes is presented in figure 4.4. The contribution of the the quartic term to the potential at the trap center ($\pm 100 \mu\text{m}$) is well below 1 %. The calculated trapping frequency for a single $^{40}\text{Ca}^+$ ion for an endcap voltage of $U_0 = 400 \text{ V}$ is 727 kHz. The

⁴Electroplated by Michael Niedermayer and Kirill Lakhmanskiy at the University of Innsbruck

⁵Compared to the setup described in [29] only a quarter of the electrical power is needed to achieve the same confinement.

⁶Comsol Multiphysics 4

experimentally observed value is 819 kHz. The mismatch is most likely due to an asymmetry of the trap with respect to the radial plane. All four blades were shifted by a few ten μm towards one endcap during the assembling.

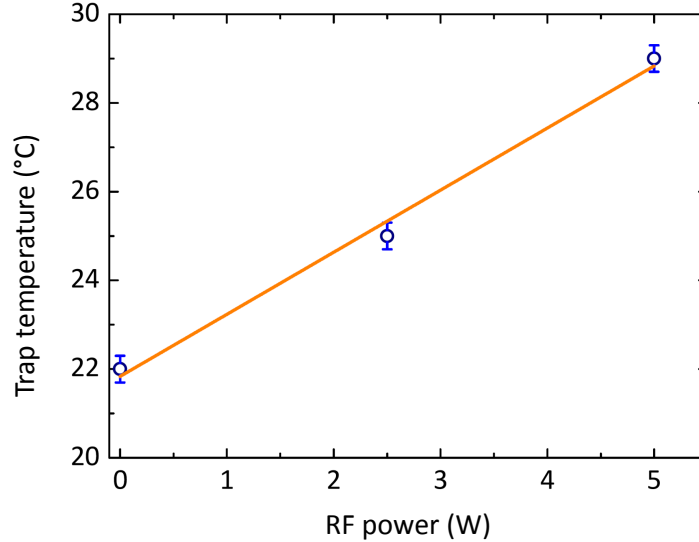


Figure 4.3: *Equilibrium trap temperature depending on the RF power sent into the helical resonator. The resistance was measured with the 4-point method. Since the trap RF disturbed the measurement, the displayed values represent the temperature directly after switching off the RF. Since the trap already started to cool down, conservative error bars are given. The temperature increases linearly by 1.4 K/W. The room temperature in the lab is 22 °C. During experiments with the mixed ion crystal, the trap is operated at 1 W which increases its equilibrium temperature by 1.4 degrees.*

The pseudopotential in the radial plane, which is displayed in figure 4.5, is derived from the simulated static potentials in a second step. The radial oscillation frequency for a single calcium ion at a RF voltage of $V_0 = 1000$ V is 3.2 MHz. Since there is no direct way to measure the voltage on the radial blades in this setup, there are no experimental values to compare to. For more information the reader is referred to [29]. There, a voltage divider on the helical resonator was used to estimate the blade voltage and consequently a comparison between theoretical and experimental results was possible. A setup for a stabilization of the RF voltage on the blade electrodes can be found in [32].

To avoid thermal stress during the bake-out, the trap holder with a solid-state spring (see figure 4.7) at one side was also made of titanium. Two targets, one of pure aluminium and one of an alloy⁷ (30% Ca, 70% Al) were attached 26 mm above the trap for laser ablation.

⁷Konik industries

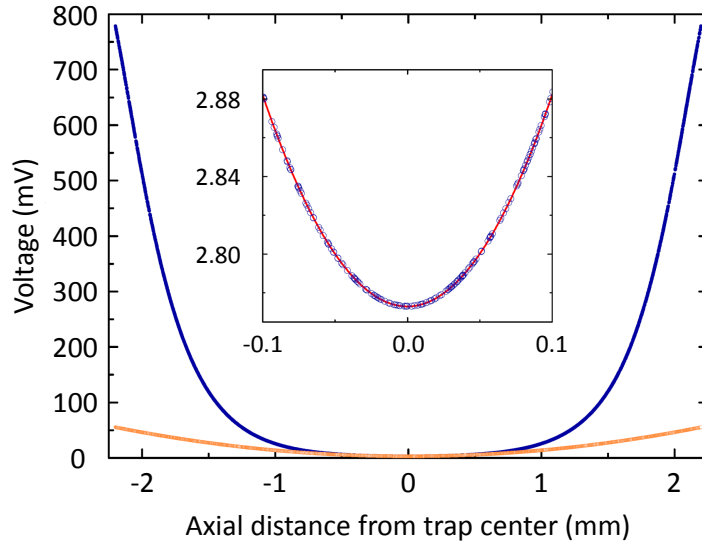


Figure 4.4: *Finite element simulation of the axial trapping confinement for a voltage of +1 V on both endcaps. The resulting potential is displayed by the blue curve in the main plot. The inset plot shows the potential at the trap center ($\pm 100 \mu\text{m}$) and a fourth degree polynomial fit (red line). The orange line in the main plot represents the harmonic part of the potential. The anharmonicities at the trap center are well below 1 %.*

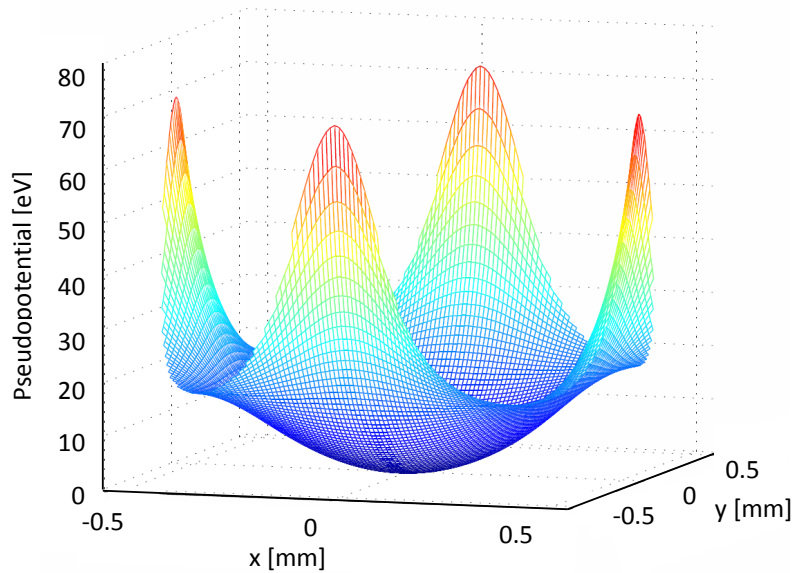


Figure 4.5: *Pseudopotential for a $^{40}\text{Ca}^+$ ion at a trap drive frequency of 32 MHz and $V_0 = 1000$ V inferred from electrostatic FEM simulations. The blade electrodes are aligned along the x and y axis.*

An important property of ion traps is the heating rate. It determines the rate at which a cold trapped ion gains kinetic energy. The first trap that was built during this work has a axial heating rate of 1.3(2) phonons per second at an axial confinement of 1 MHz. The second trap, which was used during the measurements presented in this work, has a heating rate of 37(2) phonons per second at the same axial confinement. The heating rate measurements are shown in figure 4.6. The reasons for the difference in the heating rate of the two traps are unknown. Different surface contamination due to a different treatment during the gold plating process could be responsible.

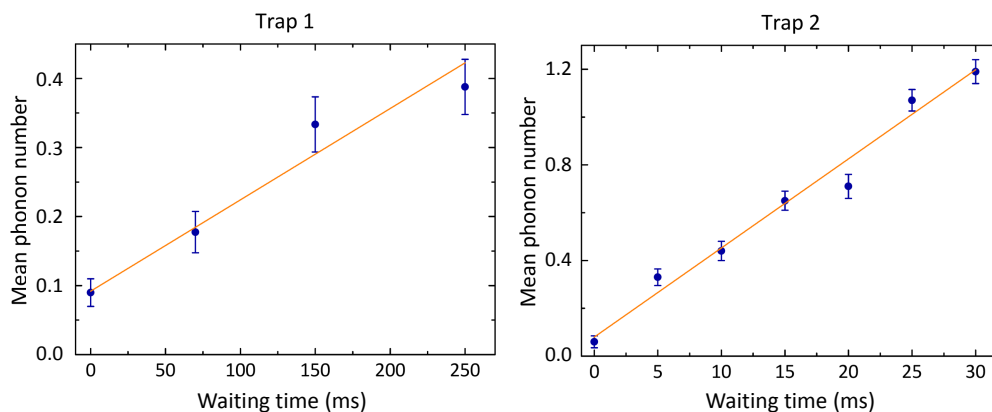


Figure 4.6: Axial heating rates of both traps at an axial confinement of 1 MHz. Trap 1 shows a heating rate of 1.3(2) phonons per second. The heating rate of trap 2 of 37(2) phonons per second is more than an order of magnitude higher. The heating rate was determined by comparing excitation of red and blue sideband for a given waiting time after ground state cooling.

4.1.2 Vacuum vessel

The main part of the ultra high vacuum (UHV) chamber containing the trap (see figure 4.7) is a stainless steel spherical octagon⁸. It has two big 100 mm and eight smaller 40 mm confocal flanges (CF). The mechanical connection between the trap holder and the octagon is done with a groove grabber⁹. Both CF100 and four of the CF40 flanges are equipped with fused silica viewports^{10,11} with an anti-reflective coating¹² for 267 nm, 397 nm and 729 nm to avoid losses and reflections inside the chamber. The reflectivity depending on the wavelength is presented in figure 4.8.

⁸Kimball physics MCF600-SphOct-F2C8

⁹Kimball physics MCF275-GrvGrb-CYL1000

¹⁰VACOM VPCF40DUVQ-L-NM

¹¹VACOM VPCF100DUVQ-L-NM

¹²Tafelmaier X/UIMCS6

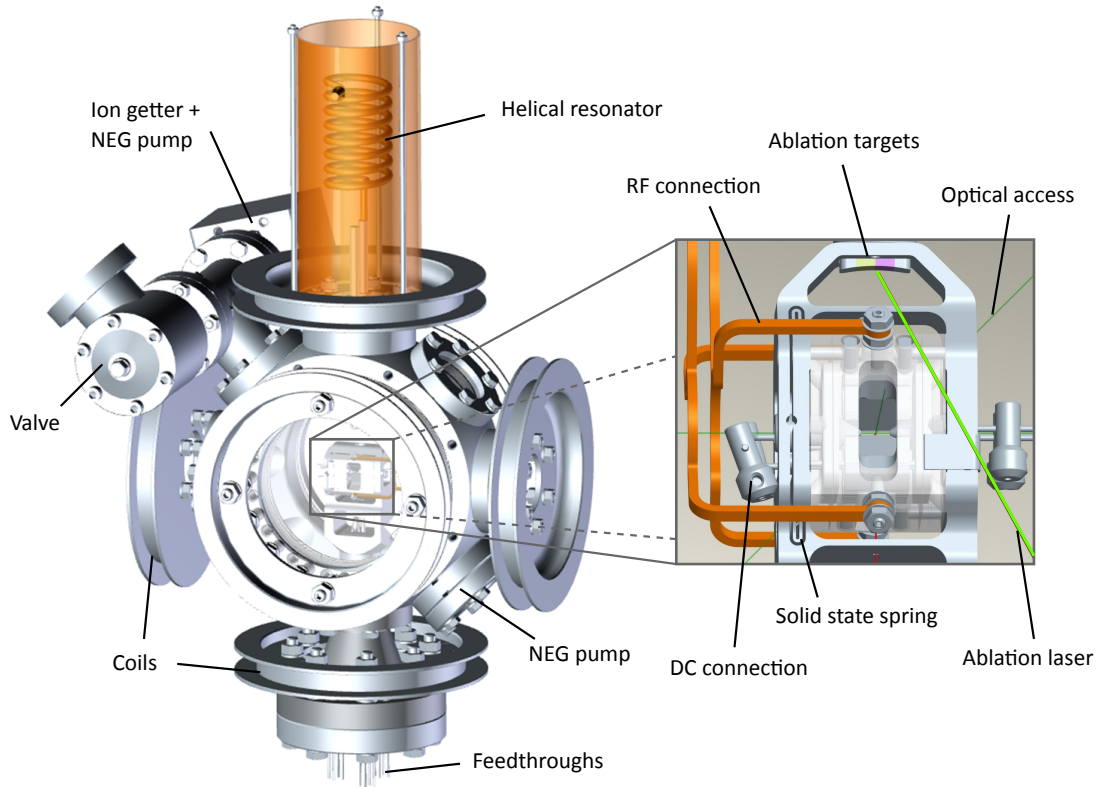


Figure 4.7: Drawing of the UHV chamber containing the trap. Electrical feedthroughs are attached at the top and bottom for the helical resonator providing the high voltage RF and the stable DC voltages respectively. To the bottom right and the top left two pumps are connected as well as a valve. Three coil pairs orthogonal to each other allow one to apply a quantization magnetic field and to compensate for magnetic stray fields perpendicular to the quantization axis. The remaining flanges have fused silica viewports with anti-reflective coatings.

Top and bottom flanges are used for RF¹³ and DC¹⁴ feedthroughs. All electrical connections inside the vacuum are done with oxygen free high conductivity copper (OFHC) wires, electrically isolated with aluminium oxide ceramic beads. The RF source for the trap drive is a frequency generator¹⁵ at 32.3 MHz, whose output is amplified¹⁶ to 1-2 W and coupled into the quarter wave helical resonator which amplifies the voltage by a factor of ~ 60 . The coupling is done via a sliding contact that is attached to a threaded teflon bar, that is screwed into the resonator coil. This has the advantage over the usual clip contact, that the impedance matching can be done while the grounding shield is closed. A reflectometer¹⁷ between ampli-

¹³VACOM CF40-HV25S-2-CE-CU64

¹⁴VACOM W-HV6-4-CE-CU13

¹⁵Rohde & Schwarz SML01

¹⁶Minicircuits LZY-22+

¹⁷Rohde & Schwarz power reflection meter NRT

fier and helical resonator shows the reflected power and therefore allows one to adjust the RF frequency to the resonance. The DC voltages for the endcap and compensation electrodes are provided from a stable high voltage source¹⁸ ($\Delta V/V \approx 10^{-5}$). Low pass filters with a cut-off frequency of 4 Hz directly at the feedthroughs suppress noise that is picked up on the cables.

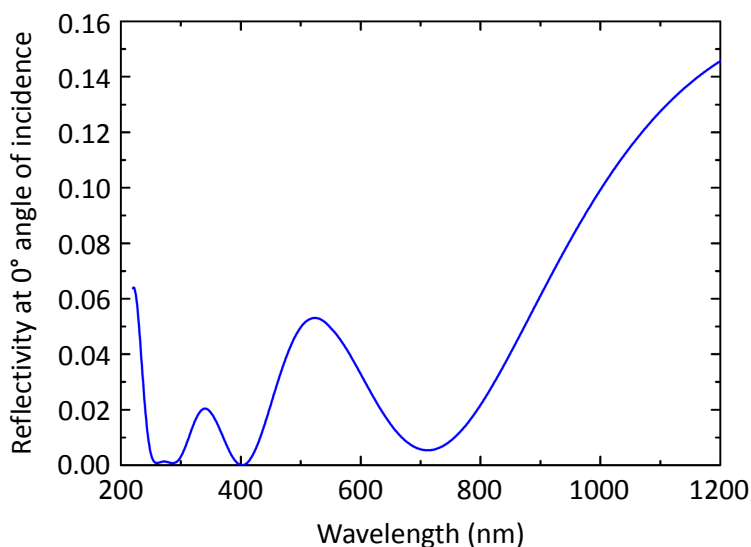


Figure 4.8: Reflectivity of viewport coatings at 0° angle of incidence depending on the wavelength. The reflectivities for the spectroscopy laser wavelengths around 267 nm and 729 nm as well as the Doppler cooling laser at 397 nm are well below 1 %.

An ION/NEG pump¹⁹ is attached to the CF40 tee-piece at the top west viewport as well as an all-metal angle valve. The remaining bottom east flange is used for a NEG pump²⁰, that is next to the trap. Before assembling the setup the in-vacuum steel parts and the gold-plated electrodes were air baked at 350 °C for one day. This passivates the steel surfaces by creation of an oxide layer and therefore reduces outgassing of hydrogen. After that all parts were carefully cleaned with acetone (except copper), isopropanol and methanol in an ultrasonic bath. After assembling the chamber it was baked for 1 week at 180 °C. Next, the NEGs were activated and the valve was closed. Finally the pressure settled down to 10^{-11} mbar. The pressure is measured with the ion pump current ~ 1 nA. A single ion collision rate of $\approx 0.3/min$ with the background gas was observed by analyzing the fluorescence counts while Doppler-cooling. This indicates, that the pressure at the trap is about $5 \cdot 10^{-11}$ mbar.

Three big and one small coil pair (see figure 4.7) provide the quantization axis and the compensation magnetic field. The three big pairs are designed to create a field of 5 G at the

¹⁸ISEG EHS8020x-K2

¹⁹SAES NEXTorrr D 100-5

²⁰SAES Capacitorrr D 100

ion's position at a current of 1 A. Due to practical reasons none of the coil pairs fulfills the Helmholtz criteria. The coils attached to the big viewports have 100 turns, the other ones have 220. An additional small pair of coils (see figure 4.1) in anti-parallel configuration along the trap axis allows one to compensate for a magnetic field gradient along an ion string. The current which is sent through the quantization coils is stabilized by a home-built PID regulator that contains a reference resistor²¹.

4.1.3 Magnetic field shielding

Fluctuating magnetic fields in the lab shift atomic energy levels and therefore affect coherent qubit operations as well as the stability of an optical atomic clock. In order to improve the magnetic field stability at the ion's position the vacuum chamber is enclosed in a magnetic shield²². It consists of a welded aluminium case lined with a double layer of a magnetic nickel-iron alloy²³. The box has a big front door and two smaller inspection doors on the sides that are usually closed. Several small holes in the back provide access for optical fibers and electrical cables. Four holes in the base serve to attach the trap setup directly to the optical table via electrically isolating posts.

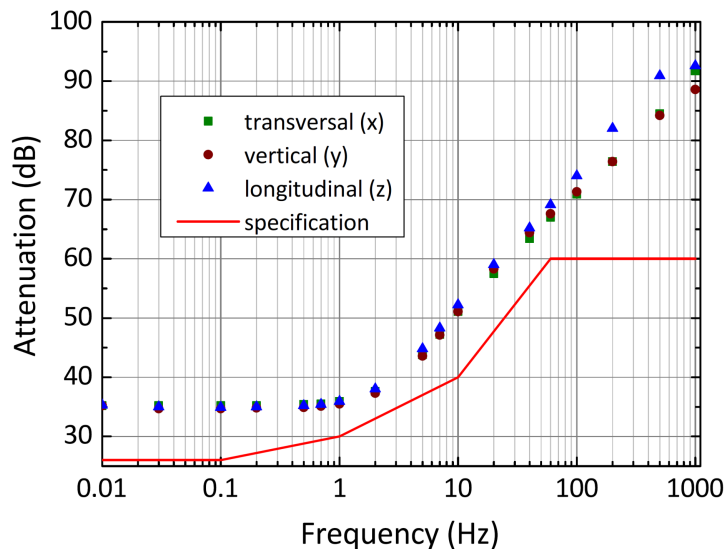


Figure 4.9: AC magnetic field attenuation in the center of the chamber measured by the manufacturer. Magnetic fields with frequencies below 1 Hz are attenuated by 35 dB. At a frequency of 50 Hz, which is the strongest component in the lab, an attenuation of more than 65 dB is obtained.

²¹Vishay VCS 302

²²IMEDCO AG

²³Magnifer by ThyssenKrupp

AC magnetic fields with frequencies ranging from 10 mHz to 1Hz are attenuated in the center of the box by 35 dB. For frequencies beyond 1Hz the screening effect increases linearly, reaching 65 dB at 50 Hz. The shielding effectiveness of the enclosure depending on the AC magnetic field frequency along all three directions is presented in figure 4.9. With this shield, magnetic field deviations within one line cycle could be reduced from 1 mG to 40 μG peak to peak. This was measured with Ramsey experiments that were synchronized to the AC power line and repeated for different delays with respect to the power line phase [29]. The currently limiting factors for the short term stability of the magnetic field of $\Delta B_{50\text{Hz}}/B \approx 10^{-5}$ are electrical cables running into the shielding. The long term magnetic field stability was measured with the clock script (see section 5.3) which was not synchronized to the AC power line. Therefore the line cycle induced fluctuations are averaged out. The progression of the magnetic field over a period of 100 minutes is shown in figure 4.10. The long term stability of the magnetic field of $\Delta B/B \approx 3 \cdot 10^{-6}$ is limited by the temperature stability of the PID regulator which stabilizes the current that is sent through the coils.

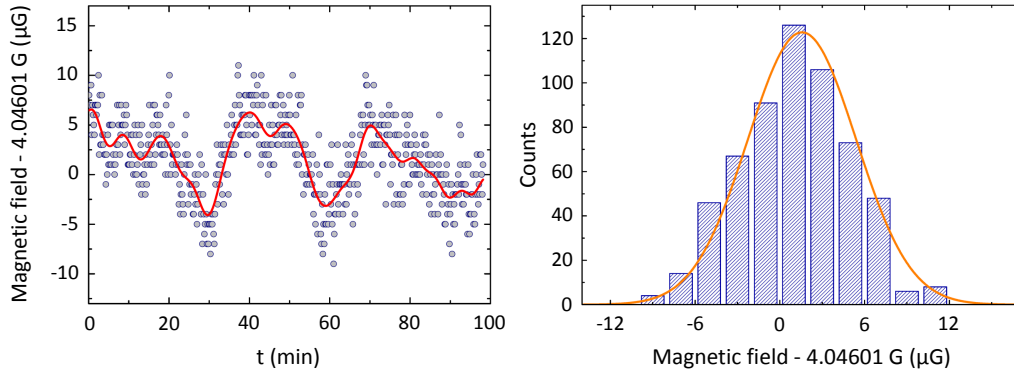


Figure 4.10: *Left: Magnetic field at the ion measured with a Ramsey experiment with a Ramsey time of 3 ms. Short term fluctuations of 5-10 μG peak to peak are visible. The red line is Fourier smoothed to highlight periodicities. The 10 μG modulation with a cycle time of ~ 30 min is caused by the air conditioning of the lab, which modulates the temperature of the current driver and therefore the temperature of the reference resistor inside [29]. Right: Histogram of the magnetic field with a bin size of 2 μG . The orange line is a Gaussian fit with 10 μG FWHM.*

4.1.4 Imaging system & state detection

The optical setup for imaging and fluorescence detection is identical with the one described in [29], where a detailed description of the detection method and the detection efficiencies is presented. In short, the discrimination between the internal $S_{1/2}$ and $D_{5/2}$ states in $^{40}\text{Ca}^+$ is done by electron shelving [49]. As long as the calcium ion is in the $S_{1/2}$ state, illuminating the ion with the 397 nm and 866 nm lasers will cause the ion to scatter 397 nm photons

which are detected by a photomultiplier or a camera. The ion is detected as “bright”. In the case of the ion being in the $D_{5/2}$ state no 397 nm photons will be scattered and the ion is detected as “dark”. Repeating the experiment n times leads to two different photon count distributions. These distributions correspond to the two cases described above and can be related to peaks in a histogram. The photon count distributions can be expressed by a Poisson distribution [60]. Typically the fluorescence counts are accumulated for a duration of 5 ms after each single experiment. For experiments with up to 4 calcium ions the internal states can be well discriminated but for longer ion strings a clear discrimination is no longer possible because of overlapping peaks in the histogram [29]. This problem is overcome by detection of spatially resolved fluorescence of individual ions on an EMCCD camera.

The collection of the ion’s fluorescence is done with a custom-made objective²⁴. The photons are guided to a PMT²⁵ and an EMCCD²⁶ camera. An optical band-pass filter²⁷ (transmission between 381 nm and 399 nm) and a variable slit²⁸ block stray light, entering the imaging path.

Since the camera pixel size (8 μm) and the equilibrium distance of two ions at a certain trapping confinement (see equation 2.10) are known, the magnification factor of the objective can be calibrated by determining the pixel-to-pixel distance of two fluorescing $^{40}\text{Ca}^+$ ions on the EMCCD camera image. The axial oscillation frequency of the ions was determined by modulating the axial confinement. If the modulation hits the resonance frequency of the center-of-mass mode, the ions oscillate around their equilibrium positions which can be seen on the EMCCD camera. The corresponding images are shown in figure 4.11. At an oscillation frequency of 199.1(1) kHz the calculated equilibrium distance yields 16.435(6) μm . The pixel-to-pixel distance of the ions is 56(0.5). Consequently the imaging system covers an area of 330 μm · 330 μm at the trap center with a magnification factor of ~ 27 .



Figure 4.11: Average of 100 EMCCD camera images each of two trapped calcium ions. a) two calcium ions resting at their equilibrium positions. b) modulation of the axial trapping confinement at the resonance frequency of 199.1(1) kHz. The calculated equilibrium distance for this confinement is 16.435(6) μm . The ion to ion distance in pixels which yields 56(0.5).

²⁴Silloptics $f = 66.8$ mm, $d = 34$ mm

²⁵Sens-Tech P25PC, quantum efficiency of $\sim 27\%$ at 397 nm

²⁶Andor iXon DV885JCs-VP, pixel size 8 x 8 μm , quantum efficiency of 37% at 397 nm.

²⁷Semrock SEM-FF01-390/18-25

²⁸Owis Spalt 40

4.2 Laser systems

A total of eleven different laser systems were used in this work. Each of them has its specific task and therefore the requirements in terms of spectral properties, power, etc differ. A list with all the laser systems and a short description of their application is presented in table 4.1. All of them are commercially available diode, fiber or solid state lasers. A description of all lasers setups is presented in the following section. Setting up laser systems for experiments with trapped calcium ions is now standard and described in detail in various theses [19,29,33–35,61]. For this reason the main focus of this section was laid on describing the laser systems, relevant for aluminium ions, as well as technical innovations.

Laser wavelength	Application
397 nm	Doppler cooling of $^{40}\text{Ca}^+$
854 nm	Repumping from the $D_{5/2}$ levels in $^{40}\text{Ca}^+$
866 nm	Repumping from the $D_{3/2}$ levels in $^{40}\text{Ca}^+$
423 nm	Photo-ionization of ^{40}Ca
394 nm	Photo-ionization of ^{27}Al
375 nm	Photo-ionization of ^{40}Ca
532 nm pulsed	Ablation of Ca and Al atoms
729 nm	Excitation of the $S_{1/2} \leftrightarrow D_{5/2}$ clock transition in $^{40}\text{Ca}^+$
267.0 nm	Excitation of the $^1S_0 \leftrightarrow ^3P_1$ intercombination transition in $^{27}\text{Al}^+$
267.4 nm	Excitation of the $^1S_0 \leftrightarrow ^3P_0$ clock transition in $^{27}\text{Al}^+$
Frequency comb	Frequency measurement of both clock lasers

Table 4.1: Listing of all laser systems implemented in the experimental setup as well as their application.

4.2.1 Lasers for Doppler-cooling, repumping, and photo-ionization

All laser systems for Doppler-cooling, repumping and photo-ionization are mounted on a breadboard, hanging under the optical table. A second breadboard accommodates the acousto-optic modulators for switching the light on and off within the experimental sequence. The lasers are stabilized to the wavelength-meter (see section 4.2.2) which is situated between the two breadboards.

397 nm cooling laser

The $S_{1/2} \leftrightarrow P_{1/2}$ dipole transition in $^{40}\text{Ca}^+$ at a wavelength of 397 nm is used for Doppler-cooling, optical pumping and state detection by fluorescence (electron shelving). The corresponding light source is a frequency-doubled external cavity diode laser²⁹ (ECDL) at a fundamental wavelength of 793 nm which is subsequently amplified by a tapered amplifier (TA). A schematic drawing of the 397 nm laser setup is presented in figure 4.12. Even though laser diodes at 397 nm are commercially available, their handling is more difficult and so the standard approach to produce this wavelength was chosen to have a low-maintenance system although it is more expensive. Furthermore these systems have the advantage of having a nicer beam profile and less amplified spontaneous emission (ASE). A few ten μW of the infrared light are sent via a single mode fiber to the Wavelength meter³⁰, to which the laser is stabilized to (see section 4.2.2). Approximately 12 mW of 397 nm light is guided to the AOM breadboard. It is frequency up-shifted by 160 MHz by the double-pass AOM³¹ 1 and subsequently split into two parts. A mechanical shutter that blocks the 0th diffraction order can be opened and the far red detuned light helps to recrystallize the ions after a collision with the background gas. The first path contains the main part of the light and passes the single-pass AOM³² 2 at 80 MHz, which enhances the attenuation when the light is supposed to be turned off and is coupled into a photonic crystal fiber together with the repumping lasers (see below).

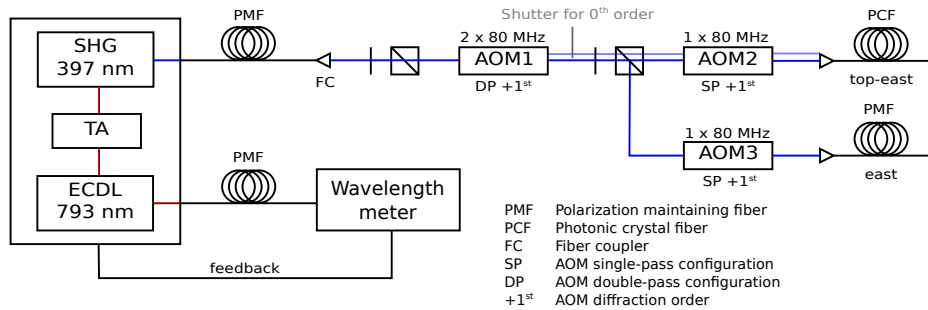


Figure 4.12: Schematic drawing of the 397 nm laser setup. Fundamental light at 793 nm, created by an ECDL, is amplified by a tapered amplifier and subsequently frequency doubled. A small fraction of it is sent to the wavelength meter for frequency drift compensation. The 397 nm light is split into two paths for Doppler-cooling and optical pumping. Black lines represent optical fibers, colored lines indicate free-space beam paths.

Light from this path is used for Doppler-cooling and state detection and has overlap with all three normal modes of an ion in the trap (see figure 4.1 top-east viewport). The beam is focused to a Gaussian beam waist of 100 μm FWHM at the ion. About 500 μW optical

²⁹Toptica TA-SHG pro

³⁰High Finesse WSU-2

³¹Crystal Technology Inc. 3080-120

³²Crystal Technology Inc. 3080-120

power is available at the trap. The second path which contains a small fraction of the light also passes the 80 MHz single-pass AOM³³ 3 and is coupled to a polarization maintaining fiber that reaches the west-viewport. A quarter wave-plate in front of the trap creates circularly polarized light and allows for optical pumping. A detailed description of the pumping scheme can be found in [29]. The Gaussian beam waist at the ion is also 100 μm FWHM.

854 nm & 866 nm repumping laser

Two external cavity diode lasers³⁴ at 854 nm and 866 nm provide light for repumping from the metastable $D_{5/2}$ and $D_{3/2}$ states, respectively. Both laser beams are guided by single-mode fibers to the AOM breadboard. A schematic drawing of the 854 nm and 866 nm laser setup is presented in figure 4.13. A small fraction of each laser beam is split off and sent via single-mode fibers to the WLM for the purpose of frequency drift compensation. The main fraction of both laser outputs pass the 200 MHz double-pass AOMs³⁵ 4&6 and the 80 MHz single-pass AOMs³⁶ 5&7 and are coupled to a photonic crystal fiber together with the 397 nm cooling beam (see above). Beam waists and optical powers at the trap are identical with the 397 nm cooling beam.

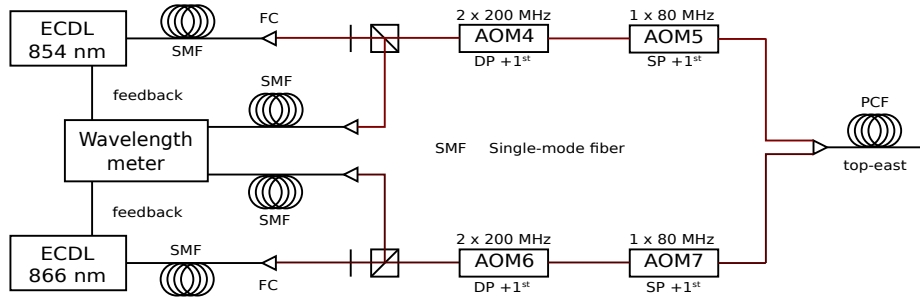


Figure 4.13: Schematic drawing of the 854 nm and 866 nm laser setups. In both cases a small fraction of the light is sent to the wavelength meter (WLM) for frequency drift compensation. The main fraction of the light is sent via a photonic crystal fiber (PCF) to the ions after passing AOMs that allow one to switch the beams on and off.

Photo-ionization lasers at 423 nm, 394 nm and 375 nm

The creation of singly positively charged ions from neutral Ca and Al atoms is done via two-step photo-ionization (PI). In case of calcium an external cavity diode laser³⁷ at 423 nm excites the $^1S_0 \leftrightarrow ^1P_1$ transition. A photon from a free running 375 nm diode laser³⁸ excites the

³³Crystal Technology Inc. 3080-120

³⁴Toptica DL pro

³⁵Crystal Technology Inc. 3200-125

³⁶Crystal Technology Inc. 3080-122

³⁷Toptica DL pro

³⁸Toptica iBeam smart

atom to an energy above the ionization threshold of 6.1 eV [54]. In the case of aluminium an ECDL³⁹ at 394 nm excites the ${}^2P_{1/2} \leftrightarrow {}^2S_{1/2}$ transition (See also section 5.1). Another 394 nm photon is sufficient to reach the ionization threshold of 6 eV [54]. The laser can be also tuned to the ${}^2P_{3/2} \leftrightarrow {}^2S_{1/2}$ transition at 396 nm. A level scheme of neutral aluminium containing the relevant levels for photo-ionization is presented in figure 4.14. More detailed information about the level structure of neutral aluminium, including the hyperfine structure, can be found in [62] .

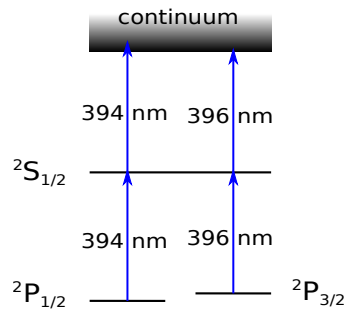


Figure 4.14: Level structure of neutral aluminium containing the relevant levels for photo-ionization. The hyperfine structure is not shown. Starting in the electronic ground state ${}^2P_{1/2}$ a 394 nm photon excites the atom to the ${}^2S_{1/2}$ intermediate state. Another 394 nm photon is sufficient to reach the ionization threshold of 6 eV. However, at temperatures that are required to evaporate aluminium atoms from bulk material the ${}^2P_{3/2}$ state is also populated [63]. This enables a second way of photo-ionization via two 396 nm photons.

A schematic drawing of the PI laser setup is presented in figure 4.15. The light from both ECDLs (423 nm and 394 nm) is guided to the AOM breadboard via single mode fibers. There, a small fraction of both beams is split off and sent to the WLM via single mode fibers for the purpose of frequency drift compensation. The 80 MHz single-pass AOM⁴⁰ 8 in the 394 nm path allows for a precise temporal delay of the PI laser with respect to the ablation pulse (see section 5.1). 375 nm light, which is produced by a free running laser diode, is guided via a multi-mode fiber to the AOM breadboard. Finally, all three beams are coupled into a single-mode fiber that goes to the trap. The beams have Gaussian beam waists of about 100 μm FWHM at the trap center. Typically 500 μW optical power of each laser is available at the trap. A mechanical shutter in front of the fiber allows us to switch all beams on and off.

³⁹Toptica DL pro

⁴⁰Crystal Technology Inc. 3080-120

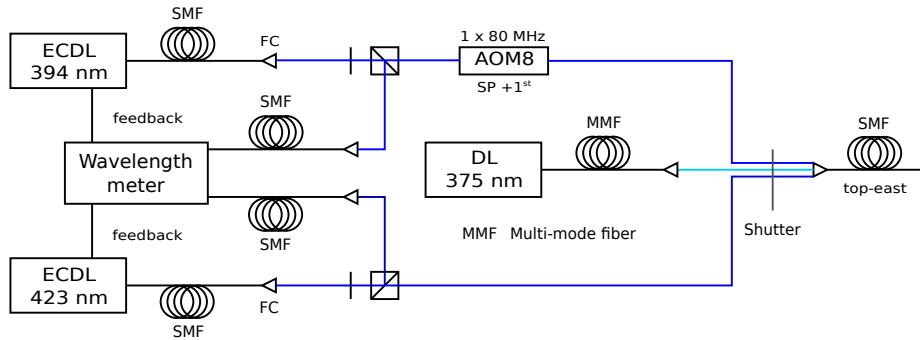


Figure 4.15: Schematic drawing of the photo-ionization laser setup. In the cases of the 394 nm and 423 nm lasers a small fraction of the light is sent to the wavelength meter for frequency drift compensation. The main fraction of both laser outputs is combined with the 375 nm light and sent to the trap. An AOM in the 394 nm path allows for switching the light on and off on the μs timescale.

Ablation laser

In this work laser ablation loading of calcium and aluminium ions was implemented (see section 5.1). Therefore neutral atoms of both species are evaporated from ablation targets by single laser pulses. The atoms are subsequently photo-ionized in the center of the trap. A schematic drawing of the ablation laser setup is presented in figure 4.16.

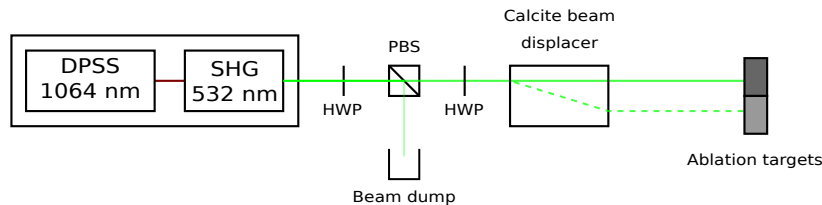


Figure 4.16: Schematic drawing of the ablation laser setup. The energy of the laser pulses is adjusted by a half-wave plate and a polarizing beam splitter. A calcite beam displacer sends the laser pulses along two different paths depending on their polarization, which allows one to address the two ablation targets individually.

The laser system is a frequency-doubled diode-pumped solid state laser (DPSS)⁴¹, which emits laser pulses at a wavelength of 532 nm. The pulses have a fixed pulse energy of 400 μJ and a temporal duration of 2 ns. Single pulses are triggered via transistor-transistor logic (TTL). For optimizing the probability of creating one ion per ablation pulse, the energy of the ablation pulses, sent to the targets, needs to be adjusted. This can be achieved by a half-wave plate followed by a polarizing beam splitter in the beam path. Furthermore two different targets for the two atomic species, respectively are mounted above the trap, which have to

⁴¹Coherent flare 532

be addressed individually. This is realized by a half-wave plate and a calcite beam displacer⁴². Depending on the polarization of the ablation pulse the beam displacer allows one to switch between two separate beam paths that individually address the two targets in the vacuum chamber.

4.2.2 Wavelength meter & wavelength control

Nearly all laser wavelengths used in the experiment are monitored and some of them are controlled with a wavelength meter (WLM)⁴³, which is based on a Fizeau interferometer. It has two fiber ports that are normally used for measurement and calibration. A four-channel micro electro-mechanical system (MEMS) fiber switch with a lifetime of more than 10^9 cycles of operation is attached to the first port. It is used to measure the wavelengths of the 793 nm, 854 nm and 866 nm lasers periodically at a rate of 50 Hz. A control program⁴⁴ calculates an error signal proportional to the deviation from the target wavelength and a digital-analog-converter (DAC) on an associated PCI card generates a DC voltage proportional to the error signal. Before the DC voltage is fed back to the piezo of the ECDLs, it is scaled down by variable voltage dividers to refine the voltage steps resulting from the finite resolution of the DAC and 50 Hz low pass filtered to suppress noise with frequencies above the control bandwidth. The variable voltage dividers are set such that the frequency resolution is as fine as possible without limiting the tuning range that is required to compensate for typical frequency drifts of the lasers. Typical ratios are 1:3-4.

This setup corrects for laser frequency drifts but it is not able to narrow the ECDL's free running linewidth of about 200 kHz. In view of the natural linewidth of the transitions, driven by the 397nm, 854nm and 866nm laser, which are on the order of 20 MHz, the lasers are sufficiently stable. Furthermore this setup renders the use of additional reference cavities unnecessary.

An 8-channel mechanical switch with a lifetime of about 10^8 cycles of operation is connected to the calibration port. The mechanical switch is used to monitor the residual laser wavelengths (729 nm, 1068 nm, 1069.6 nm, 423 nm and 394 nm). It has the advantage of resisting UV wavelengths, which the MEMS switch is not capable of. The shorter lifetime compared to the MEMS switch is no drawback since it is only used occasionally.

The WLM can be calibrated automatically with the 729 nm laser when it is referenced to the calcium ion. The calibration can be done periodically on any desired time scale which allows one to eliminate drifts due to temperature changes of the WLM. For typical calibration intervals of 10 minutes the laser frequencies are stable within less than 1 MHz. This was observed by

⁴²Thorlabs BD40

⁴³HighFinesse WSU/2

⁴⁴HighFinesse Laser Control PID

monitoring the frequency of the stable 1068 nm laser. Consequently the frequencies of the cooling and repumping lasers only need to be adjusted to the corresponding transitions once per day.

4.2.3 Ultra-stable lasers

Driving narrow transitions coherently requires light sources with a linewidth on the order of the natural linewidth of the transition. The clock transitions of $^{27}\text{Al}^+$ and $^{40}\text{Ca}^+$ have natural linewidths of $2\pi \cdot 7.6$ mHz and $2\pi \cdot 139$ mHz, respectively. Therefore, the 267.4 nm and 729 nm lasers are stabilized to optical resonators with high finesse, which are temperature-stabilized and vibration-isolated from the environment. In practice, the limiting factor for narrowing the linewidth of a laser is the thermal noise floor of the reference cavity (typically $\sim 10^{-15}$). Consequently, spectral laser linewidths on the order of 1 Hz are achievable.

The intercombination transition of the $^{27}\text{Al}^+$ ion has a natural linewidth of $2\pi \cdot 520$ Hz. Driving this transition coherently does not require a 1 Hz laser, but it is advantageous to have another ultra-stable laser at 267 nm which the 267.4 nm clock laser can be compared to. The laser systems are located in the labs, the three high-finesse cavities are placed inside a wooden box in the basement due to a lack of space in the lab.

In the following the three ultra-stable lasers at 729nm, 267.0 nm and 267.4 nm are described. This subsection is structured as follows: First, an overview of the optical setup of each laser system is given which includes schematical drawings of those. Second, the method of Pound-Drever-Hall (PDH) laser stabilization is introduced and a description of the PDH setup is given. Furthermore the spectral properties of both 267 nm lasers are characterized. A characterization of the 729 nm laser can be found in [61].

729 nm laser

An ultra-stable titanium-sapphire laser (Ti:Sa) with a short term linewidth of 1 Hz [61], which is located in lab 1 is used to coherently drive transitions between the $S_{1/2}$ and $D_{5/2}$ manifolds. It can be used to manipulate the ion's internal and motional state with high fidelity [29, 32, 35] using carrier and sideband transitions. A detailed description of the current setup in lab 1 can be found in [29] and references therein.

A 10 m long polarization maintaining fiber (APC end), whose optical path length is stabilized, guides 15 mW of the light to lab 2. A schematic drawing of the 729 nm laser setup is presented in figure 4.17. The light is sent through the 80 MHz AOM⁴⁵ 12 (+1st order) followed by a wedge, which is used to reflect 4 % of the light back into the fiber. An interferometer in lab 1 is used for fiber noise cancellation (FNC). The stable light is used to seed a tapered amplifier⁴⁶ with a maximum output power of 560 mW. The 80 MHz AOM⁴⁷ 13 (-1st order) cancels the frequency offset and can be used for intensity stabilization (PD 5) and locking the

⁴⁵Crystal Technology Inc. 3080-120

⁴⁶Toptica TA 100

⁴⁷Crystal Technology Inc. 3080-120

laser to the spherical cavity⁴⁸, located in the basement.

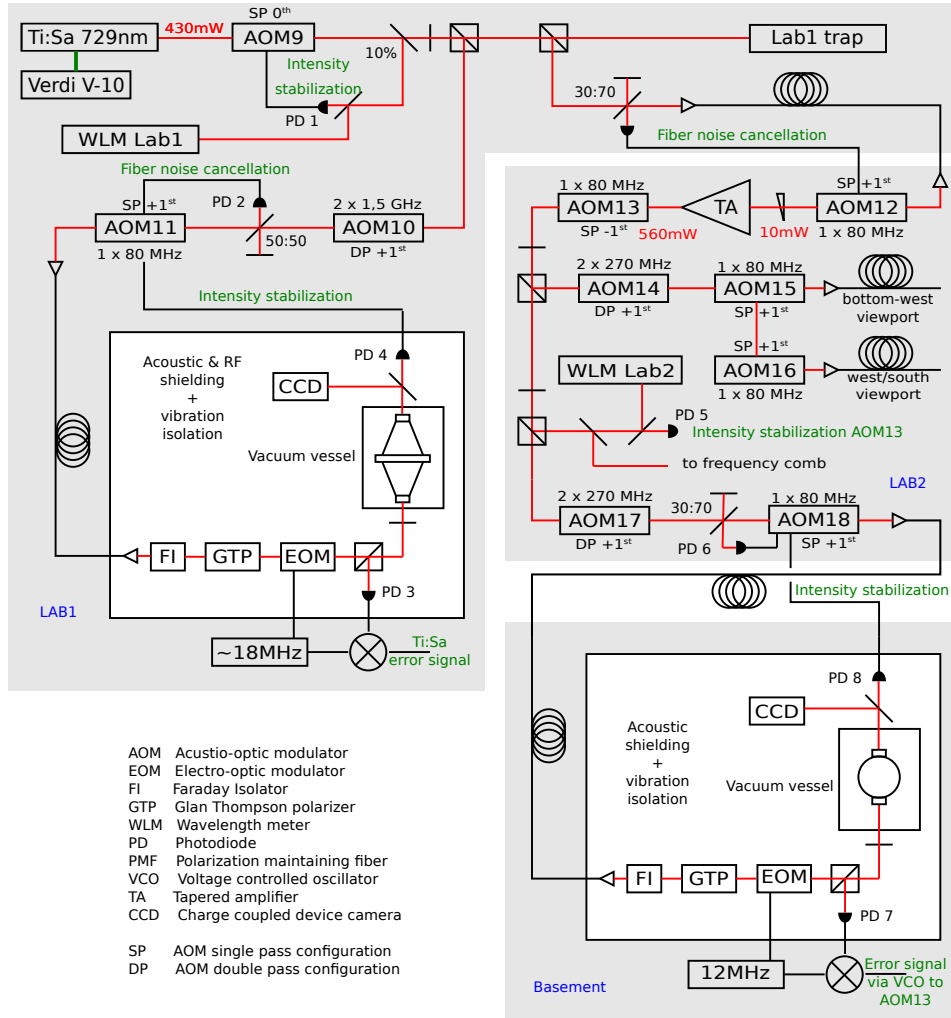


Figure 4.17: Schematic overview of the 729 nm laser setup. It is spread over three different locations. The laser itself and the PDH locking setup (vertical cavity) is located in lab 1. A part of the light is split off and sent to lab 2 where a tapered amplifier provides 560 mW of power. Afterwards the light is distributed among different paths that go to the experiment, the wavelength meter, intensity stabilization and the Pound-Drever-Hall setup located in the basement.

The main fraction of the light is going into the 270 MHz double-pass AOM⁴⁹ 14, which is used to bring the laser frequency into resonance with the Zeeman transition to be excited. The 80 MHz single pass AOMs⁵⁰ 15&16 in a row allow one to send the light to different ports at the trap and two 2 m long PM fibers guide the light to the ions.

⁴⁸ATF 6300 spherical cavity

⁴⁹Brimrose TEF 270-100-729

⁵⁰Crystal Technology Inc. 3080-120

The fraction of the light, which is not going into AOM 14, is used for an optical beat note with the frequency comb (see section 4.2.4), for the PDH locking setup in the basement, for laser intensity stabilization (PD 5) and calibrating the wavelength meter. The main part of the light passes the 270 MHz double pass AOM⁵¹ 17, which is used to compensate for the cavity drift, an interferometer (FNC) and the 80 MHz single pass AOM⁵² 18 for laser intensity stabilization (PD 8) and fiber noise cancellation. The rest of the light is sent to the wavelength meter and to a photo diode (PD 5) for laser intensity stabilization.

The spherical cavity has a finesse of $\mathcal{F} \approx 200.000$ which was measured by cavity ring-down spectroscopy and shows a drift rate of 50 mHz/s. Since the Ti:Sa is already phase-stabilized by the PDH setup in lab 1, the PDH setup in the basement is currently not used to lock the 729 nm laser to the spherical cavity. Nevertheless it provides the ability to be independent of the 729 nm laser in lab 1.

267.0 nm laser

To drive the $^1S_0 \leftrightarrow ^3P_1$ intercombination line in $^{27}\text{Al}^+$ an ultra stable laser at 267.0 nm with a maximum output power of 18 mW is used. The laser setup consists of a frequency quadrupled ECDL⁵³, which is locked to an external high finesse cavity⁵⁴ at its fundamental wavelength of 1068 nm. The spherical cavity has a finesse of $\mathcal{F} \approx 300.000$ and shows a drift rate of 46 mHz/s. A schematic drawing of the 267.0 nm laser setup is presented in figure 4.18. Coarse wavelength tuning is done via manually aligning the grating of the ECDL. A piezo actuating on the grating is used for fine tuning of the wavelength and for compensation of drifts and low frequency noise. Frequency stabilization with high bandwidth is done by a commercial PID controller⁵⁵ that feeds back to the laser diode current. The lock setup consists of the double pass AOM⁵⁶ 19 for frequency mode matching and cavity drift compensation and the 80 MHz AOM⁵⁷ 20 for fiber noise cancellation (PD 9) and laser intensity stabilization (PD 10). A 10 m long fiber guides the light to the PDH setup in the basement, which is described later. The error signal (PD 11) is fed into the fast analog linewidth control (FALC) with a slow and a fast locking branch. The slow part feeds back onto the piezo, the fast part on the laser diode current.

A linewidth of less than 1.63 Hz FWHM at 4 s was observed (see figure 4.24) by an optical beat note with the stable fiber laser (see below). However, there is broad-band high frequency noise that can not be fully compensated due to a relatively low control loop bandwidth of about

⁵¹Brimrose TEF 270-100-729

⁵²Crystal Technology Inc. 3080-120

⁵³Toptica DL TA FHG pro

⁵⁴ATF 6300 spherical cavity

⁵⁵Toptica FALC

⁵⁶Brimrose TEF 270-100-1068

⁵⁷Crystal Technology Inc. 3080-197

500 kHz. The locking bandwidth is limited by the modulation input or the diode current driver of the laser. This is proved by a phase delay measurement.

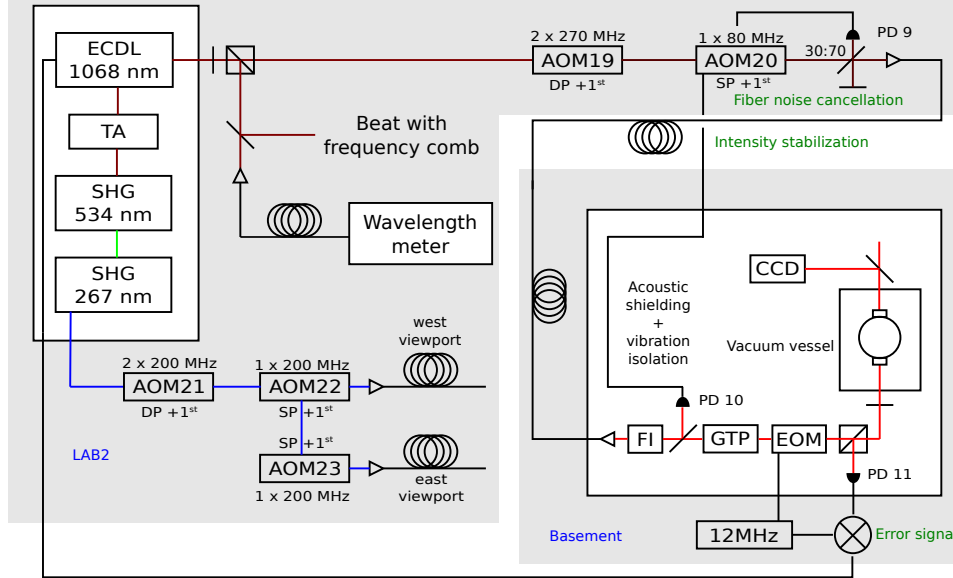


Figure 4.18: Schematic overview of the 267.0 nm lasers setup. An external cavity diode laser emits radiation at 1068 nm which is sent to a tapered amplifier. A fraction of the infrared light is split off and sent to the wavelength meter and the Pound-Drever-Hall setup located in the basement. The main part of the light is frequency-quadrupled and guided to the experiment.

The laser diode current was amplitude-modulated, which leads to a frequency modulation of the laser, and the laser light was sent through a low-finesse cavity⁵⁸. At a wavelength of 1068 nm the reflectivity of the cavity mirrors is $\leq 50\%$, which leads to a finesse of $\mathcal{F} \lesssim 10$. While sitting on the slope of the cavity resonance the transmitted light gets amplitude modulated which is detected with a photodiode. The relative phase between the diode current modulation and the photodiode signal is presented in figure 4.19. At a modulation frequency of 300 kHz the phase delay is already 90° and reaches 180° around 1 MHz. Additional phase delays from the PID controller and finite cable lengths are expected. Consequently, the control bandwidth is expected to be substantially smaller than 1 MHz. However, an additional $50 \mu\text{F}$ capacitor in parallel to the laser diode current reduced the high-frequency noise without decreasing the control bandwidth notably. The stable light at 1068 nm gets subsequently frequency-quadrupled.

The light at 267 nm passes the 200 MHz double-pass AOM⁵⁹ 21, which is used to adjust the laser frequency to the Zeeman transition to be excited and is sent to the 200 MHz single-pass

⁵⁸Toptica FPI 100-0750-1

⁵⁹Crystal Technology Inc. 3200-1220

AOMs⁶⁰ 22&23 in a row, that split the light into two paths.

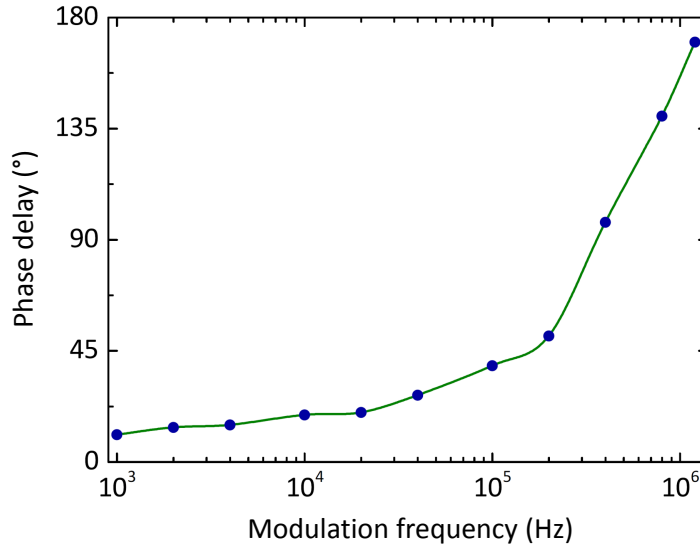


Figure 4.19: Phase delay of the laser diode response with respect to the modulation signal. The green line is a Bezier interpolation. A phase delay of 90° is already reached at a frequency of 300 kHz and reaches 180° around 1 MHz. From this measurement servo bumps around 1 MHz are expected. Additional phase delays result from finite cable lengths in the lock setup and the PID circuit itself which further decrease the control bandwidth.

Solid-core photonic crystal fibers guide the light to the east and west viewport. These fibers have low losses in the UV due to a modification of the color centers in the material [64]. This is achieved by loading the fiber with hydrogen gas under pressure and illuminating it with UV light afterwards. Typically 1.5 mW optical power is available at the trap. The beam is focused to a Gaussian beam waist of 65 μm FWHM at the ion.

267.4 nm laser

The ultra-stable 267.4 nm laser setup, which is used to drive the $^1\text{S}_0 \leftrightarrow ^3\text{P}_0$ transition in $^{27}\text{Al}^+$, consists of a frequency-quadrupled⁶¹ fiber laser⁶², which is locked to an external high finesse cavity⁶³ at its fundamental wavelength of 1069.6 nm. The cylindrical cavity has a finesse of $\mathcal{F} \approx 405.000$ and shows a drift rate of 100 mHz/s. The optical setup is almost identical with the one described above. A schematic drawing of the 267.4 nm laser setup is presented in figure 4.20. Typically the laser provides 30 mW of 267.4 nm light. Coarse

⁶⁰Crystal Technology Inc. 3200-1220

⁶¹Toptica FHG standalone

⁶²Menlo Systems orange one

⁶³ATF6020 notched cavity

wavelength pre-tuning is done via the fiber temperature. A piezo actuating on the fiber is used for fine tuning of the wavelength and for compensation of drifts and low frequency noise. A fiber AOM⁶⁴ between seed laser and fiber amplifier allows for frequency stabilization with high bandwidth.

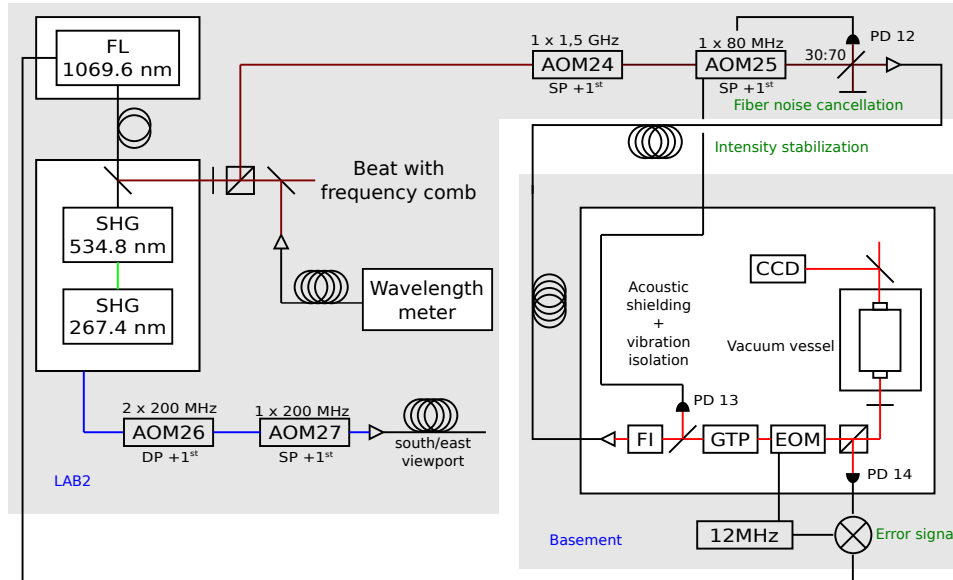


Figure 4.20: Schematic overview of the 267.4 nm lasers setup. A fiber laser emits radiation at 1069.6 nm which is sent along a polarization maintaining single mode fiber to a standalone fourth harmonic generation setup. A fraction of the infrared light is split off after the fiber and sent to the wavelength meter and the Pound-Drever-Hall setup located in the basement. The main part of the light is frequency-quadrupled and guided to the experiment.

The lock setup consists of the GHz AOM⁶⁵ 24 for frequency mode matching and cavity drift compensation and the 80 MHz AOM⁶⁶ 25 for fiber noise cancellation (PD 12) and laser intensity stabilization (PD 13). A 10 m long fiber guides the light to the PDH setup in the basement. The error signal (PD 14) is fed into a homemade PID controller⁶⁷ with a slow and a fast locking branch. The slow part feeds back onto the piezo, the fast part is sent to a low-noise voltage controlled oscillator (VCO)⁶⁸ that provides the driving frequency for the fiber AOM inside the laser. The locking bandwidth of 100 kHz is limited by the modulation bandwidth of the VCO. A linewidth of less than 1.63 Hz FWHM at 4 s was achieved (see figure 4.24). The stable light at 1069.6 nm gets frequency-quadrupled afterwards.

⁶⁴Gooch & Housego T-M150-0.4C2G-3-F2P

⁶⁵Brimrose GPF 1500-1000-1068

⁶⁶Crystal Technology Inc. 3080-197

⁶⁷Built by Gerhard Hendl

⁶⁸Vectron VS-705-ECE-SAAN-150M000000

The 267.4 nm light is sent to the 200 MHz double-pass AOM⁶⁹ 26, which is used to bring the laser frequency into resonance with the Zeeman transition to be excited, and subsequently passes the 200 MHz single-pass AOM⁷⁰ 27. A solid-core photonic crystal fiber guides the light to the south or east viewport. Laser power and beam waist at the trap are identical with the one described above.

Pound-Drever-Hall locking setup

All three spectroscopy lasers (729 nm, 267.0 nm and 267.4 nm) are phase-stabilized to external high-finesse resonators via the Pound-Drever-Hall (PDH) method [65, 66] which became a standard technique in the field of quantum optics and precision spectroscopy. The method and the required optical setup is described in numerous theses and articles i.e. [33, 34, 61, 67] just to name a few. Therefore the following description is restricted to a short summary.

The optical setup is identical for the three lasers mentioned above. Faraday isolators⁷¹ avoid disturbing back-reflections of the laser beam to the light source and Glan-Thompson polarizers⁷² keep the linear polarization as pure as possible. Next, electro-optic modulators⁷³ (EOM) phase-modulate the laser at the drive frequency (~ 12 MHz). The light passes a polarizing beam splitter and a quarter wave-plate before it enters the cavity. The polarization of the laser light in front of the EOM needs to be aligned to its crystal axis in order to minimize polarization modulation (at the drive frequency), which results in amplitude modulation after the PBS. Significant residual amplitude modulation leads to an unwanted frequency modulation of the laser due to the intensity modulation of the light on the PDH photo diode. Approximately 50 % of the light is coupled into the cavity (TEM₀₀ mode). The reflected part of the light passes the quarter wave plate again and is reflected by the PBS to fast photo diodes (PD 7⁷⁴ in figure 4.17, PD 11⁷⁵ in figure 4.18 & PD 14⁷⁶ in figure 4.20).

To obtain the PDH error signal [65, 66] when the laser frequency is scanned over the cavity resonance, the photo diode signal is mixed with the EOM drive frequency. The steepest slope of the error signal at the zero point is achieved with a modulation depth of 42% [65].

The error signal is fed into a PID controller which acts on different feedback elements depending on the laser. About 30% of the incident beam power gets transmitted through the cavity for optimized PID parameters.

A small fraction of the light inside the cavity is absorbed by the mirror coatings which

⁶⁹Crystal Technology Inc. 3200-1220

⁷⁰Crystal Technology Inc. 3200-1220

⁷¹Isolation > 35 dB

⁷²B. Halle, 10^{-8} extinction ratio

⁷³Linos PM-C-BB

⁷⁴Thorlabs DET10A/M

⁷⁵Thorlabs PDA10CF-EC

⁷⁶Thorlabs PDA10CF-EC

leads to local heating of those. The resulting thermal expansion of the coatings decreases the effective cavity length and thus changes the resonance frequency of the cavity. This response depending on the incident beam power is presented in figure 4.21 for the two infrared cavities.

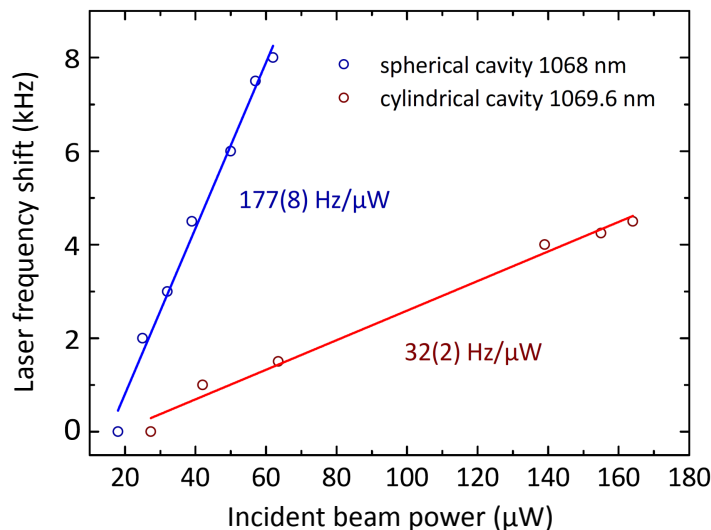


Figure 4.21: Laser frequency shift depending on the optical power of the incident beam for both infrared high-finesse cavities. The frequency shift is presented with respect to the lowest point in power. The difference in the slope can be partially explained by a factor of 2 in cavity length as well as a slightly smaller spot size of the cavity mode at the planar mirror of the spherical cavity (116 μm and 138 μm at $1/e^2$ intensity).

Therefore the laser intensity inside the cavity has to be stabilized⁷⁷. In the case of the 729 nm laser a photo diode (PD 8⁷⁸) in transmission is used. Due to the relatively low sensitivity of the photo diodes (PD 10⁷⁹ & PD 13⁸⁰) at the infrared wavelengths compared to 729 nm, the stabilization is done right after the Faraday Isolators for both aluminium lasers. Fractional intensity instabilities of 10^{-4} are achieved.

Another important point in order to achieve the ultimate laser stability is the temperature stabilization of the reference cavities. The target temperature is given by the so called zero crossing temperature (T_C) of the Ultra-Low Expansion glass (ULE), which the cavity spacer is made of. This is the point where the thermal expansion coefficient changes its sign and the linear part vanishes. The zero crossing temperatures of all three cavities are shown in figure 4.22.

⁷⁷SRS SIM960

⁷⁸Thorlabs PD10A

⁷⁹Hamamatsu G12180-010A

⁸⁰Hamamatsu G12180-010A

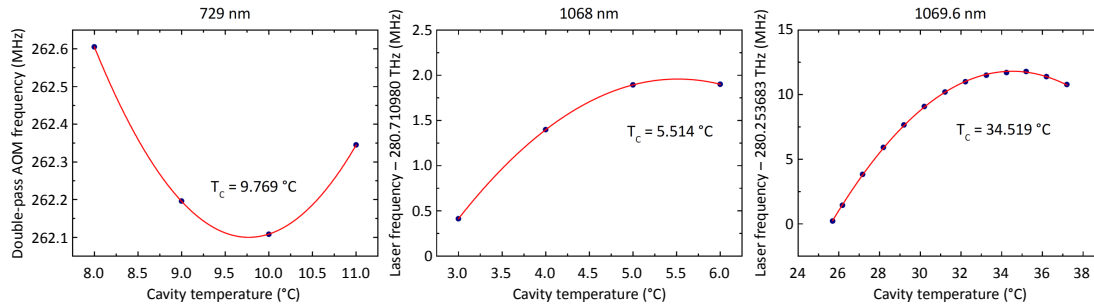


Figure 4.22: *Measurements of the zero crossing temperatures for the three high finesse cavities. The data represents the cavity length depending on its temperature. At the point where the coefficient of thermal expansion changes its sign, the linear part vanishes. At this point laser frequency changes due to temperature changes of the cavity are minimal. In the case of the 729 nm cavity the laser was locked to the ion and the double pass AOM was adjusted to resonance. The positive curvature arises from the fact that the -1^{st} diffraction order of the AOM was used. In the case of the two infrared cavities the laser frequency was measured with the frequency comb.*

A further important point is the isolation from acoustic noise present in the lab. The cavity spacer slightly changes its shape when it experiences accelerations which results in a change of the cavity length and therefore influences the laser frequency. For acoustic shielding a wooden box was built which rests on Sorbothane⁸¹ sheets in the basement. To avoid electromagnetic pick up, the outside of the box was lined with copper-wallpaper. The inside of the box is lined with lead rubber to increase its weight and therefore lower its natural frequency and acoustic foam to break sound waves. The box is filled with 10 cm quartz sand (grain size 1 mm) to damp acoustic vibrations. Two active vibration isolation platforms⁸² rest on the sand. One of them carries both spherical cavities for 729 nm and 1068 nm, the other one accommodates the cylindrical cavity for 1069.6 nm.

The temperature stabilization of the spherical cavities is done with a commercial temperature controller⁸³ that acts on Peltier elements inside the vacuum vessels. The cylindrical cavity is temperature-stabilized with a commercial temperature controller⁸⁴ that is connected to a resistive heater outside the vacuum can but within the heat shield. Typical temperature stabilities of ± 200 μK (in loop) are achieved for all three cavities.

During the optimization of the laser locks it is necessary to identify noise sources by their characteristic frequencies. Typically this is done via a beat note with a laser that is known to be stable. If there is only one noise source modulating the phase of one laser at a particular

⁸¹Visco-elastic polymer, used for vibration isolation (<http://www.sorbothane.com/>)

⁸²ACCURION halcyonics micro60

⁸³SRS PTC10

⁸⁴Wavelength Electronics LFI 3751

frequency, a sideband at the modulation frequency shows up on the beat signal spectrum. Depending on the modulation depth also higher order sidebands at harmonic frequencies can appear. As soon as both lasers are affected by several noise sources, this method breaks down since only a broad peak will be visible on the beat spectrum. Therefore it is useful to extract the phase noise spectrum of the beat. This can be done by detecting the beat note (212 MHz in this case) with a fast photo diode and mixing it down to about 10 kHz with two identical RF signals while one is phase shifted with respect to the other one by 90° (quadrature term). Consequently two beat signals at 10 kHz with a relative phase of 90° emerge, which are recorded by a fast oscilloscope. The quadrature term is needed to get the complete information about the phase evolution and to isolate amplitude noise. Subsequently the linear term in the phase evolution, which results from the non-zero beat frequency, is subtracted and a fast Fourier transform (FFT) leads to the phase noise $S_\varphi(f)$. More detailed information about the method can be found in reference [68]. The phase noise power spectral density of both aluminium lasers is presented in figure 4.23.

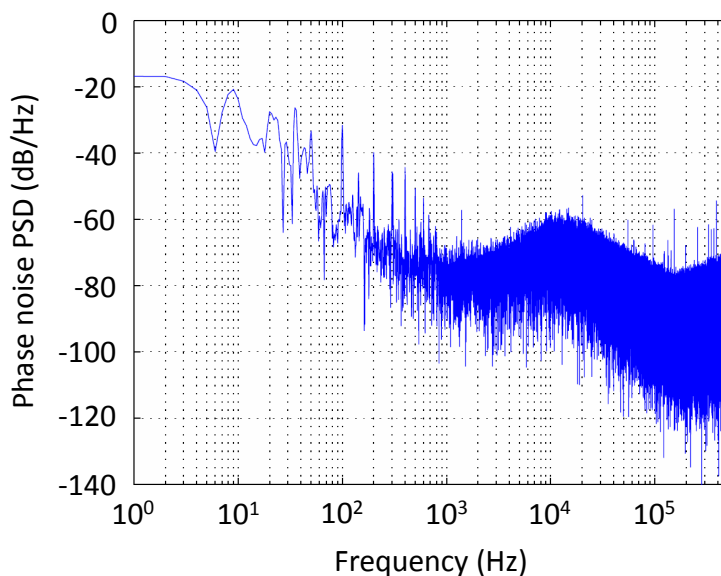


Figure 4.23: Phase noise power spectral density of both aluminium lasers at 1069.6 nm. The diode laser was locked to the TEM_{00} mode of the spherical cavity which is closest to the fiber laser frequency. The down-mixed beat signal was recorded for one second and the phase noise PSD was derived as described in the main text. The peaks from 10 Hz to 30 Hz result from vibrations affecting the cylindrical cavity. The spikes at 50 Hz and harmonic frequencies up to 500 Hz are not real since they were not observed on the optical beat note. The spikes emerge from electromagnetic pick up resulting from a ground loop with the oscilloscope. The broad-band phase noise at frequencies of about 5 kHz and higher is attributed to the diode laser. The increased high-frequency noise is the limiting factor for coherent operations on the intercombination transition in $^{27}\text{Al}^+$ (see section 5.5) but could not be compensated for.

At frequencies ranging from 1 Hz to 1 kHz the phase noise power spectral density decreases linearly (20 dB/decade). At frequencies of 5 kHz and higher two phase noise bumps can be obtained in the spectrum, which can be attributed to the diode laser (see section 5.5). As soon as the locks were optimized, the combined spectral width of both lasers was analyzed. Therefore the beat signal at 212 MHz was Fourier analyzed with a high resolution spectrum analyzer⁸⁵ with an acquisition time of 4 s and a resolution bandwidth of 1 Hz. The results are presented in figure 4.24. A lorentzian fit of the beat spectrum yields a spectral width of $\Delta\nu = 1.63(3)$ Hz FWHM. In the case of both lasers contributing equally to the signal each laser is assumed to have a linewidth of $\Delta\nu/2 = 0.82(2)$ Hz. Servo bumps and characteristic noise sources can be identified in the logarithmic plot.

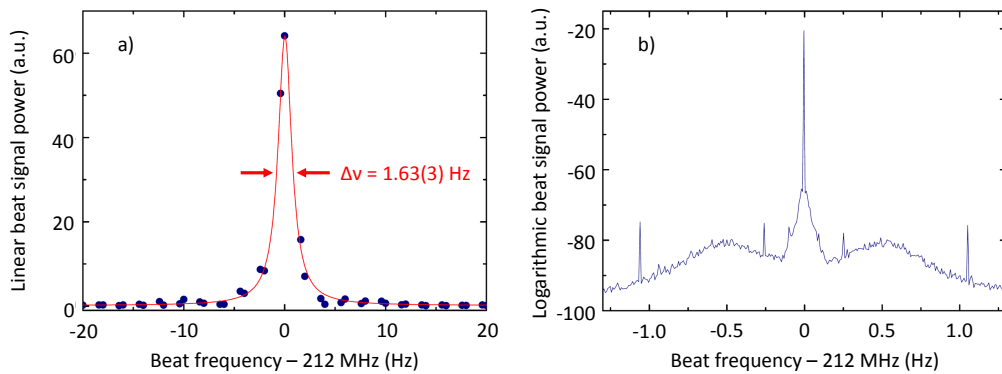


Figure 4.24: Optical beat note detection between both stable aluminium lasers at 1069.6 nm. The diode laser was locked to the TEM_{00} mode of the spherical cavity which is closest to the fiber laser frequency. The beat at 212 MHz was detected with a fast photodiode. a) linear power spectrum of the beat signal. The data consists of two consecutive sweeps (centered afterwards) at a resolution bandwidth of 1 Hz with an acquisition time of 4 s each. A lorentzian fit yields a spectral width of $\Delta\nu = 1.63(3)$ Hz FWHM. If both lasers contribute equally to the signal, a spectral width of $\Delta\nu/2 = 0.82(2)$ Hz each can be assumed. Note, that the data represents the two best shots out of five. The other data sets suffered from the long-term instability of the diode laser (see figure 4.25 and main text for more information) b) logarithmic power spectrum of the beat signal taken with a resolution bandwidth of 10 Hz. The small shoulders around 10 kHz correspond to noise of the diode laser. Servo bumps of the fiber laser lock are slightly visible at 100 kHz. The broad peaks around 500 kHz are servo bumps of the diode laser lock. The spikes at 250 kHz and 1.1 MHz are most likely due to electromagnetic pick up.

The frequency stability of the lasers over longer time scales is typically characterized by the Allan deviation. It denotes the fractional frequency uncertainty for different averaging times

⁸⁵Rohde & Schwarz FSP 13

and is expressed by

$$\sigma_y(\tau) = \sqrt{\frac{1}{2(m-1)} \sum_{i=1}^{m-1} (y_{i+1} - y_i)^2} \quad (4.1)$$

where y_i are the fractional frequencies averaged over a temporal period τ and m is the number of y_i values. An optical beat note detection between two lasers contains the instabilities of both lasers. The combined Allan variance of two oscillators is $\sigma_{A,B}^2(\tau) = \sigma_A^2(\tau) + \sigma_B^2(\tau)$. As soon as a third oscillator C comes into play the variances can be decomposed into the variances of each oscillator by the three-cornered hat method $\sigma_A^2(\tau) = \frac{1}{2}(\sigma_{A,B}^2(\tau) + \sigma_{C,A}^2(\tau) - \sigma_{C,B}^2(\tau))$. To extract the instability of each laser, both laser frequencies were simultaneously measured with the frequency comb (see section 4.2.4). The Allan deviations of both lasers and the frequency comb are presented in figure 4.25.

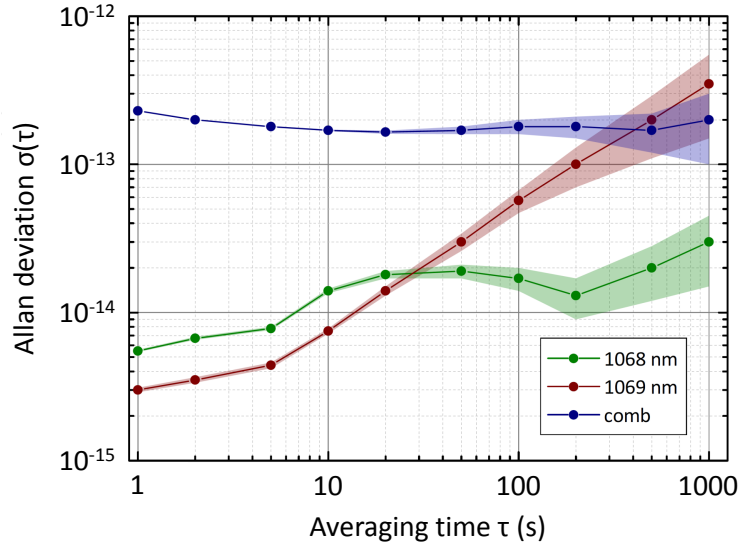


Figure 4.25: Allan deviations of the frequency comb (locked to the GPS disciplined OCXO) and both aluminium lasers at their fundamental wavelength. The laser frequencies were simultaneously measured with the frequency comb. The Allan deviations were calculated afterwards (see main text). The short-term stability of the 1069 nm laser of $3 \cdot 10^{-15}$ at 1 s is close to the thermal noise floor of the cylindrical reference cavity ($7.4 \cdot 10^{-16}$ at 1 s). The long-term behaviour is dominated by the cavity drift rate. The short-term stability of the 1068 nm laser of $5.5 \cdot 10^{-15}$ at 1 s is also close to the thermal noise floor of the spherical reference cavity ($1.7 \cdot 10^{-15}$ at 1 s). The drift rate is significantly smaller compared to the cylindrical cavity. On time scales from 10 s to 100 s the stability suffers from the cavity response to its temperature stabilization (see main text). Note that each optical path contained a 2 m long optical fiber whose optical path length was not stabilized. Therefore the short term stabilities of both lasers should be considered as upper bounds. The direct linewidth measurement in figure 4.24 indicates a combined instability of $5.8 \cdot 10^{-15}$ at 4 s. The instability of the comb (OCXO) is quite constantly $2 \cdot 10^{-13}$.

The inferred short term stabilities of both lasers are close to the thermal noise limit of the corresponding reference cavities. Each optical path contained a 2 m long fiber, whose optical pathlength was not actively stabilized. Therefore the short term stabilities should be seen as an upper bound. The long term behaviour is dominated by the aging of the cavities, resulting in frequency drifts. Linear drifts can be compensated for by sweeping the frequency of an AOM in the optical path. The stability of the 1068 nm laser on time scales between 10 s and 100 s suffers from the temperature stabilization of the spherical cavity. The digital temperature stabilization has a low pass filter of 10 s. Therefore the current, sent through the Peltier-element inside the cavity housing is changed on this time scale. Whenever the current is changed an instantaneous increase of the laser frequency of about 10 Hz is observed, which then relaxes during the next seconds, leading to a saw-tooth-like signal. The mechanism leading to the frequency excursions of the laser is not clear. A possible explanation could be that the cavity is held in place by a clamp which is mounted to a base-plate to which the Peltier-element is attached. When the Peltier cools ($T_C=5.514^\circ\text{C}$) the housing the base-plate contracts, resulting in an increased force on the cavity spacer.

The laser stabilization is done on a best effort basis. In view of the acoustic and electromagnetic noise at the location of the cavities as well as the spatial separation of lasers and cavities, the short term stability is quite remarkable since it is close to its theoretical limit. Further improvements of the laser stability would require major changes on the setup in terms of acoustic and electromagnetic shielding.

Fiber noise cancellation

Light that travels along an optical fiber acquires frequency noise due to changes of the optical path length caused by acoustic vibrations, thermally and air pressure induced stress [69]. These effects broaden the laser linewidth, depending on the fiber length and the noise that it is exposed to. For precision experiments that rely on a narrow laser line, this fiber noise is not tolerable and it has to be compensated for [69].

The optical setup for fiber noise cancellation (FNC) consists of a non-polarizing beam splitter with 30% reflection. The transmitted light passes an 80 MHz AOM and the $+1^{st}$ diffraction order is coupled into a fiber. Typically 4% of the light is reflected at the 0° angle-polished fiber end and acquires the noise twice while travelling backwards along the fiber. The light passes the AOM a second time and the $+1^{st}$ order is overlapped with the incident beam at the beam splitter in front of the AOM. A fiber noise modulated beat note at twice the AOM frequency can be detected with a fast photodiode. The beat signal is mixed down with a stable 160 MHz signal from a referenced RF synthesizer. The error signal represents the phase difference between the beat signal and the RF signal. It is sent to a PI controller whose

output is connected to a voltage-controlled oscillator (VCO). The VCO⁸⁶ provides the driving frequency for the AOM and therefore closes the control loop. The fiber noise is compensated by a phase locked loop (PLL).

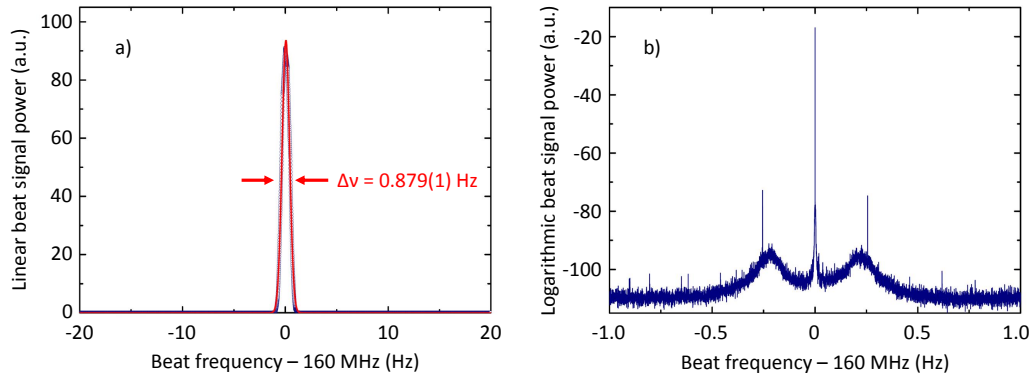


Figure 4.26: Optical beat note detection of a 10 m long noise-cancelled fiber. a) Linear power spectrum of the beat signal. The data is taken with a resolution bandwidth of 1 Hz. The spectral width of the peak is close to the resolution limit of the spectrum analyzer. For $1/f$ noise in the lab a Gaussian-like line shape is expected [70]. A Gaussian fit gives a spectral width of 0.879(1) Hz FWHM. b) Logarithmic power spectrum of the beat signal taken with a resolution bandwidth of 10 Hz. The peaks around 200 kHz correspond to servo bumps of the control loop.

Typically locking bandwidths of more than 100 kHz are achieved. A Fourier spectrum of the beat signal for a 10 m long noise cancelled fiber is presented in figure 4.26. The spectral width of the beat is 0.879(1) Hz FWHM, which is close to the resolution limit of the spectrum analyzer.

UV fiber noise

Like all optical fibers also the fused silica solid core photonic crystal fibers [64], which guide the 267 nm light to the trap, modulate noise onto the laser light. These fibers are more exposed to acoustic noise present in the lab since only the bare fiber without any cord is used. At this point in the beam path the noise cannot be cancelled in the usual way since it is not continuous wave (CW) any more. Therefore the spectral broadening of the light travelling through 1.5 m long fibers for typical noise conditions in the lab were investigated. The spectral broadening is measured by a self-heterodyne linewidth measurement with a fast photo diode. A constant frequency offset of 150 MHz was induced by an AOM. The spectrum of the beat was observed with a high resolution spectrum analyzer⁸⁷, which is presented in figure 4.27. The laser used in this experiment was a free-running frequency-quadrupled fiber

⁸⁶Micronetics MW500-1531

⁸⁷Rohde & Schwarz FSP 13

laser with a short term linewidth of ≤ 8 kHz. Since the beam paths of the interferometer are nearly equally long the observed spectral width of the beat results only from fiber noise. The presented spectrum consists of 100 acquisitions with a resolution bandwidth of 1 Hz. The total measurement time was about 5 min. A spectral width of 4.02(3) Hz FWHM was observed. Probably the spectral broadening of the light can be further suppressed by better acoustic shielding and vibration damping.

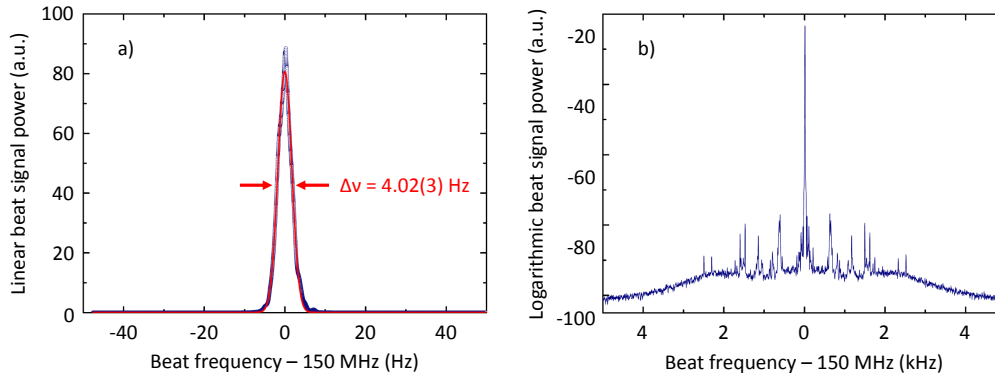


Figure 4.27: *Optical beat note detection of frequency noise induced by a 1.5 m long fiber. a) linear power spectrum of the beat signal. The data consists of an average of 100 consecutive measurements with a resolution bandwidth of 1 Hz with a total measurement time of ~ 5 min. The spectral width of the peak is not limited by the bandwidth of the spectrum analyzer. A Gaussian fit gives a spectral width of 4.02(3) Hz FWHM. b) logarithmic power spectrum of the beat signal taken with a resolution bandwidth of 10 Hz. The peaks between 600 Hz and 1.5 kHz correspond to acoustic noise and mechanical vibrations on the optical table.*

4.2.4 Frequency comb

One of the centerpieces of an optical frequency standard is the frequency comb, used for measuring frequencies in the optical domain. It acts as a clockwork and down-converts the frequency of a laser that is locked to an atomic transition to the radio-frequency (RF) domain. The RF frequencies can then be handled and distributed by commercial electronics. In the following, the setup and working principle of the femto-second fiber laser frequency comb⁸⁸ used in this work is described.

Operating principle

A fiber ring emits a train of ultra-short laser pulses which result from a coherent superposition of many equally spaced optical frequencies $f_n = n \cdot f_{rep}$. The temporal separation of the pulses is set by the round trip time within the fiber ring. The output of a frequency comb in the

⁸⁸Menlo Systems FC1500

time and frequency domain is depicted in figure 4.28. Hence the repetition rate is given by $f_{rep} = 1/\tau = c/l$, with l being the cavity length and the speed of light c . The laser is said to be mode-locked when there is a common phase relationship among all longitudinal modes f_n . This phase relationship defines the phase of the electric field compared to the pulse envelope and is called carrier-envelope phase ϕ_{CE} which is shifted by $\Delta\phi_{CE}$ after each cavity round trip.

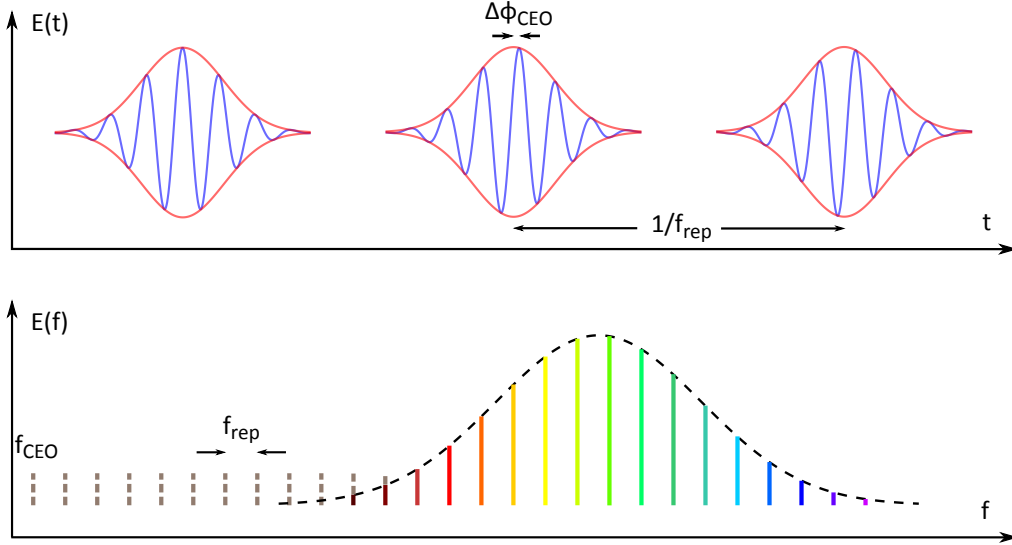


Figure 4.28: Top: Pulse train emitted by a mode locked laser. Bottom: Eponymous comb-like frequency spectrum.

Since the pulse envelope propagates with the group velocity v_g , while the carrier wave travels with its phase velocity v_p the entire spectrum of the frequency comb is shifted by the carrier-envelope-offset (CEO) frequency

$$f_{CEO} = \frac{1}{2\pi} \frac{d\phi_{CE}}{dt} \approx \frac{\Delta\phi_{CE}}{2\pi\tau} \quad (4.2)$$

The whole frequency spectrum can now be characterized with the repetition rate and the carrier-envelope-offset frequency. The mode spectrum is expressed by

$$f_m = m \cdot f_{rep} + f_{CEO} \quad (4.3)$$

with an integer number m on the order of $\sim 10^6$. Both frequencies are within the radio frequency domain. After determining m , the optical frequency is obtained from a measurement of f_{rep} and f_{CEO} .

Femtosecond fiber laser

The centerpiece of the comb is an Erbium doped fiber ring laser. The repetition rate is adjustable via an intra-cavity EOM and a mirror piezo by adjusting the optical path length of the laser resonator. Variable pump power and a moveable intra-cavity wedge provides control over the carrier envelope offset frequency. The pump light is coupled into the fiber ring via a wavelength division multiplexer (WDM). A Faraday isolator (FI) prevents the predominant direction for the light. Wave plates before and after the fiber provide control over the laser polarization. A schematic overview of the comb setup is presented in figure 4.29. Usually the repetition rate and the offset frequency are locked to the 10 MHz reference (GPS disciplined oven controlled quartz oscillator (OCXO)⁸⁹) with a fractional frequency instability of $\sim 2 \cdot 10^{-13}$.

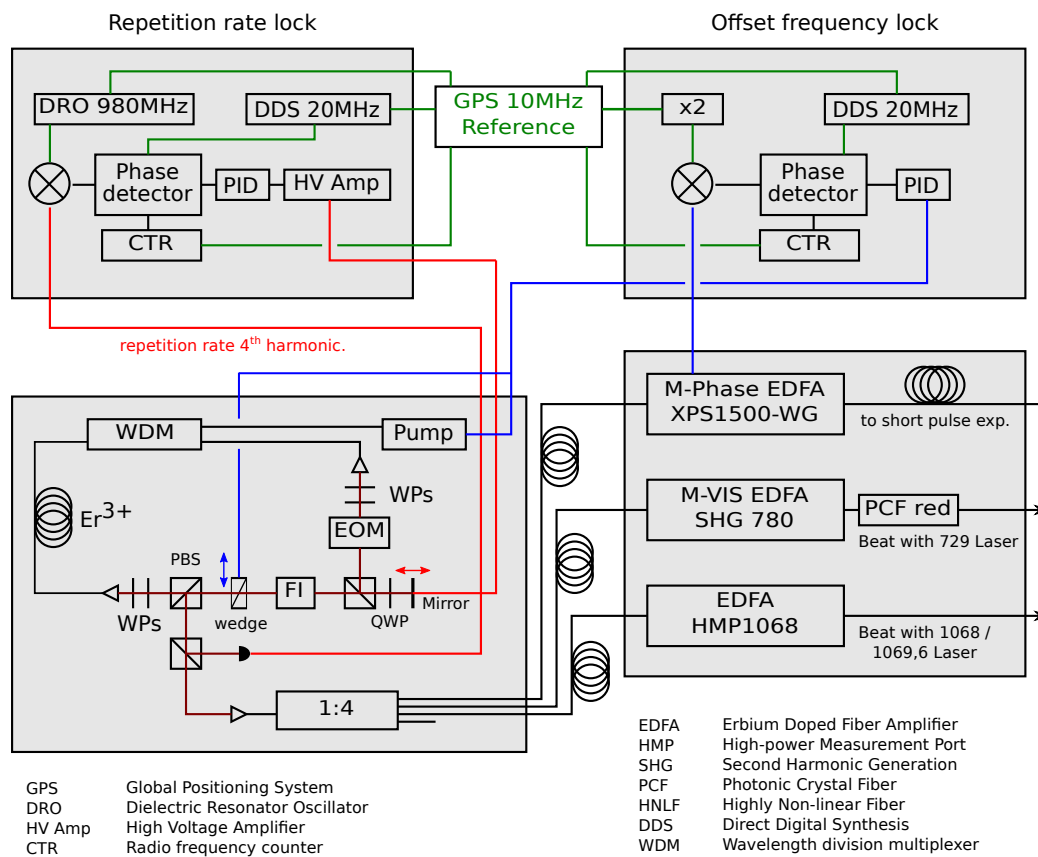


Figure 4.29: Schematic drawing of the frequency comb locked to the 10 MHz GPS signal (green lines). The centerpiece of the comb is the Erbium doped fiber ring at the bottom left. Red and blue lines represent the measured repetition rate and offset frequency, respectively as well as their control signals. The EOM in the fiber ring is only in use when the comb is locked to an optical reference. See main text for more information.

⁸⁹Menlo systems GPS 6-12

Within the M-VIS EDFA SHG 780 unit, the light from the fiber ring is amplified, frequency-doubled and sent to a highly non-linear fiber for spectral broadening. The outcome is used to measure the frequency of the 729 nm laser via an optical beat note (see below). The EDFA HMP1068 unit amplifies the comb light and creates a comb spectrum around 1068 nm which is used for the frequency measurement of both aluminium lasers at their fundamental wavelengths of 1068 nm and 1069.6 nm. The frequency shift of the comb spectrum is achieved by the soliton self-frequency Raman shift [71], which depends on the pump power. Typical comb spectra are presented in figure 4.30.

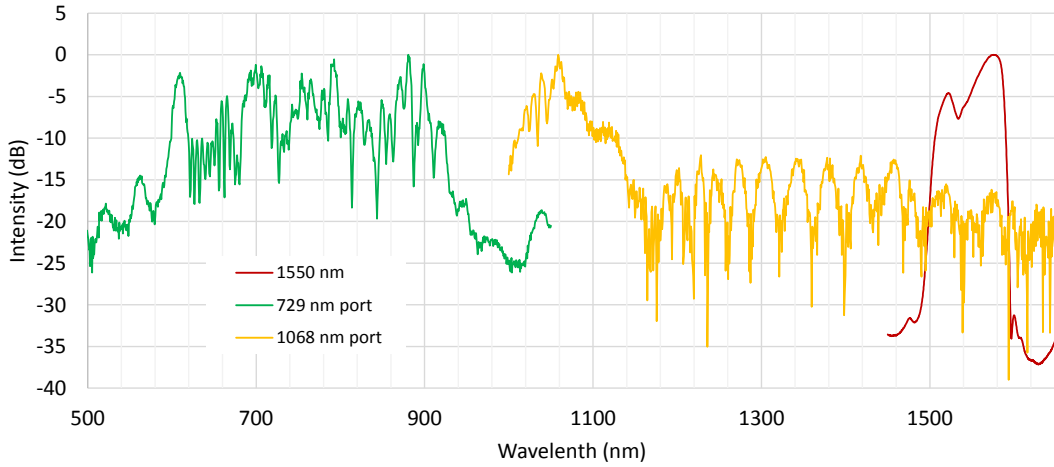


Figure 4.30: Frequency comb spectra at the fundamental wavelength around 1550 nm (red) and the two measurements ports around 729 nm (green) and 1068 nm (orange). The optical power at the two measurement ports are 132 mW and 79 mW, respectively. With kind permission from Menlo Systems.

Optical beat note detection

There are several ways to characterize a laser's spectral properties and its frequency. In the case of a second laser being the reference, this is done via an optical beat note detection. Therefore both lasers with similar frequencies are overlapped on a fast photodiode via a non-polarizing beam splitter (BS). The resulting photo-current is frequency-modulated by the difference frequency of the lasers and can be expressed as:

$$I(t) \sim |E_1(t) + E_2(t)|^2 = |E_1(t)|^2 + |E_2(t)|^2 + 2\text{Re}\{E_1^*(t) \cdot E_2(t)\} \quad (4.4)$$

The power spectrum observed on a spectrum analyzer is a convolution of both laser spectra:

$$S_{E_1^* \cdot E_2}(f) = S_{E_1}(f) \otimes S_{E_2}(f) \quad (4.5)$$

The contribution of each laser to the convoluted spectrum depends on their noise spectra. In the case of white noise the line shape of the lasers are lorentzian and the spectral width (full width at half maximum) of the convoluted signal is $\Delta_{beat} = \Delta f_1 + \Delta f_2$. Gaussian laser spectra lead to $\Delta_{beat} = \sqrt{\Delta f_1^2 + \Delta f_2^2}$.

Repetition rate lock

To stabilize the repetition rate (250 MHz in this case) to the GPS reference a small part of the comb light is sent to a fast photodiode where the fourth harmonic of the repetition rate is detected. This signal around 1 GHz is mixed down with a 980 MHz signal derived from a referenced dielectric resonator oscillator (DRO) and a signal around 20 MHz is generated. To create an error signal at DC it is once more mixed down with a 20 MHz signal derived from a referenced direct digital synthesizer (DDS). The error signal is fed into a PID controller, amplified afterwards and applied to the mirror piezo that controls the cavity length and therefore the repetition rate. The repetition rate can be also locked to a stable laser when the comb is used to down-convert a optical frequency to RF. Therefore the beat signal between the comb and the laser is kept fixed by feeding back onto the intra-cavity EOM and the piezo mirror.

Offset frequency lock

The CEO frequency is generated in the M-Phase EDFA XPS1500-WG unit. There the light at a center wavelength 1.56 μm is amplified and spectrally broadened by a highly non-linear fiber to more than an octave (1 μm - 2.1 μm). A non-linear interferometer, which doubles the frequency of the long-wavelength part of the spectrum and compares it with the near infrared part via a beat note. The beat frequency is the CEO frequency, which is usually set to 20 MHz.

$$|2(nf_{rep} + f_{CEO}) - (2nf_{rep} + f_{CEO})| = f_{CEO} \quad (4.6)$$

To lock the CEO frequency to 20 MHz it is mixed with a frequency doubled GPS signal. The resulting signal is put into a phase detector together with the target frequency derived from a referenced DDS. The error signal is sent to a PID controller and its output is connected to the pump current control.

Frequency measurement

The frequency of a continuous wave (CW) laser can be measured via an optical beat note with the light of the frequency comb. Therefore the two laser beams with the same polarization are spatially overlapped. To select only comb modes with a frequency similar to the CW laser the beams are sent onto a grating. The CW laser and the nearest comb modes are diffracted

under the same angle and sent to a fast photodiode. A beat note (typically ~ 40 kHz FWHM if limited by the comb stability) between the laser and the nearest comb modes is visible on a spectrum analyzer. The signal to noise ratio (SNR) of the beat signal has to be optimized by improving the spatial alignment and the spectral output of the comb. The latter is done via translation stages that vary the amount of comb light which is coupled into the nonlinear fibers by moving objectives. The output spectra depend on the pump power. Depending on the RF counters used in the measurement the beat signal has to be amplified and the signal-to-noise ratio should reach 30 dB or more at a resolution bandwidth of 50 kHz to guarantee for correct frequency counting. It is useful to use band pass filters to enhance the SNR. Ideally the beat signal is split and counted by two separate counters while one path is attenuated by 3 dB or more. For precision measurements on the Hz scale both counter values should fully agree within the resolution limit. If both counters disagree by more than ~ 10 mHz for beat frequencies in the 10 MHz range and a gate time of 1 s, the SNR is too low.

Before the absolute frequency measurement can start, the signs of the beat frequencies and the absolute mode number n have to be determined.

$$f_{CW} = n f_{rep} \pm f_{CEO} \pm f_{beat} \quad (4.7)$$

The sign of the beat frequency can be determined by changing the repetition rate slightly. If the sign is positive, the beat frequency decreases while the repetition rate increases and vice versa. The sign of the offset-beat can be determined in a similar way. The sign is positive when the beat frequency decreases with increasing offset frequency. In the case of the visible comb port, the offset frequency is added twice since the comb light was frequency-doubled. The mode number can be calculated by two frequency measurements with significantly different repetition rates. The repetition rates should differ by about 10 kHz or more, otherwise mistakes in the determination become more likely due to a lower signal-to-noise ratio. This is not necessary in this setup since the wavelength meter is accurate enough to identify the mode number.

The optical power density of the comb output spectra around 729 nm and 1068 nm is typically ~ 2 mW/nm which results in ~ 1.4 μ W per comb mode for optimized parameters. As soon as the measurement starts, the repetition rate, the offset frequency and the beat frequency are simultaneously recorded by dead-time free RF counters⁹⁰ and are added up to the optical frequency. Usually the repetition rate and the offset frequency are locked to the 10 MHz reference (GPS disciplined OCXO⁹¹) with a fractional frequency instability of $\sim 2 \cdot 10^{-13}$ at time scales of from seconds to hours (see figure 4.25). There is the possibility to lock the repetition rate directly to a stable laser (for example 729 nm laser) which should improve the stability of the comb. Unfortunately the translation stage, which is responsible for the 729 nm

⁹⁰FXM50 K&K Messtechnik

⁹¹Menlo systems GPS 6-12

spectrum, is mechanically not stable enough and therefore requires high maintainance to keep a sufficient SNR which makes it laborious to work with.

4.3 Experimental control

Several different hardware components are involved in the electronic control of the experiment. A schematic drawing of the experimental control is presented in figure 4.31. Its centerpiece is the Control PC on which a C++ program (TrICS = trapped ion control system) coordinates the tasks of multiple devices and provides a graphical user interface (GUI). It compiles the pulse sequences that are written in python for a given set of parameters in the TrICS GUI and sends it via a Ethernet connection to the “Pulse Box”. The latter is FPGA-based and contains 8 direct digital synthesizers (DDS) which allow for precise timing, frequency and phase control of the generated RF pulses that are sent to AOMs in the stable laser setup. All frequency sources that are crucial in terms of accuracy are referenced to the 10 MHz GPS signal.

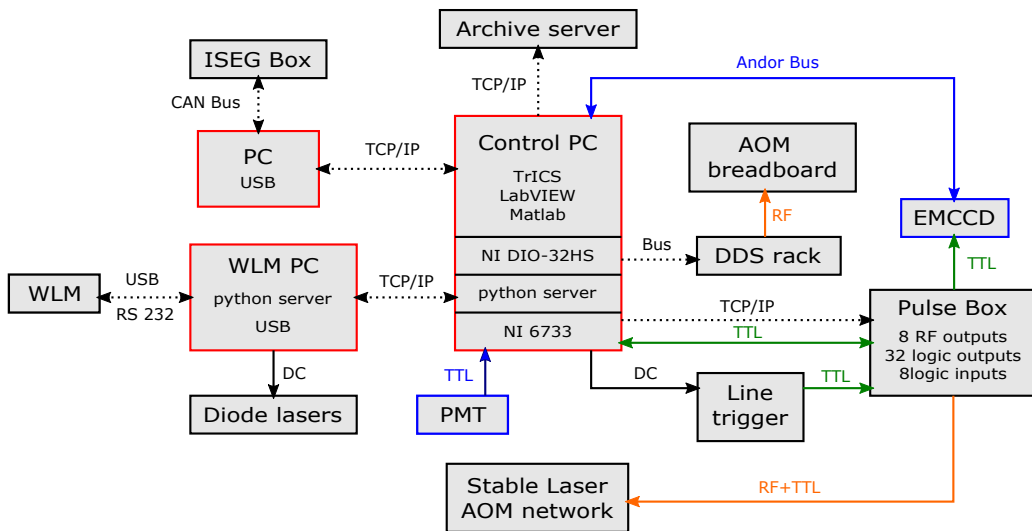


Figure 4.31: Schematic overview of the experimental control. Devices are represented as boxes and their links by arrows. All control signals emanate from the control PC in the center. It is connected to two auxiliary PCs that are responsible for the control of the high-voltage source (ISEG), which provides the voltage for the endcap electrodes and the wavelength meter (WLM) which is involved in the stabilization of the diode lasers. The Pulse box and the DDS rack provide the RF signals for the AOMs. The fluorescence data is acquired by a photomultiplier tube or by an electron multiplying charge coupled device camera.

All other AOMs on the breadboard are driven by homebuilt DDSs whose output power and frequency are controlled by TrICS via the bus system. The WLM PC on which the wavelength meter software is running is connected to the Control PC via Ethernet. It receives the setpoint frequencies of the diode lasers from TrICS. The high finesse wavelength control translates them into DC voltages which are applied to the piezos. A further PC is used to control the stable high voltage source (ISEG) and other devices. The state detection is done by recording the

fluorescence counts for a given time window after each experiment. For experiments with only one calcium ion the photomultiplier tube (PMT) was used. For experiments with long ion strings a LabVIEW based program [72] communicating with the EMCCD camera can be used. The experimental data is displayed on the TrICS GUI or automatically post-processed to feed back on the laser lock and the calculation of the magnetic field.

5 Experimental techniques

In this chapter important experimental techniques for experiments with trapped ions are presented. The first part presents an investigation of the laser ablation loading of $^{40}\text{Ca}^+$ and $^{27}\text{Al}^+$ ions, which was published in New Journal of Physics [73]. The second part describes the procedures of setting up a typical experimental sequence involving laser cooling, optical pumping as well as the calibration of sideband frequencies and AC-Stark shifts. The third and fourth parts present how a stable laser is referenced to a narrow atomic transition and detail the method of compensating micromotion using the narrow-band laser. In the last part, the method of quantum logic spectroscopy is introduced which is used to detect the electronic state of an aluminium ion.

5.1 Laser ablation loading of ions

The standard approach of loading ions into a trap is to evaporate neutral atoms of a particular element from a resistively heated oven and to photo-ionize them at the trap center. In the case of calcium ions this is a well-proven technique, which has been used for more than a decade. Evaporating neutral aluminium atoms from a thermal source requires considerably higher temperatures to create a sufficient atom flux. In the first trap setup an alumina ceramic oven with a piece of pure aluminium in the center was resistively heated by a tantalum wire. To trap an aluminium ion the oven was operated at 12 W for several minutes. The dissipated heat led to thermal expansion of the ion trap holder of tens of microns and outgassing problems. Another drawback was the short lifetime of the oven since the tantalum wire burnt through after a few attempts.

An alternative approach, which was used in the second setup, is to evaporate neutral atoms by single ablation laser pulses. For this purpose, single laser pulses at 532 nm with a duration of 2 ns and a pulse energy of 100 μJ were fired onto ablation targets. The trap potential was set such that a single calcium ion oscillated with frequencies of 400 kHz axially and 2 MHz radially. To load calcium ions the alloy target (see section 4.1) was used on which the ablation laser was focused to a Gaussian beam waist of 200 μm FWHM. Aluminium atoms were ablated from the pure aluminium target with a spot size of 50 μm FWHM. Initially the intention was to load both species from the alloy target. However, loading aluminium ions from the alloy target was only possible with a substantially higher pulse energy which directly

created unwanted calcium ions. Both targets are hit by the ablation pulse under an incident angle of 30° . Simultaneously the photo-ionization lasers were sent along the trap axis with Gaussian beam waists of $100\ \mu\text{m}$ FWHM and laser powers of $500\ \mu\text{W}$ each.

For experiments with a mixed ion crystal a calcium ion is loaded first, since aluminium ions can only be sympathetically cooled. Typically a single calcium ion is loaded after a few ablation pulses. The probability of creating a single aluminium ion with one ablation pulse is similar. At the first attempts to load aluminium ions, relatively long cooling times on the order of several minutes were observed until the ions crystallize. In order to understand these long sympathetic cooling times, time-resolved neutral atom fluorescence measurements were carried out to characterize the velocity distribution of ablated atoms.

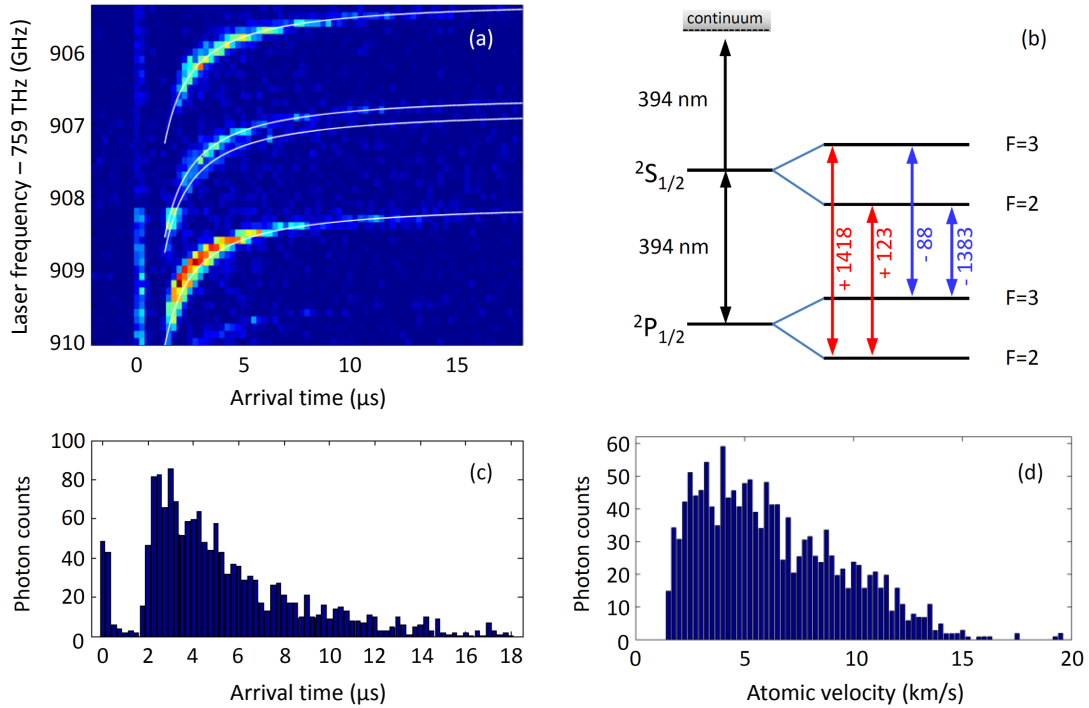


Figure 5.1: Time-resolved fluorescence spectroscopy on the $2P_{1/2} \leftrightarrow 2S_{1/2}$ transition. *a)* Time-resolved fluorescence of Al atoms crossing the trap center versus laser detuning. The number of detected photons is colour-coded in the image. The vertical line at $\tau \approx 0$ results from photons produced by the ablation pulse. The white lines indicate expected resonances between the motion of the atoms and the laser beam of 87.7° . *b)* Hyperfine structure of the transition with hyperfine shifts [62] in units of MHz. *c)* Histogram of atomic arrival times. *d)* Histogram of atomic velocities (see main text). The distribution peaks at velocities around $4.5\ \text{km/s}$.

Towards this end, single ablation pulses with an energy of $200\ \mu\text{J}$ were fired onto the targets while the photo-ionization laser was turned on. The atoms crossing the $394\ \text{nm}$ laser beam

scatter photons (see figure 5.1 b) which were detected by the PMT and recorded by a fast oscilloscope¹. Since atomic motion and laser beams were not perfectly perpendicular to each other a Doppler shift was observed. Each horizontal trace is the average of five laser ablation pulses. A fraction of the ablation pulse light was sent to a fast photodiode which provided the trigger signal for the oscilloscope. Because of the hyperfine structure of the ground and excited state four individual transitions are observed which are spread over about 3 GHz in frequency. To get rid of Doppler shifts the detected photon counts were summed up in frequency space which yields the arrival time distribution of the atoms on which a background was subtracted. To derive the atomic velocity distribution assumptions have to be made. The probability of detecting a scattered photon is inversely proportional to the atomic velocity. In the case of aluminium it is assumed that each atom only scatters one photon before it gets pumped to a different state. The fluorescence data and the inferred distributions are shown in figure 5.1. Finally, atomic velocities ranging from 1.5 up to 15 km/s are observed. The distribution peaks at atomic velocities of 4.5 km/s.

In order to detect the presence of an Al⁺ ion before the Ca⁺ and the Al⁺ ions crystallize into a 2-ion crystal, a new detection method was developed. A hot ion orbiting in the trap creates time-varying electric fields that act as a source of motional heating for the cold Ca⁺ ion. Small heating effects are easily detectable with Rabi spectroscopy on a motional sideband transition. In this case the heating effect is big enough that it is detectable on the carrier transition since their coupling strength depends on the motional state outside the Lamb-Dicke regime. The experimental sequence is the following:

- Doppler-cooling the calcium ion to the Lamb-Dicke regime and optical pumping to the S_{1/2} ground state.
- During a waiting time τ , the ion is heated if an aluminium ion is present in the trap.
- A π - pulse carried out on the S_{1/2} \leftrightarrow D_{5/2} transition. In the presence of an aluminium ion a reduced transfer probability is observed.
- State detection via electron shelving.

Figure 5.2 illustrates this detection technique. The recorded reduced transfer probability can be used to calculate the mean number of transferred motional quanta during the waiting time τ . By integration over time the initial energy of the hot ion can be calculated. More information about the sympathetic cooling dynamics can be found in section 6.1.

The velocity distribution of ablated calcium atoms can be also derived from neutral atom fluorescence. Since the ¹S₀ \leftrightarrow ¹P₁ transition in calcium is closed, contrary to the ²P_{1/2} \leftrightarrow ²S_{1/2} transition in aluminium, a calcium atom can scatter more than one photon while crossing the

¹LeCroy SDA 11000

laser beam. Corresponding data as well as the inferred arrival time and velocity distributions are presented in figure 5.3.

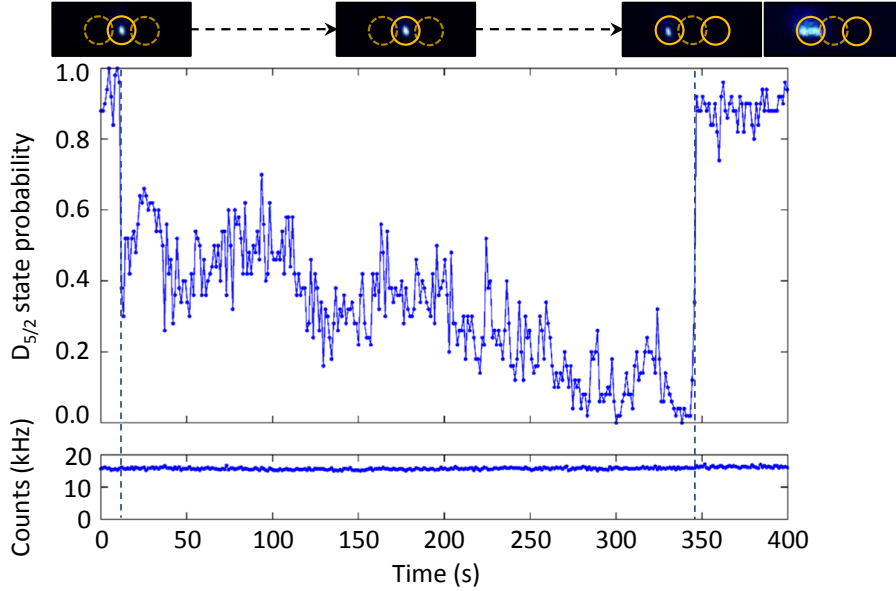


Figure 5.2: *Detecting the loading of a hot aluminium ion by a cold calcium ion. A π - pulse on the $S_{1/2} \leftrightarrow D_{5/2}$ transition transfers the population to the excited state of the calcium ion. After 10 s an ablation pulse is triggered and a hot $^{27}\text{Al}^+$ ion gets captured in the trap. It transfers kinetic energy to the present calcium ion which results in a reduced state transfer probability towards the excited state. Over the next 340 s the aluminium ion is sympathetically cooled until the ions crystallize. The presence of the hot ion does not show up in the fluorescence counts. The EMCCD camera images above show the equilibrium position of a single calcium ion and the two-ion crystal later on. The rightmost picture shows motional excitation of the mixed crystal by modulation of the axial confinement at the in-phase mode frequency for a measurement of the mass of the dark ion.*

Atomic velocities between 600 m/s and 4.2 km/s are observed. The main fraction of the ablated calcium atoms have velocities around 1.6 km/s which is almost a factor of 3 slower compared to ablated aluminium atoms.

A way to reduce the sympathetic cooling times of hot aluminium ions is to select relatively slow atoms by introducing a temporal delay τ_d between ablation pulse and the time when the photo-ionization laser is turned on for a duration τ . This also allows one to investigate which velocity classes of aluminium ions can be trapped. It turns out that only ions with velocities between 800 m/s and 3700 m/s can be trapped. The lower limit is given by the low density of slow atoms while the upper limit is set by the trap depth.

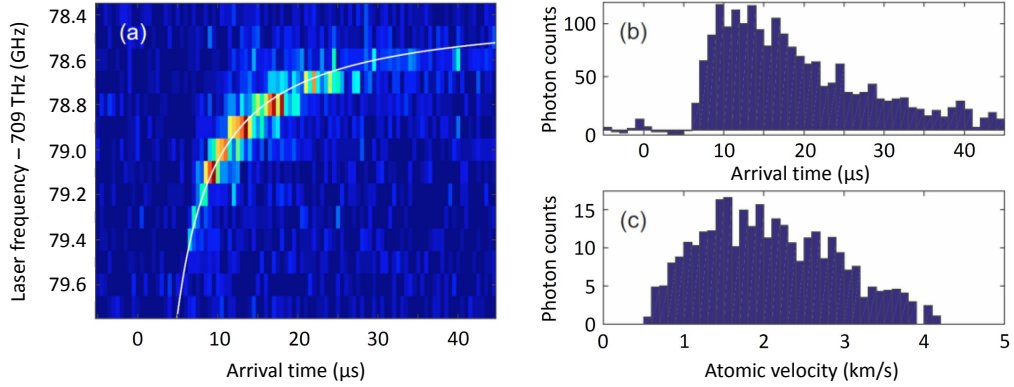


Figure 5.3: (a) Time-resolved fluorescence spectroscopy on the $^1S_0 \leftrightarrow ^1P_1$ transition of ^{40}Ca atoms crossing the trap center. The white line indicates the expected resonance for an angle of 84° between the direction of motion of the atoms and the laser beam. (b) Arrival time distribution obtained from (a) after background subtraction. (c) Atomic velocity distribution derived from (b) assuming that the number of scattered photons is inversely proportional to the atomic velocity v . The velocity distribution peaks at velocities of about 1600 m/s.

5.2 Experimental sequence

Every single experiment with trapped ions consists of a series of different steps. A schematic overview of a typical sequence is depicted in figure 5.4. Before the desired experiment can be carried out, the ions are prepared in a well-defined internal and motional state by laser cooling and optical pumping. After that coherent operations on the narrow transitions can be carried out with high fidelity. At the end of each experiment a quantum state measurement is performed. In the following each experimental step for experiments with an Al^{+} / Ca^{+} - mixed ion crystal is described. Thereby the focus is laid on the part describing the aluminium ion. The experimental sequences containing all relevant experimental parameters are encoded in a python file that is interpreted by the experiment control program. A detailed description can be found in [29].

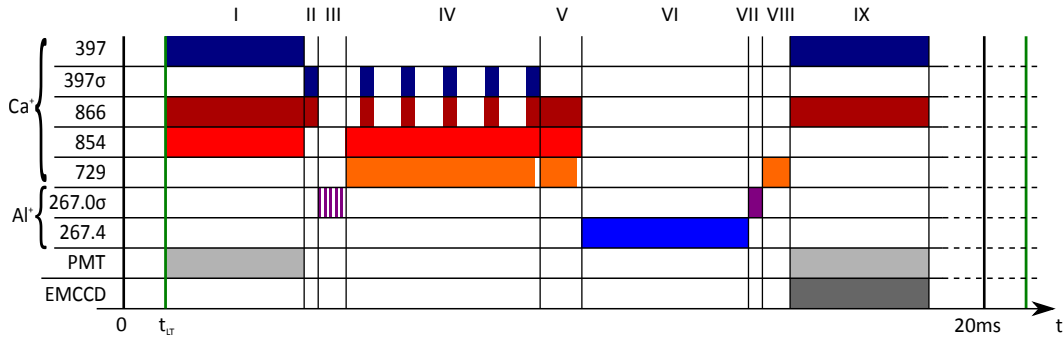


Figure 5.4: Schematic of a typical pulse sequence with a mixed ion crystal. Doppler-cooling (I) followed by optical pumping of Ca^{+} (II). Optical pumping on the aluminium ion (III). Continuous sideband cooling (IV). Frequency-resolved optical pumping (V). The particular experiment (VI). Quantum logic state transfer (VII) & (VIII). State detection (IX).

(I) Doppler-cooling

Every experimental sequence starts with Doppler-cooling the ions. A 397 nm beam addressing the $S_{1/2} \leftrightarrow P_{1/2}$ transition is applied for a period of 5 ms. The beam has overlap with all three normal modes of an ion in the trap. Since the transition is not closed, the 866 nm laser is used simultaneously for repumping population from the $D_{3/2}$ states. The intensity of the cooling laser is chosen to be half the saturation intensity of the transition and the laser frequency is red-detuned by half the spectral width of the transition $\Delta = -\gamma/2$. To avoid additional line broadening from the 866 nm laser its power is set close to saturation. Slightly blue-detuning the frequency of the 866 nm laser prevents coherent state trapping. The settings for sympathetic Doppler-cooling when working with mixed ion crystals are identical to the ones

chosen for cooling a single Ca^+ ion. The fluorescence counts registered during Doppler-cooling can be used to monitor the crystalline order of the ions. In the case of a melting event due to a collision with background gas an additional 160 MHz red-detuned beam is used to recrystallize the ions and the corrupted data is taken again.

(II) Optical pumping of $^{40}\text{Ca}^+$

After Doppler-cooling the calcium ion is prepared in the $m_j = +1/2$ ground state using the weak circularly polarized beam at 397 nm for about 20 μs . The achieved pumping fidelity is typically 99%.

(III) Frequency-resolved optical pumping of $^{27}\text{Al}^+$

If an aluminium ion is involved in the experiment a series of π - pulses on the $^1\text{S}_0 \leftrightarrow ^3\text{P}_1$ transition manifold is applied with $\Delta m = \pm 1$, depending on the desired target state. Each π - pulse is followed by a 300 μs waiting time to allow the excited state to decay.

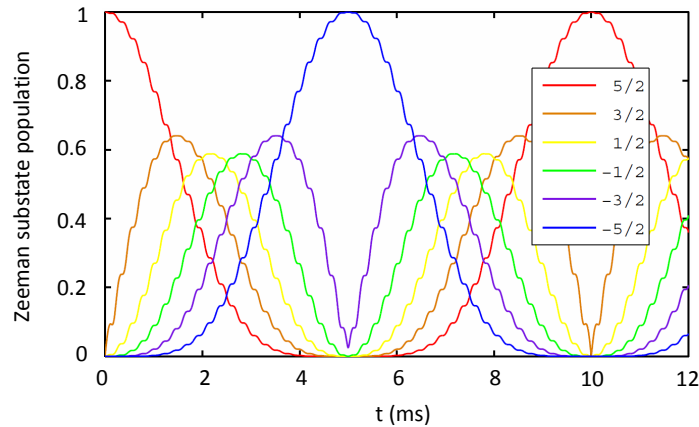


Figure 5.5: *Calculated time evolution of the resonantly driven six-level system starting in the $m_f = 5/2$ Zeeman substate. The calculation assumes a level splitting of 4.4 kHz and a Rabi frequency of 200 Hz. The small modulation from the fast rotating term indicates that a rotating-wave approximation would still be justified. Since the inner levels couple in both directions, only the stretched Zeeman states are fully populated at a certain point in time.*

A frequency measurement of the outermost transitions and precise knowledge of the magnetic field, calibrated with the $\text{S}_{1/2} \leftrightarrow \text{D}_{5/2}$ transition in calcium, allows one to calculate the frequencies of the inner transitions. Since the Rabi frequency on the outermost transition is known, the length of the π - pulses on the inner transitions can be calculated by the inverse ratio of the corresponding Clebsch-Gordan coefficients. The whole procedure is repeated five times.

The pumping efficiency is characterized by inducing nuclear spin flips by an AC magnetic field. With this the ion can be prepared in the other stretched Zeeman substate. The time evolution of the Zeeman substate populations for a given coupling strength is presented in figure 5.5. Frequency-resolved optical pumping as described above is carried out afterwards followed by a detection whether the ion has reached its target Zeeman state or not. The corresponding data is presented in figure 5.6.

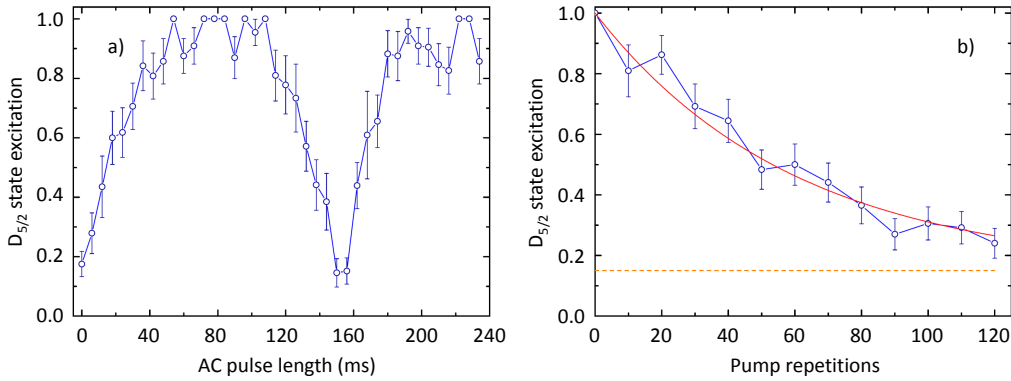


Figure 5.6: a) Nuclear spin rotation induced by an AC magnetic field at 4.452 kHz, detected via quantum logic spectroscopy with a calcium ion. At the beginning of the experiment the ion is prepared in the $m_F = 5/2$ Zeeman state via 100 pump repetitions. An AC magnetic field ($\sim 15 \text{ mG}_{\text{peak}}$) induces a full spin rotation within 150 ms. Since the initialization is not perfect, the data was postselected depending on the outcome of the previous experiment. The contrast is limited by imperfect state detection, the Rabi frequency is limited by the inductance of the coil pair ($\sim 6.5 \text{ mH}$) and the current driver, respectively as well as the magnetic field attenuation by the vacuum chamber ($\sim 15 \text{ dB}$). b) Pump efficiency characterization. The ion is transferred to the opposite stretched state $m_F = -5/2$ via a 75 ms long AC pulse and optical pumping towards the $m_F = 5/2$ state is carried out subsequently. The baseline at 0.15 arises from imperfect state detection. The red line is an exponential fit to the data. After about 40 repetitions half of the population is brought back to the target state. The probability of transferring the population from one stretched state to the other one is about 2% per pump repetition.

After about 40 pump repetitions half the population is brought from one stretched Zeeman state to the target Zeeman state. Therefore the probability of transferring the population from one outermost Zeeman state to the other using a single pumping step is about 2%. One limiting factor for the pump efficiency are imperfect π -pulses due to laser noise. Another reason could be a quadratic Zeeman shift of the inner 3P_1 Zeeman substates, resulting from a coupling to other 3P_1 hyperfine states, which would lead to off-resonant pump pulses, but needs further investigation.

(IV) Sideband cooling

For experiments that require the ions to be prepared in the ground state of a particular motional mode, continuous sideband-cooling is applied to the motional mode of interest for a duration of 7 ms. The 729 nm laser frequency is addressed to the red sideband of the corresponding mode of the $S_{1/2}, m_j = 1/2 \leftrightarrow D_{5/2}, m_j = 5/2$ transition. To speed up the process the 854 nm laser is used to reduce the lifetime of the excited state (quenching). Each of these cycles reduces the mean phonon number of the thermal state after Doppler-cooling by one. Since there is also a finite probability to decay from the $P_{3/2}$ into the $D_{3/2}$ state the 866 nm laser is used for repumping via the $P_{1/2}$ state. Additional optical pumping with the 397 nm laser ensures a closed cooling cycle.

(V) Frequency-resolved optical pumping of $^{40}\text{Ca}^+$

The optical pumping efficiency can be improved by using the 729 nm laser. Its frequency is made resonant with the $S_{1/2}, m_j = -1/2 \leftrightarrow D_{5/2}, m_j = 3/2$ transition. Together with the 854 nm and 866 nm laser this leads to a population transfer to the desired $S_{1/2}, m_j = 1/2$ state. Pumping efficiencies after 200 μs of 99.9 % can be achieved.

(VI) Coherent state manipulation

Now the ions are prepared in a particular electronic and motional state and the actual experiment can start. During the experiment the ion's internal and external states are manipulated using different accessible carrier and sideband transitions. While the carrier transition frequencies of $^{40}\text{Ca}^+$ are calibrated with the clock script (see section 5.3), sideband transition frequencies are calibrated manually. Symmetrically to carrier transitions motional sidebands appear. The sidebands can be identified by their response to changes of the trap potential. A fraction of a typical excitation spectrum is presented in figure 5.7. The confinement and the quantization magnetic field have to be chosen in a way that sideband and carrier transitions are well separated in frequency. The linear Zeeman shift of transition frequencies depending on the quantization magnetic field is depicted in figure 5.8. Here only the electric quadrupole transition in $^{40}\text{Ca}^+$ and the intercombination line in $^{27}\text{Al}^+$ are considered.

At typical quantization magnetic fields of about 4 G and secular frequencies on the order of 1 MHz the linear Zeeman effect on the aluminium clock transition is too small to cause any overlap of sideband and carrier transitions.

Once the trapping confinement is chosen, excess micromotion has to be compensated (see section 5.5). As soon as micromotion is compensated for, Rabi frequencies on the transitions of interest as well as AC-Stark shifts of those have to be calibrated manually.

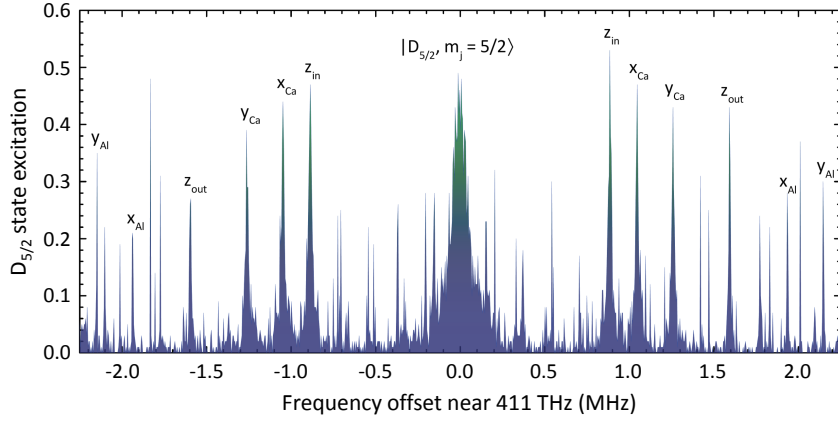


Figure 5.7: Fraction of an excitation spectrum of on the calcium $S_{1/2} \leftrightarrow D_{5/2}$ transition with a mixed Al-/Ca- ion crystal at typical trapping conditions, taken with the diagonal 729 nm beam. The center peak represents the $S_{1/2}, m_j = 1/2 \leftrightarrow D_{5/2}, m_j = 5/2$ carrier transition and symmetric to it red and blue motional sidebands of the mixed crystal appear. The axial in- and out-of-phase modes are visible at ± 888 kHz and ± 1.596 MHz respectively. The radial modes are not degenerate. Calcium-like modes are observed at ± 0.9 MHz and ± 1.1 MHz, the aluminium-like modes show up at ± 1.9 MHz and ± 2.1 MHz. Other peaks appearing correspond to second order sidebands or combination of those.

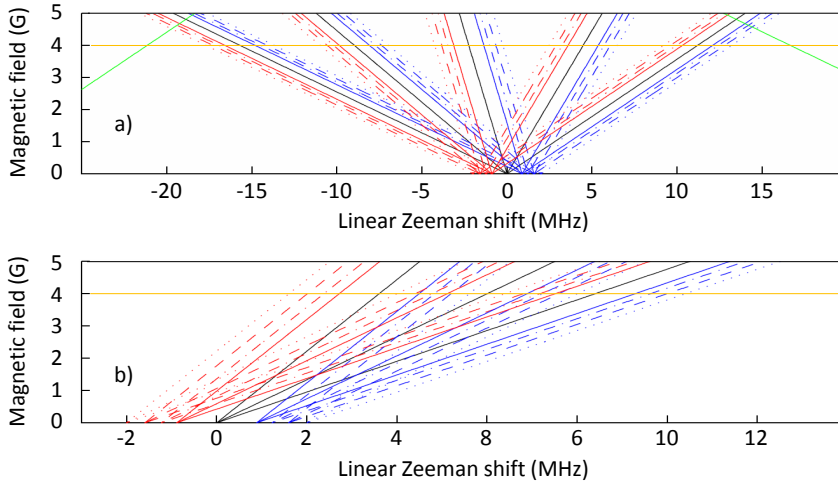


Figure 5.8: Calculated Zeeman-splitting of the $S_{1/2}, m_j = 1/2 \leftrightarrow D_{5/2}$ transition manifold in $^{40}\text{Ca}^+$ (top) and the $^1S_0, F = 5/2, m_f = 5/2 \leftrightarrow ^3P_1, F = 7/2, m_f = 3/2, 5/2, 7/2$ transition manifold in $^{27}\text{Al}^+$ (bottom) including red and blue motional sidebands. Carrier transition frequencies are depicted as black lines. The green lines are micromotion sidebands. For the case of $^1S_0, F = 5/2, m_f = -5/2 \leftrightarrow ^3P_1, F = 7/2, m_f = -3/2, -5/2, -7/2$ flip the sign on the x-axis. The Zeeman splitting of the ground state is negligible. For most of the experiments a quantization field of 4 G was applied.

(VII) & (VIII) Quantum logic state mapping

In the case of experiments with a mixed-ion crystal, the internal state of the aluminium ion has to be mapped to the internal state of the calcium ion before the fluorescence detection on the calcium ions happens. This is done in the quantum logic way by transferring the aluminium ion's internal state onto the motional state of a common motional mode and subsequently to the internal state of the calcium ion by the means of sideband pulses (see section 5.4).

(IX) Fluorescence detection

To discriminate between the $S_{1/2}$ and $D_{5/2}$ state of the calcium ions the 397 nm beam is turned on. In the case of the calcium ion being in the $S_{1/2}$ state photons are scattered on the $S_{1/2} \leftrightarrow P_{1/2}$ transition. The fluorescence photons are collected by a PMT or an EMCCD camera. To reach a high fluorescence rate the intensity of the 397 nm laser is set to the saturation intensity of the transition (on resonance). The laser frequency is still red-detuned by $\Delta = -\gamma/2$ from resonance. Detection efficiencies are well above 99% when collecting fluorescence photons for about 5 ms.

5.3 Locking the 729 nm Laser to the S-D transition

In order to carry out coherent operations with high fidelity precise knowledge of the laser frequency and the magnetic field is required. Therefore two symmetric transitions ($\pm 1/2 \leftrightarrow \pm 3/2$) with respect to the line center that suffer least from the quadrupole shift are probed by a Ramsey experiment. The duration of the $\pi/2$ - pulses is set to 100 μs to avoid significant AC Stark shifts. Each transition is probed twice with the phase of the second pulse shifted with respect to the first one by $(\phi_1 = \frac{\pi}{2}, \phi_2 = \frac{3\pi}{2})$. The pulses are separated by a waiting time τ_R . Taking the average over a hundred experiments each provides an estimate of the excited state probabilities p_{ϕ_1} and p_{ϕ_2} . The difference between the laser frequency and the atomic transition frequency is expressed by

$$\Delta\nu = \frac{1}{2\pi(\tau_R + 2\tau_\pi/\pi)} \arcsin \frac{p_{\phi_1} - p_{\phi_2}}{p_{\phi_1} + p_{\phi_2}}. \quad (5.1)$$

The line center at zero magnetic field can be calculated from the two measured frequency differences $\Delta\nu_1$ and $\Delta\nu_2$. The line center is the arithmetic mean of both frequencies since symmetric transitions were chosen. The magnetic field can be derived from the frequency difference of both transitions resulting from the linear Zeeman effect. The measurements are automatically executed every few minutes by the experiment control program which raises or lowers the waiting time between 10 μs and 4 ms depending on the outcome of the previous measurement. The laser frequency and the magnetic field are fitted by a polynomial of a chosen order (typically 1 for the frequency and 0 for the magnetic field) and the extrapolated values are used in the next experiment. It is useful to weigh the data contributing to the fit by the time when they were taken, which is implemented by an exponential loss of memory at a timescale of 10 min. Error bars are calculated from quantum projection noise [60] $\sigma = \sqrt{p(1-p)/N}$ where N is the number of measurements and p is the excitation probability.

5.4 Micromotion compensation

Electric stray fields that shift the ion from the RF nodal point cause excess micromotion, i.e. a driven motion at the trap's driving frequency Ω_T . Analogous to the case of secular motion the laser seems frequency modulated in the ion's reference frame due to resulting Doppler shifts. Consequently, the effective electric field can be expressed as [74]

$$E(t) = E_0 e^{-i\omega_l t} e^{ikx_a \frac{q}{2}} \sin(\Omega_T t) \quad (5.2)$$

where ω_l is the laser frequency, k is the wavevector of the laser beam, x_a is the ion's distance from the nodal point and the q-parameter q (see section 2.1). The second exponen-

tial in equation 5.2 can be expanded in terms of Bessel functions $J_n(\beta)$ as $e^{ikx_a \frac{q}{2} \sin(\Omega_T t)} = \sum_{n=-\infty}^{\infty} J_n(\beta) e^{in\Omega_T t}$ with the modulation index $\beta = kx_a \frac{q}{2}$. In the limit of small modulation, the modulation index β can be expressed in terms of the coupling strength ratios between carrier and micromotion sideband as $\beta/2 \approx \frac{J_1(\beta)}{J_2(\beta)} = \frac{\Omega_{MMSB}}{\Omega_{Carrier}}$.

The distance of the ion from the RF nodal point can be determined by $d = \frac{2\beta}{qk}$. The strength of a static electric stray field that shifts the ion's equilibrium position by d can be calculated by $E_s = \frac{m\omega_r^2 d}{e}$ where ω_r is the secular frequency. Excess micromotion first of all causes a loss in coupling strength on the carrier transitions and can prevent the ion from being efficiently cooled. Furthermore, it induces a systematic frequency shift in frequency standards and therefore has to be minimized by micromotion compensation techniques. The compensation is done by changing the DC voltages on the compensation electrodes and comparing the Rabi frequencies on carrier and micromotion sideband transitions. The relative coupling strength of the first micromotion sideband depending on the compensation voltage is presented in figure 5.9.

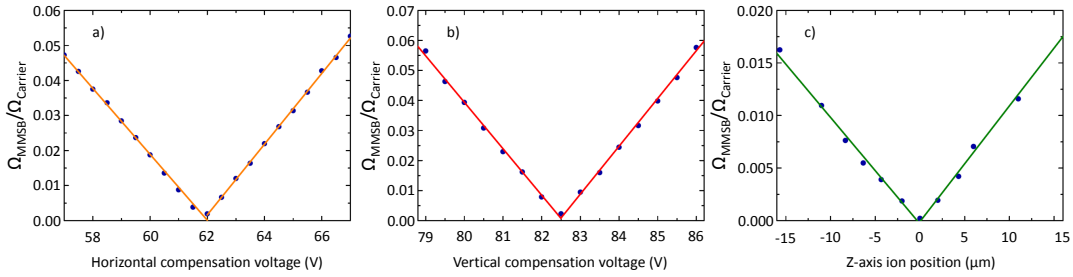


Figure 5.9: *Micromotion compensation in vertical a), horizontal b) and axial direction c). The data shows the coupling strength ratios of the first micromotion sideband to the carrier depending on the horizontal a) and vertical b) compensation voltages as well as the position along the trap axis c). The data was taken at an axial and radial confinement of 820 kHz and 1.35 MHz, respectively for a single $^{40}\text{Ca}^+$ ion. Minimal modulation indices of $\beta \approx 1/250$ are measured along the radial directions. Along the axial direction a minimal modulation index of $\beta \approx 1/2000$ is observed.*

For the current trap, typical compensation voltages are on the order of 60 - 80 V which lead to electric fields of 150 - 200 V/m at the position of the ion. In standard linear Paul traps (with endcap electrodes), driven by quarter wave resonators, also axial micromotion is present. To compensate for this, the endcap voltages are imbalanced such that the ion is placed to the RF nodal point. Optimized coupling strength ratios for all three directions of micromotion of $\frac{\Omega_{car}}{\Omega_{mm}} \gtrsim 500$ are achieved. The uncompensated stray field in radial direction is therefore 120 mV/m.

The homogeneity of radial micromotion along the trap axis was investigated by shifting the ion by 20 μm along the axis and optimizing the radial compensation voltages. Only a slight change of 0.5 V of the compensation voltage was necessary to reach optimal parameters again.

Some field lines from the RF blade electrodes point to the endcap electrodes which causes a shallow confinement along the axis. By comparing the q parameters in axial and radial direction using the relations $q = \frac{2\beta}{dk}$ and $q = \frac{\sqrt{8}\omega_r}{\Omega_T}$ respectively, the ratio of the quadrupole potentials can be calculated. This result shows that the trap creates nearly an ideal 2D quadrupole potential with 99.6% of the RF potential curvature in the radial plane.

5.5 Quantum logic spectroscopy

Quantum logic spectroscopy [75] is a technique that provides the ability to carry out experiments with ions that lack suitable transitions for cooling and state detection. With the help of a co-trapped “logic ion” ($^{40}\text{Ca}^+$) the “spectroscopy ion” ($^{27}\text{Al}^+$) can be sympathetically laser-cooled. Furthermore the internal state of the spectroscopy ion can be transferred to the internal state of the logic ion by coherent operations. The method uses coherent sideband pulses that map an internal state to a motional state of a common motional mode and vice versa.

At the beginning of the experiment both ions are prepared in the electronic and motional ground state of a joint motional mode $|0, g_S, g_L\rangle$. Spectroscopy on the clock transition of the spectroscopy ion creates a coherent superposition of the two clock states $|0, g_L\rangle \otimes \{\alpha |g_S\rangle + \beta |e_{S(3P_0)}\rangle\}$. A π - pulse on the blue sideband of the intercombination transition maps the ground state population to a phonon of a joint motional mode $\{\beta |0\rangle + \alpha |1\rangle\} \otimes \{\beta |e_{S(3P_0)}\rangle + \alpha |e_{S(3P_1)}\rangle\} \otimes |g_L\rangle$. A π - pulse on the red sideband of the clock transition of the logic ion maps the motional state to the logic ions internal state $|0\rangle \otimes \{\beta |e_{S(3P_0)}\rangle + \alpha |e_{S(3P_1)}\rangle\} \otimes \{\alpha |g_L\rangle + \beta |e_L\rangle\}$. The electronic state of the logic ion $\alpha |g_L\rangle + \beta |e_L\rangle$ is detected via electron shelving. The sequence described above is illustrated in figure 5.10.

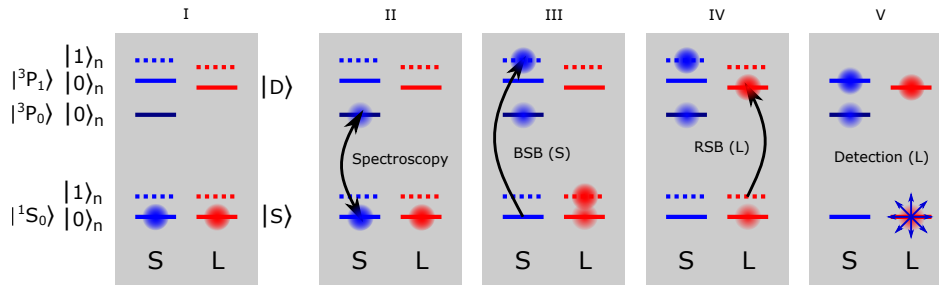


Figure 5.10: Quantum logic spectroscopy with an $\text{Al}^+ - \text{Ca}^+$ ion crystal. (I) The experiment starts with both ions in the electronic and motional ground state of a joint motional mode. (II) Spectroscopy on the clock transition of the spectroscopy ion. (III) Mapping of the ground state population to a phonon of a joint motional mode. (IV) Mapping the motional state to the logic ions internal state. (V) State detection via electron shelving.

During the measurements carried out in this work the out-of-phase axial mode at 1.596 MHz was chosen for the state transfer since it is further away in frequency from the carrier and has a much lower heating rate of only ~ 0.8 phonons/s compared to the axial in-phase mode with ~ 70 phonons/s .

The limit for the overall detection fidelity is given by the sum of different imperfect operations like state preparation, ground state cooling and the fidelity of the mapping pulses. The

biggest contribution comes from the imperfect blue sideband pulse on the intercombination transition. The highest transfer probability for this π - pulse was $\sim 95\%$, mainly limited by high frequency noise of the laser (see figure 4.23 & 4.24). Rabi oscillations on the blue sideband and the carrier are presented in figure 5.11.

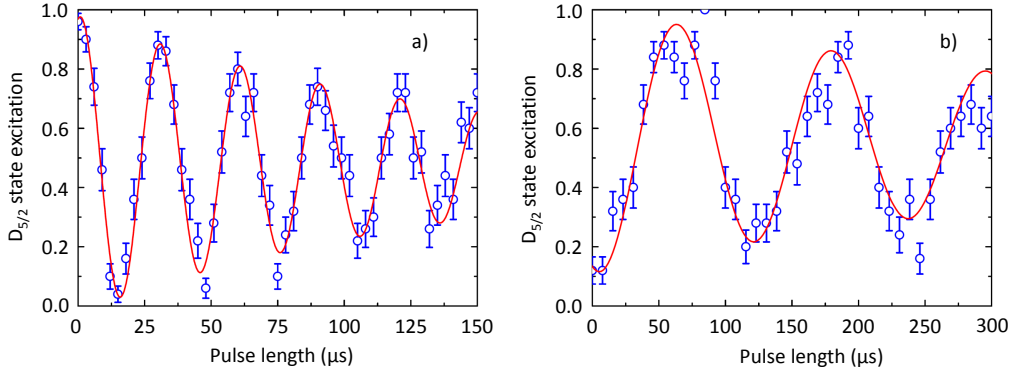


Figure 5.11: *a) Rabi oscillations on the blue out-of-phase mode sideband of the $^1S_0, m_f = 5/2 \leftrightarrow ^3P_1, F = 7/2, m_f = 7/2$ transition measured by quantum logic spectroscopy. After $15 \mu\text{s}$ approximately 95% of the population is transferred to the excited state, which gives rise to the baseline in the Ramsey patterns in chapter 6. The main limitation therefore is high frequency noise of the probe laser (see main text). The error bars are calculated by quantum projection noise for 50 experiments per data point. b) Rabi oscillations on the $^1S_0, m_f = 5/2 \leftrightarrow ^3P_1, F = 7/2, m_f = 7/2$ carrier transition measured by quantum logic spectroscopy. In this experiment, a laser pulse, resonant with the carrier transition, was applied prior to the sideband pulse on the out-of-phase mode.*

This assumption is justified by the fact that the contrast decreases further with higher Rabi frequency. Therefore the Rabi frequency was chosen such that the maximum transfer probability is achieved. The quantum logic experiments that were carried out, start with the $^{40}\text{Ca}^+$ ion being in the excited state. A blue sideband pulse followed by a fluorescence detection provided a check if sideband cooling to the ground state was successful. For this reason the QLS measurements show an inverted signal that starts at an excitation of 1.

6 Measurements

The experimental results achieved in this work are presented in this chapter. It is structured as follows: The first part (section 6.1) describes the experimental investigation of the sympathetic cooling dynamics of aluminium and calcium ions which was published in New Journal of Physics [73]. Theoretical modelling and numerical simulations of the sympathetic cooling dynamics can be found in the publication. In the next section (section 6.2) collective Ramsey experiments with long ion strings were used to investigate the electrical quadrupole shift in a calcium ion string. In section 6.3 an absolute frequency measurement of the $^1S_0 \leftrightarrow ^3P_1$, $F = 7/2$ transition in $^{27}\text{Al}^+$ via quantum logic spectroscopy with a $^{40}\text{Ca}^+$ ion is described. Furthermore the Landé g-factor of the 3P_1 , $F = 7/2$ state was determined. Section 6.4 concludes with a first spectroscopic signal from the $^1S_0 \leftrightarrow ^3P_0$ clock transition.

6.1 Sympathetic cooling

The method for detecting the presence of a hot ion in the trap (see section 5.1) provides detailed information about the sympathetic cooling process. The experiments start with a Doppler-cooled $^{40}\text{Ca}^+$ ion with trapping frequencies of 2 MHz radially and 0.4 MHz axially. After a waiting time of 10 ms two π - pulses on the $S_{1/2}$, $m_j = -1/2 \leftrightarrow D_{5/2}$, $m_j = -3/2$ and $S_{1/2}$, $m_j = 1/2 \leftrightarrow D$, $m_j = 3/2$ transitions were carried out. The internal state of the $^{40}\text{Ca}^+$ ion was detected by electron shelving. The sequence was repeated continuously with 50 experimental cycles per data point. In one experimental cycle an ablation pulse was fired onto the target and the 394 nm photo-ionization laser was turned on with the goal of creating a $^{27}\text{Al}^+$ ion in the trap. As soon as a hot aluminium ion gets trapped it manifests itself as a drop in excitation probability. Over time a trend to lower and lower excitation probabilities is observed which results from the increasing heating rate the calcium ion experiences. Finally the ions crystallize and the excitation probability recovers. The temporal evolution of the excitation probability during the sympathetic cooling process is presented in figure 6.1.

The coupling strength Ω_{nn} on a carrier transition outside the Lamb-Dicke regime depends on the motional state of a vibrational mode and is given by $\Omega_{nn} = \Omega_0 \langle n | e^{i\eta(a+a^\dagger)} | n \rangle$. The excitation probability of a laser pulse that corresponds to a π - pulse for an ion in the Lamb-Dicke regime allows for inferences on the transferred motional quanta during the waiting time.

The mean squared Rabi frequency can be approximated by

$$\langle \Omega^2 \rangle_{\bar{n}} \approx \Omega_0^2 e^{(-2\eta^2 \bar{n})} I_0(2\eta^2 \bar{n}) \quad (6.1)$$

with I_0 being the modified Bessel-function of the first kind.

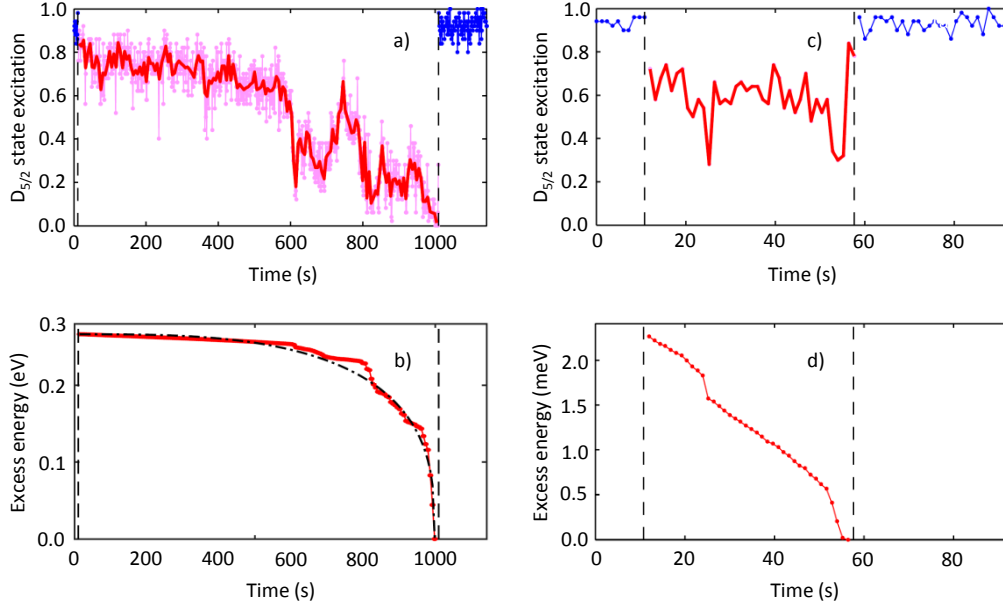


Figure 6.1: Sympathetic cooling dynamics of a $^{27}\text{Al}^+$ ion cooled by one $^{40}\text{Ca}^+$ ion. a) $D_{5/2}$ state excitation probability after a π -pulse on the S - D carrier transition. After a few seconds (left dashed vertical line) a hot $^{27}\text{Al}^+$ ion is created by an ablation pulse. The ions crystallize after 1000 s of sympathetic cooling (right dashed vertical line). The $D_{5/2}$ state population shown as red (pink) dots results from binning 250 (50) experimental cycles. b) Energy of the $^{27}\text{Al}^+$ ion calculated from the binned data in a). The dashed-dotted black line is the temporal energy loss predicted by equation (6.3) with initial energy and cooling time adjusted to fit the experimental data. c) and d) show the same type of signal as a) and b) respectively for a $^{27}\text{Al}^+$ ion that was trapped for about 40 s before getting lost again.

The excitation probability of a laser pulse with a duration $\Omega_0\tau = \pi$ applied to an ion in a thermal state is approximated by [73]

$$p_n = \langle \sin(\Omega_{nn}\tau/2)^2 \rangle \approx \frac{1}{\Omega_0} \sin^2 \left(\frac{\pi}{2} \sqrt{\langle \Omega^2 \rangle_{\bar{n}}} \right). \quad (6.2)$$

Thus the phonons transferred to the calcium ion during the waiting time and furthermore the initial energy of the hot ion can be tracked back. To infer the initial energy of the aluminium ion assumptions have to be made. The heating rate is expected to be spatially isotropic and it is assumed that laser cooling dissipates all the transferred energy such that the calcium ion

stays close to the Lamb-Dicke regime until the final stage of the cooling process. The latter is confirmed by experiments with and without the waiting time before the π - pulses and comparing the excitation probabilities. The excitation without the waiting time (grey data points in figure 6.2 a) is largely close to one but drops at the end of the cooling process. For the conversion of the excitation probability to a heating rate 250 experiment were binned to reduce the influence of quantum projection noise. Sometimes it happened that a hot trapped aluminium ion got lost after seconds to minutes. A possible explanation therefore are collisions with the cooling ion that repartition the kinetic energy among the three spatial directions and the ion escapes along a direction where the trap is not deep enough to confine it. Ions with high kinetic energy might also explore unstable trapping regions.

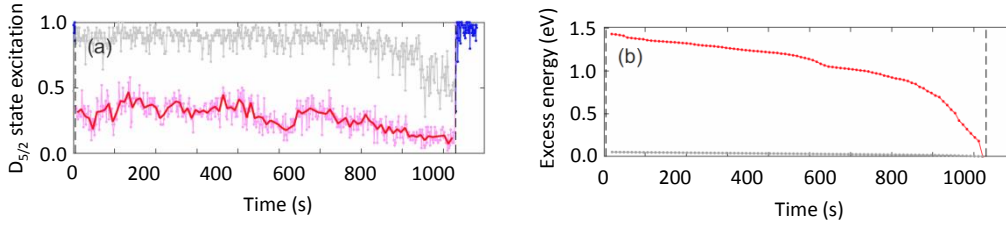


Figure 6.2: Sympathetic cooling dynamics of a $^{27}\text{Al}^+$ ion cooled by one $^{40}\text{Ca}^+$ ion with the same type of curves as in figure 6.1. In this experiment the waiting time for every second data point (grey dots in (a)) was omitted. It ensures that the transfer probability is still high until the end of the cooling process. The error made by assuming that the calcium has zero temperature at the beginning of each experiment is negligibly small (grey line in (b)).

According to a simple sympathetic cooling model, derived in [73] the temporal energy loss of the hot ion is given by

$$E(t) = \sqrt[3]{E(0)^3 - \left(\frac{t}{\tau}\right) \frac{24m_h}{m_c} E_d^3}, \quad (6.3)$$

where $E(0)$ is the initial energy of the hot ion, $\tau = 2\pi/\omega$ is the oscillation period of the hot ion and m_h and m_c are the masses of the hot and the cold ion, respectively. $E_d = \frac{1}{2}m_h\omega^2 d^2 = e^2/4\pi\epsilon_0 d$ is an energy scale with $d = (e^2/2\pi\epsilon_0 m_h \omega^2)^{1/3}$. The time that is needed to extract all energy is expressed by [73]

$$\tau_{cool} = \frac{m_c}{24m_h} \left(\frac{E(0)}{E_d}\right)^3 \tau. \quad (6.4)$$

The cooling time τ_{cool} shows a strong dependence on the initial energy of the hot ion. For a hot aluminium ion with an initial energy of 1 eV and an oscillation frequency of $\omega = (2\pi) 1$ MHz a cooling time of 5000 s is predicted, which is of the same order of magnitude as the cooling time observed in figure 6.2.

Similar measurements were carried out to investigate the sympathetic cooling dynamics of hot $^{40}\text{Ca}^+$ ions as a function of the number of Doppler-cooled $^{40}\text{Ca}^+$ ions present in the trap. In the regime where the Doppler shift is much bigger than the detuning of the cooling laser from resonance, simple models [76] predict cooling rates that scale only weakly with the energy of the ion $dE/dt \sim 1/\sqrt{E}$. Numerical estimates based on [76] predict cooling times of many seconds to minutes for $E_0 = 0.1 \dots 1$ eV for Doppler-cooling settings optimized for achieving low temperatures. These predictions are confirmed by the experimental observations presented in figure 6.3. A mean cooling time of 100 s is found for cooling one hot $^{40}\text{Ca}^+$ ion by a cold one, which is shorter than the cooling times for a hot $^{27}\text{Al}^+$ ion but considerably longer than what is expected from numerical simulations [73]. Shorter cooling times can be achieved by adjusting the laser frequency to the Doppler shift during the cooling process.

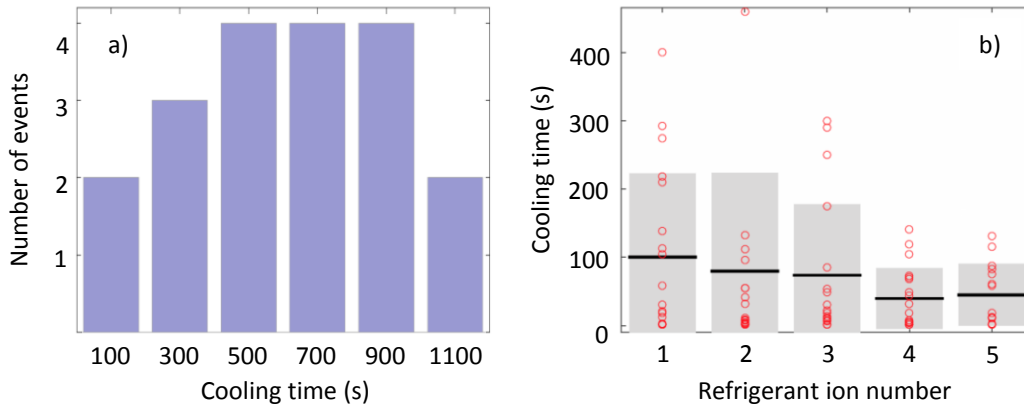


Figure 6.3: a) Distribution of sympathetic cooling times of a hot $^{27}\text{Al}^+$ ion cooled by a $^{40}\text{Ca}^+$ ion. The histogram shows 19 loading events at a bin size of 200 s. A mean cooling time of 600 s is observed. b) Distribution of the sympathetic cooling times of a $^{40}\text{Ca}^+$ ions as function of the number of refrigerant ions (also $^{40}\text{Ca}^+$). The red circles indicate the individual cooling times for each experiment. The black lines show the mean value for each data series with calculated standard deviation error bars in grey. Assuming that the initial energy of the hot ion is identical on average the average cooling time is expected to decrease inversely with the number of ions (due the increased refrigeration power of the string).

The long sympathetic cooling times observed in these experiments are ascribed to the high initial energy of the ions. One part of it is the kinetic energy of laser-ablated atoms. An aluminium atom at a velocity of 1000 m/s has a kinetic energy of 0.14 eV. Since the sympathetic cooling times scale as $\tau \sim E_0^3$, the initial energy E_0 of ions loaded into the trap has to be kept as low as possible. To a certain extent this can be done by a delay between ablation pulse and the photo-ionization beam and therefore selecting the low velocity tail of the distribution. Another contribution is the potential energy of an ion created off-center. An ion created at

$z = 500 \mu\text{m}$ in a conservative harmonic potential with an oscillation frequency of $\omega_z/2\pi = 500$ kHz exhibits a potential energy of $E_{pot} = 0.35$ eV. It is currently not clear if the sympathetic cooling times can be shortened by restricting the ion creation volume to a region around the trap center. In the case of calcium this could be realized by two tightly focused PI beams crossing at the trap center instead of co-propagating beams along the trap axis. For the slowest aluminium atoms a cooling time of a few seconds is predicted [73] but cooling times shorter than a minute were never observed experimentally. In this setup the ions can be created over a rather long distance along the trap axis, which is assumed to be the limiting factor for the cooling times.

6.2 Ramsey correlation spectroscopy

The future of trapped ion optical frequency standards lies in spectroscopy of multi-ion entangled states [12,34]. Contrary to the single ion case the spatial extension of an ion string is on the order of 100 μm along the trap axis for typical trapping conditions.



Figure 6.4: EMCCD camera image of a string of eleven trapped calcium ions. The ions are separated by $\sim 4.4\text{-}6.5 \mu\text{m}$.

Inhomogeneous magnetic and electric fields at the trap as well as the presence of other ions lead to different systematic frequency shifts along the ion string. In the case of $^{40}\text{Ca}^+$ ions the most dominant part is the electric quadrupole shift which can lead to a difference in transition frequency up to 100 Hz from the inner to the outermost ions depending on the axial confinement and the transition to be excited.

The shift arises from a non-spherical charge distribution of the D states that couples to electric field gradients at the position of the ions. These electric field gradients are created by the DC potential along the trap axis and the electric field from other ions present in the trap. Detailed information about the electric quadrupole shift in $^{40}\text{Ca}^+$ can be found in [34,46,77] and references therein. The electric quadrupole moment of an atom in the electronic state $|\gamma, J \neq 0\rangle$ is given by

$$\Theta(\gamma, J) = -e \langle \gamma, J, m_J = J | \sum_{i=1}^N r_i^2 C_0^{(2)}(\theta_i, \varphi_i) | \gamma, J, m_J = J \rangle \quad (6.5)$$

It consists of the sum over all electrons with coordinates r_i, θ_i and φ_i and the normalized spherical harmonic $C_0^{(2)}(\theta_i, \varphi_i) = \sqrt{\frac{4\pi}{5}} Y_{2,0}(\theta_i, \varphi_i)$. The Hamiltonian describing the interaction of the electric quadrupole moment with the gradient of an external electric field denotes $H = \nabla \mathbf{E} \cdot \Theta$. The electric quadrupole moment of the $D_{5/2}$ state of $^{40}\text{Ca}^+$ was measured to be $\Theta(3d, 5/2) = 1.82(1)ea_0^2$ [38] where a_0 is the Bohr radius. The resulting frequency shift to first order for a magnetic sub-level m_j is given by [78,79]

$$\Delta\nu_Q = \frac{1}{4h} \nabla E \cdot \Theta(\gamma, J) \frac{J(J+1) - 3m_j^2}{J(2J-1)} (3\cos^2\beta - 1) \quad (6.6)$$

where β is the angle between the quantization axis and the electric field gradient. A calculation of the electric quadrupole shift for a string of $^{40}\text{Ca}^+$ ions is presented in figure 6.5. The ions in the center of the ion string experience the strongest electric field gradients. Therefore the electric quadrupole shift is biggest for the center ions.

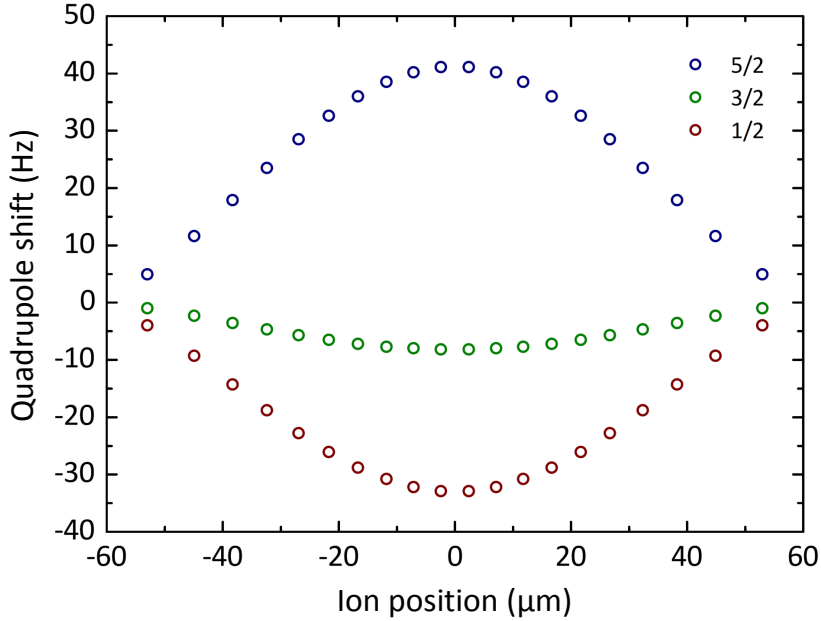


Figure 6.5: Calculated quadrupole shift of the $D_{5/2}, m_j = 1/2, 3/2, 5/2$ levels for a string of 20 ions at an axial confinement of 219 kHz and $\beta = 0$. The calculation uses equilibrium positions at zero temperature. The electric field gradient from the presence of neighboring ions as well as the static field gradient from a harmonic trapping potential was taken into account.

As long as these frequency shifts are well calibrated this does not form an obstacle to build a multi-ion frequency standard. A way to measure the differences in transition frequency is to perform collective Ramsey experiments with Ramsey times beyond the single ion coherence time. During the Ramsey time the Bloch vectors rotate in the equatorial plane. Correlated noise influences the rotation speed and thus washes out the average Bloch vector. A projection of the Bloch vector onto the z -axis of the Bloch sphere leads to a time-dependent parity signal between two ions. The parity signal arises from a measurement whether the z -components of the two Bloch vectors are co- or anti-aligned. One of the outermost ions of the ion string is used as a reference. Oscillations in the parity signal in time correspond to relative transition frequency differences. Typical parity oscillations observed with this method are presented in figure 6.6. The data was taken with the apparatus described in [29] since it is optimized to work with long ion strings.

To separate the influence of an inhomogeneous magnetic field and the electric quadrupole shift, different Zeeman transitions within the $S_{1/2} \leftrightarrow D_{5/2}$ manifold as well as the RF transition between the two $S_{1/2}$ ground states were investigated. The experiments were carried out with a string of 20 ions at an axial and radial confinement of 219 kHz and 2.7 MHz for a single calcium ion respectively. The quantization magnetic field was about 4 G. The inhomogeneities in the magnetic field measured with the $S_{1/2}, m_j = -1/2 \leftrightarrow S_{1/2}, m_j = +1/2$ RF transition

are presented in figure 6.7. The magnetic field gradient along the trap axis was compensated with an anti-parallel coil pair.

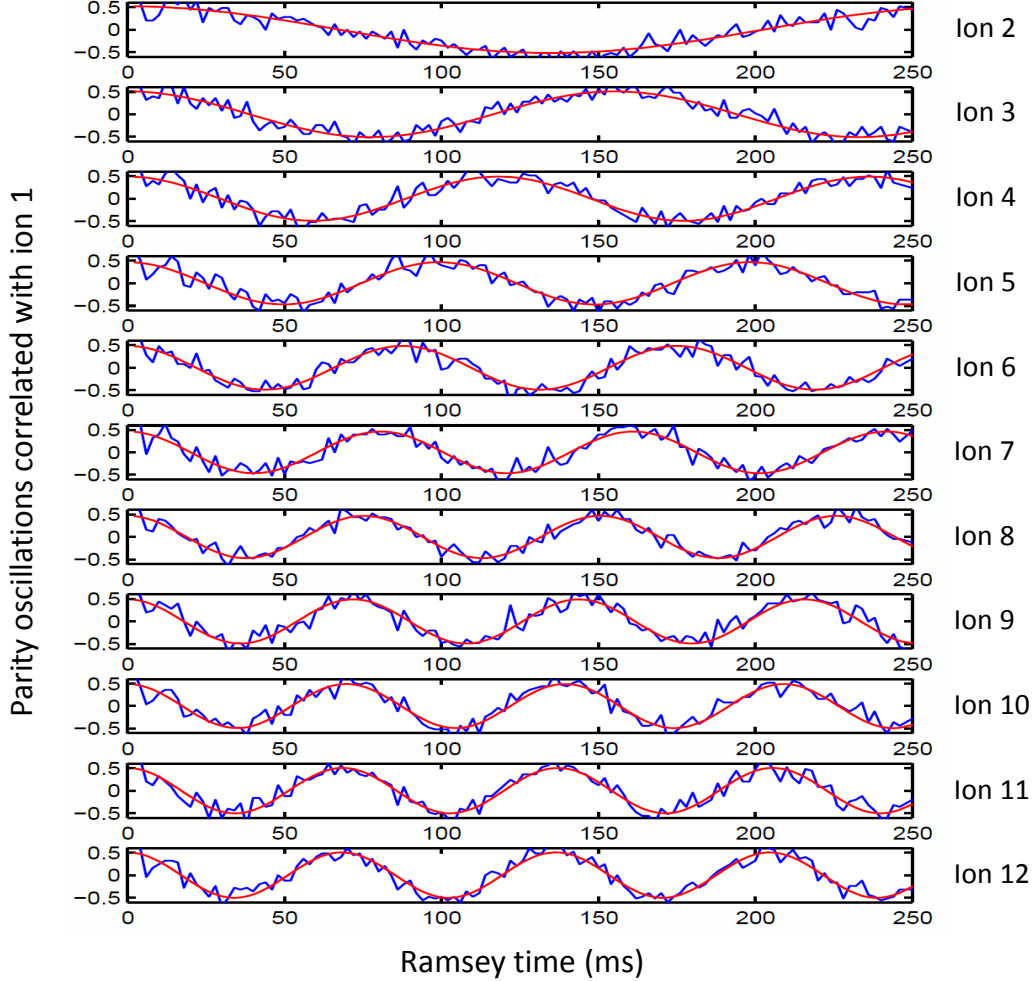


Figure 6.6: Parity oscillations of ions 2-12 correlated with ion 1 (blue curves) inferred from Ramsey experiments on the $S_{1/2}, m_j = +1/2 \leftrightarrow D_{5/2}, m_j = +5/2$ transition with Ramsey times up to 250 ms. The data consists of 4 individual scans with 50 cycles per data point. The transition frequency differences with respect to ion 1 can be determined by a sinusoidal fit (red lines). The data indicates a magnetic field gradient along the ion string since the electric quadrupole shift is expected to be symmetric.

A curvature of the magnetic field, which arises from the non-Helmholtz configuration of the magnetic field coils, is observed which leads to a parabolic distribution of the transition frequency differences. The transition frequency differences along the ion string were fitted with a second order polynomial and the residual frequency offsets from the fit were calculated (see figure 6.7). The W-shaped distribution of the residuals could lead to the assumption that the

origin of the residuals result from higher order terms in the quantization magnetic field.

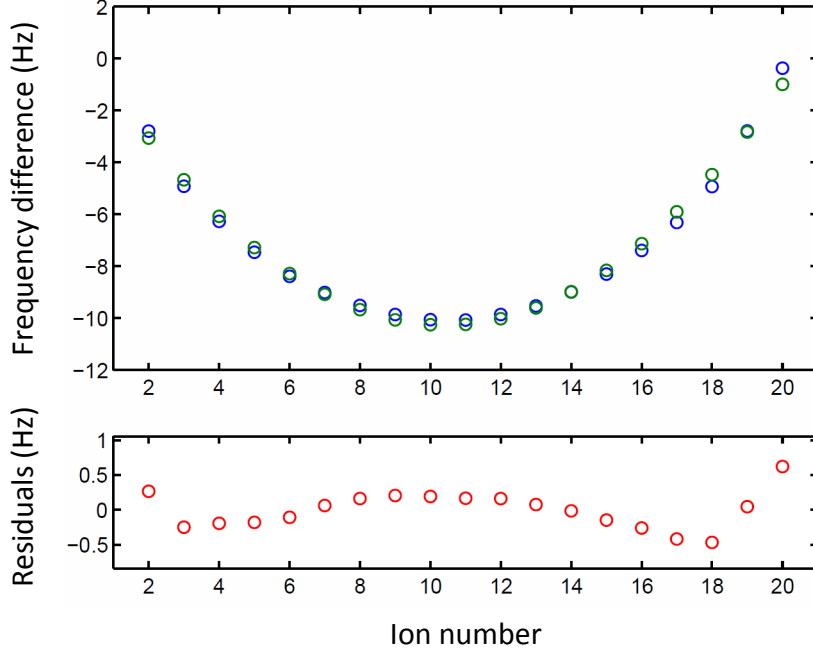


Figure 6.7: Frequency differences of ion 2-20 with respect to ion 1 (blue circles) inferred from Ramsey experiments on the $S_{1/2}, m_j = -1/2 \leftrightarrow S_{1/2}, m_j = +1/2$ RF transition. The magnetic field gradient was compensated with an anti-parallel coil pair. The parabolic shape arises from a curvature of the magnetic field. The difference in the effective magnetic field from the inner to the outermost ions is about $3 \mu\text{G}$ according to the linear Zeeman shift of about 2.8 MHz/G . The data is fitted by a second order polynomial (green circles) and the residual frequency differences between the data points and the parabolic fit are presented in the lower plot (red circles). Residuals of 1 Hz peak to peak are observed.

To investigate this, two approaches were made. First, the endcap voltages were imbalanced which shifted the ion string by about $38 \mu\text{m}$ along the trap axis and the experiment was repeated. The outcome was identical with the data taken at symmetric endcap voltages. A further experiment was carried out at a higher quantization field of 5 G. Again no notable changes with respect to the data presented in figure 6.7 were observed and therefore higher order magnetic field terms could be ruled out.

A possible explanation for the residual transition frequency shifts can be the AC magnetic field at 25 MHz generated by the trap drive [29]. The AC magnetic field off-resonantly couples the Zeeman levels of ground $S_{1/2}, m \leftrightarrow S_{1/2}, m + 1$ and excited $D_{5/2}, m \leftrightarrow D_{5/2}, m + 1$ states which leads to a shift in energy, analogously to the AC Stark shift. This effect is about an order of magnitude stronger compared to the trap in lab 2 for identical radial confinements.

The lower AC-magnetic field-induced shift in the lab 2 setup can be explained by a higher trap drive frequency of 32 MHz (larger detuning), a more symmetric wiring of the trap electrodes and differences in the magnetic susceptibilities of the trap materials.

To investigate the electric quadrupole shift of the D states, Ramsey experiments on the 729 nm transition were carried out in the same way.

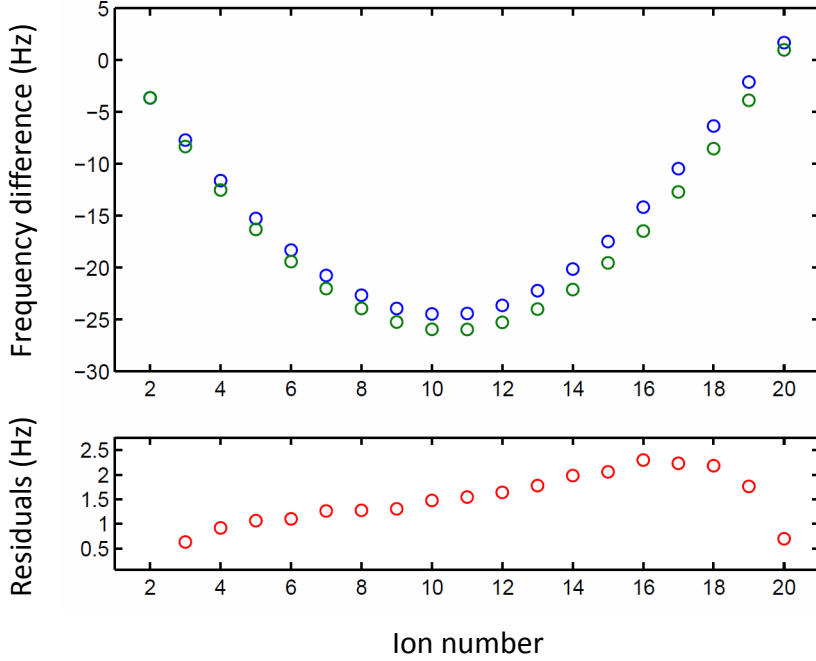


Figure 6.8: Frequency differences of ion 2-20 with respect to ion 1 (blue circles) inferred from Ramsey experiments on the $S_{1/2}, m_j = 1/2 \leftrightarrow D_{5/2}, m_j = 5/2$ transition. The observed frequency shifts are in good agreement with the calculated quadrupole shifts (green circles). The amplitude of the residuals of about 2 Hz is two times higher compared to the Zeeman ground state data. The linear Zeeman shift of the transition frequency is approximately 2 MHz/G which is a factor of 1.4 smaller than the RF transition.

The contribution of the magnetic field curvature was scaled according to the Landé g-factors and subtracted from the signal. The transition frequency differences inferred from Ramsey experiments on the $S_{1/2}, m_j = +1/2 \leftrightarrow D_{5/2}, m_j = 5/2, -3/2, -1/2$ transitions are presented in figures 6.8-6.10. The electric quadrupole shift observed in the experiments is in good agreement with the calculated values. Slight errors in the calculation can arise from the ion motion around the equilibrium positions. Since the electric field gradient around the equilibrium positions is not constant, the mean electric field gradient experienced by the ions differs from the case where the ions are at rest. Expected corrections therefore are on the order of 10^{-2} of the total shift. Uncertainties in the angle between the quantization magnetic

field and the electric field gradient are a further error source.

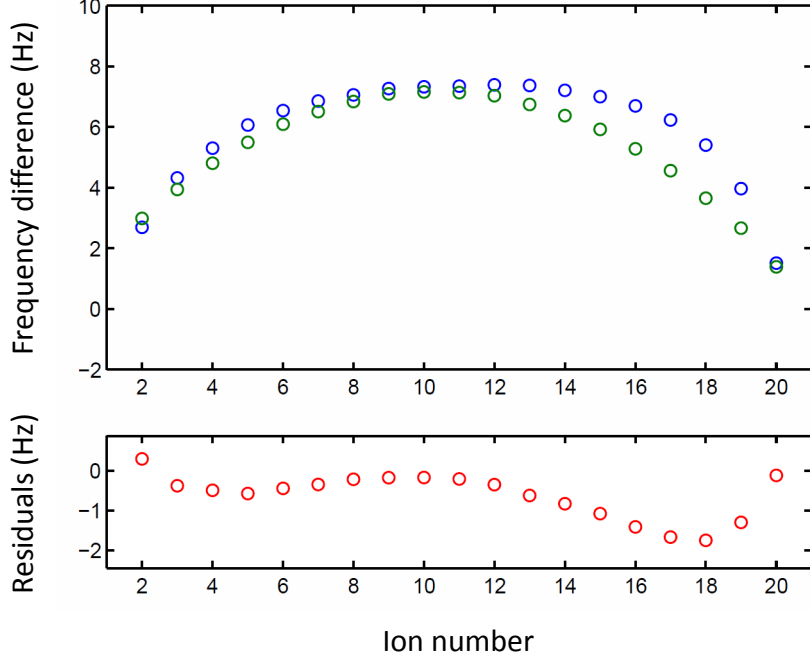


Figure 6.9: Frequency differences of ion 2-20 with respect to ion 1 (blue circles) inferred from Ramsey experiments on the $S_{1/2}, m_j = 1/2 \leftrightarrow D_{5/2}, m_j = -3/2$ transition. The observed quadrupole shifts have a different sign and are a factor ~ 3.5 smaller compared to the $S_{1/2}, m_j = 1/2 \leftrightarrow D_{5/2}, m_j = 5/2$ transition. The linear Zeeman shift of the transition frequency is approximately -2.8 MHz/G. The amplitude of the residuals of about 2 Hz is almost identical to the $S_{1/2}, m_j = 1/2 \leftrightarrow D_{5/2}, m_j = 5/2$ transition.

In all experiments using the optical transition, residuals of about 2 Hz amplitude were observed which is a factor of 2 higher than the residuals using the RF transition. All residual plots show a W-shaped feature which is more pronounced on the right-hand side, which is where the RF blades are connected to the helical resonator. This gives rise to the assumption that the residuals arise from the AC magnetic field produced by the trap, which is expected to be stronger on this side. Finally, two experiments using the RF transition were carried out at different radial confinements. In the second experiment the radial confinement was increased from 2.7 MHz to 3.4 MHz. In the data set with a higher confinement the asymmetry on the right-hand side became bigger (about 1 Hz) which confirmed the assumption that the observed shift is due to the AC magnetic field produced by the trap drive. The corresponding data is presented in figure 6.11.

The residual curves in the presented plots are unequally tilted. Since the current driver, which is used to compensate the magnetic field gradient, is not temperature stabilized its

current output can vary according to changes in the room temperature and therefore can lead to improper compensation of the field gradient.

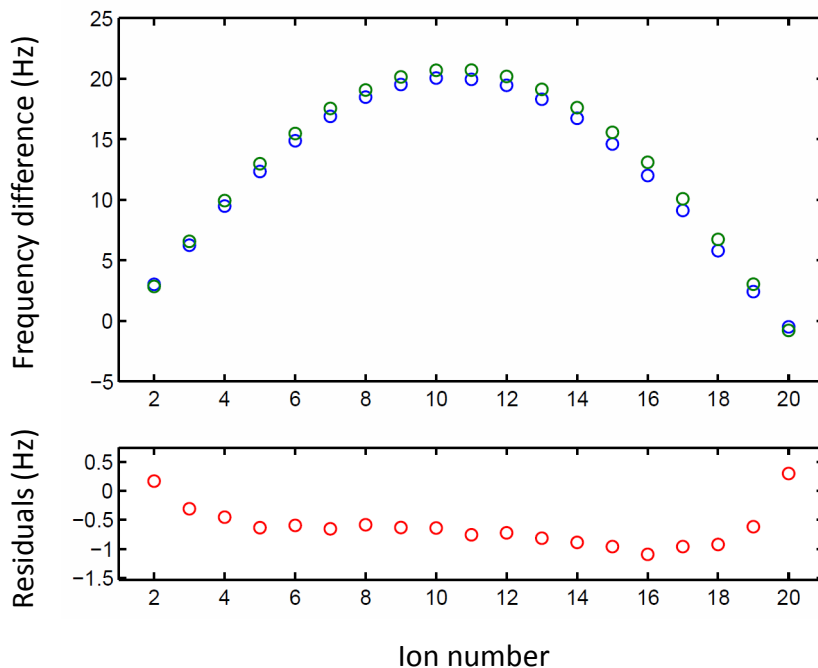


Figure 6.10: Frequency differences of ion 2-20 with respect to ion 1 (blue circles) inferred from Ramsey experiments on the $S_{1/2}, m_j = 1/2 \leftrightarrow D_{5/2}, m_j = -1/2$ transition. The observed quadrupole shifts are a factor ~ 3 bigger compared to the $S_{1/2}, m_j = 1/2 \leftrightarrow D_{5/2}, m_j = -3/2$ transition. The linear Zeeman shift of the transition frequency is with -1.6 MHz/G the smallest of all optical transitions interrogated. The amplitude of the residuals of about 1.5 Hz is slightly smaller compared to the other two optical transitions.

In summary the method of correlated Ramsey experiments describes a relatively simple but powerful method to investigate systematic frequency shifts in ion strings. The frequency resolution depends on the number of data points taken and the maximum Ramsey time. Both parameters have influence on the accuracy of the fits to the parity oscillations. While the number of data points is just a matter of time, the maximum Ramsey time is set by the collision rate with the background gas that leads to melting events of the crystal. For experiments with mixed crystals where one species can be directly cooled during the interrogation, the upper bound is given by the finite lifetime of the excited state. For the complete understanding of all systematic effects more work is needed. Finite element simulations of the AC magnetic field in the trap center with different electrode materials could lead to a more complete picture. Furthermore, a calculation of the mean electric field gradient experienced by ions in an ion string at a finite temperature would be instructive.

With regard to a multi-ion frequency standard the inhomogeneous systematic frequency shifts as well as the observed residual frequency offsets, point out the need of using ionic species that are less sensitive to these kinds of systematic frequency shifts. In the case of aluminium ions these effects are expected to be orders of magnitude smaller and could be therefore disregarded.

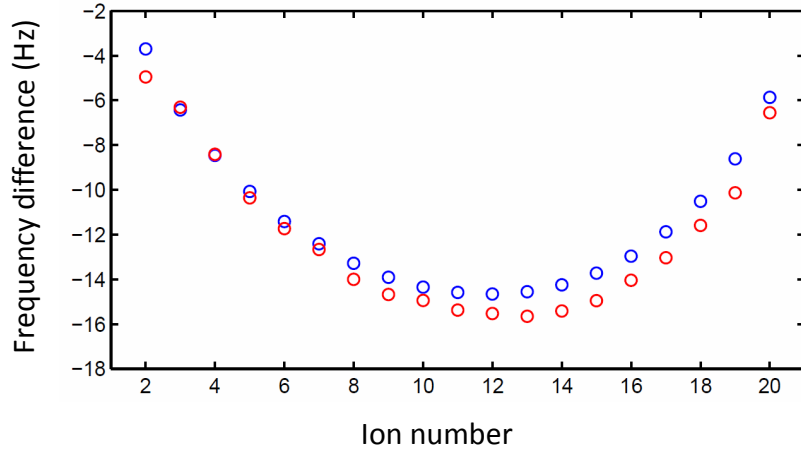


Figure 6.11: Frequency differences of ion 2-20 with respect to ion 1 at different RF confinements inferred from Ramsey experiments on the $S_{1/2}, m_j = -1/2 \leftrightarrow S_{1/2}, m_j = +1/2$ RF transition at radial confinements of 2.7 MHz (blue) and 3.4 MHz (red). Frequency differences of up to 2 Hz are obtained.

6.3 Precision spectroscopy on the $^1S_0 \leftrightarrow ^3P_1$, $F = 7/2$ transition

To perform coherent operations with high fidelity on the $^1S_0 \leftrightarrow ^3P_0$ clock transition in $^{27}\text{Al}^+$ the ion has to be prepared in a certain m_F ground state. This can be achieved by frequency-resolved optical pumping via the $^1S_0 \leftrightarrow ^3P_1$, $F = 7/2$ transition. In order to do this with high efficiency it is necessary to have precise knowledge of the Zeeman transition frequencies and therefore the Landé g-factors of ground and excited state. The g-factor of the ground state is known very accurately [48] but for the excited state only the calculated value of $g_{^3P_1, F=7/2} \approx 3/7$, which neglects relativistic and nuclear corrections, is known. Expected corrections from the nuclear contribution are on the order of $\sim 10^{-3}$. For typical magnetic fields of ~ 4 G this results in a frequency deviation of several 10 kHz between the two outermost transitions. In order to derive the g-factor of the excited state, frequency measurements of the 1S_0 , $m_f = \pm 5/2 \leftrightarrow ^3P_1$, $F = 7/2$, $m_f = \pm 7/2$ transitions were carried out in the quantum logic way. Using Ramsey's method of separated fields [5], the transition linewidth, which was limited by the interaction time of the laser with the ion, could be reduced by a factor of ~ 2 compared to Rabi spectroscopy.

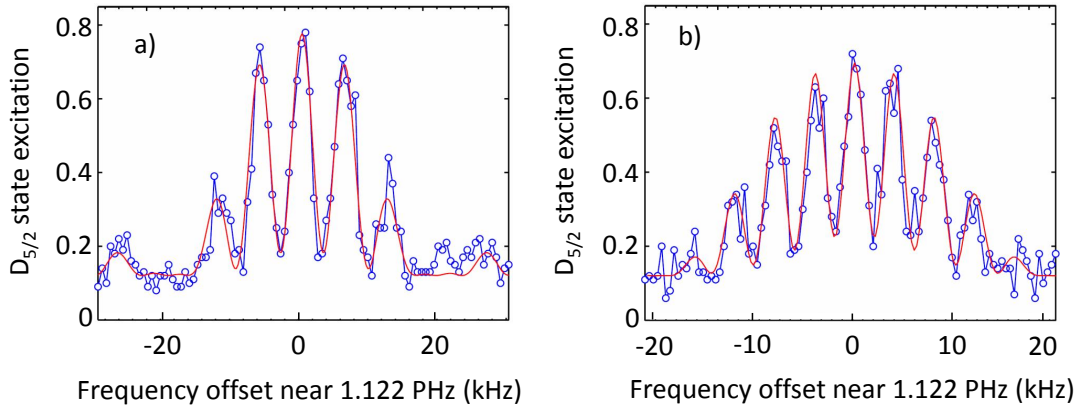


Figure 6.12: Ramsey frequency scans on the 1S_0 , $m_f = 5/2 \leftrightarrow ^3P_1$, $F = 7/2$, $m_f = 7/2$ transition with $50 \mu\text{s}$ long $\pi/2$ -pulses and Ramsey times of a) $100 \mu\text{s}$ and b) $200 \mu\text{s}$. The red line is a simulation based on solving the optical Bloch equations. The simulation results are rescaled to take into account the finite efficiency of the state-mapping procedure. Each data point is the average of the results of 50 experimental cycles.

The 729 nm clock transition in $^{40}\text{Ca}^+$ was used as a frequency reference and allowed one to calibrate the magnetic field at the position of the ions (see section 5.3). Therefore Ramsey experiments with a Ramsey time of 2 ms were performed on the $S_{1/2}$, $m_j = \pm 1/2 \leftrightarrow D_{5/2}$, $m_j = \pm 3/2$ transitions. To speed up the measurements, only Doppler-cooling was performed for the calcium interrogation. On each of the two calcium transitions two data points were taken with phases of the second Ramsey pulse of $\pm\pi$, respectively. Each data point consists of 100 experi-

mental cycle. With this, the frequency offset between 729 nm laser and the transition as well as the magnetic field can be determined. With precise knowledge of the 729 nm laser frequency, the repetition rate of the frequency comb, which was referenced to the GPS disciplined OCXO during the measurements, can be recalculated and therefore allows one to calculate the 267 nm laser frequency from its fundamental frequency at 1068 nm. In order to measure the frequency offset between the 267 nm laser and the probed atomic transition, Ramsey experiments on the $^1S_0, m_f = \pm 5/2 \leftrightarrow ^3P_1, F = 7/2, m_f = \pm 7/2$ transitions were carried out subsequently. Each transition was interrogated with four measurements with phases of the second pulse of $0, \pi/2, \pi$ and $-\pi/2$. Each data point consists of 100 experimental cycles. The four phases of the second pulse enable a reconstruction of the Bloch vector, which is important when the laser drifts and the transitions are not probed on the slopes of the center fringe any more. The measurements were carried out in the following order:

1. Al $^1S_0, m_f = \pm 5/2 \leftrightarrow ^3P_1, F = 7/2, m_f = \pm 7/2 \phi = 0$
2. Al $^1S_0, m_f = \pm 5/2 \leftrightarrow ^3P_1, F = 7/2, m_f = \pm 7/2 \phi = \pi/2$
3. Al $^1S_0, m_f = \pm 5/2 \leftrightarrow ^3P_1, F = 7/2, m_f = \pm 7/2 \phi = \pi$
4. Al $^1S_0, m_f = \pm 5/2 \leftrightarrow ^3P_1, F = 7/2, m_f = \pm 7/2 \phi = -\pi/2$
5. Ca $S_{1/2}, m_j = +1/2 \leftrightarrow D_{5/2}, m_j = +3/2 \phi = \pi/2$
6. Ca $S_{1/2}, m_j = -1/2 \leftrightarrow D_{5/2}, m_j = -3/2 \phi = -\pi/2$
7. Ca $S_{1/2}, m_j = -1/2 \leftrightarrow D_{5/2}, m_j = -3/2 \phi = \pi/2$
8. Ca $S_{1/2}, m_j = +1/2 \leftrightarrow D_{5/2}, m_j = +3/2 \phi = -\pi/2$

In total, one set of measurements consists of 50 repetitions of the sequence described above. For each stretched Zeeman transition on the aluminium 4 data sets were taken (8 in total) with Ramsey times on the aluminium of either 100 μs or 200 μs . The latter increases the slope by a factor of 1.6 compared to the 100 μs data. The spectroscopy laser intensities for both species were adjusted to $\pi/2$ - times of 50 μs in order to keep AC Stark shifts from the probe laser low. Ramsey frequency scans on the aluminium transition and numerical fits of those for both Ramsey times are presented in figure 6.12. The visibility of the fringes is mainly limited by imperfect state detection. The Ramsey contrast on the intercombination transition as a function of the Ramsey time is presented in figure 6.13. For Ramsey times up to 100 μs the contrast is mainly limited by high frequency noise of the laser. For longer Ramsey times the contrast is at its theoretical limit which is given by the natural lifetime of the excited state (305 μs).

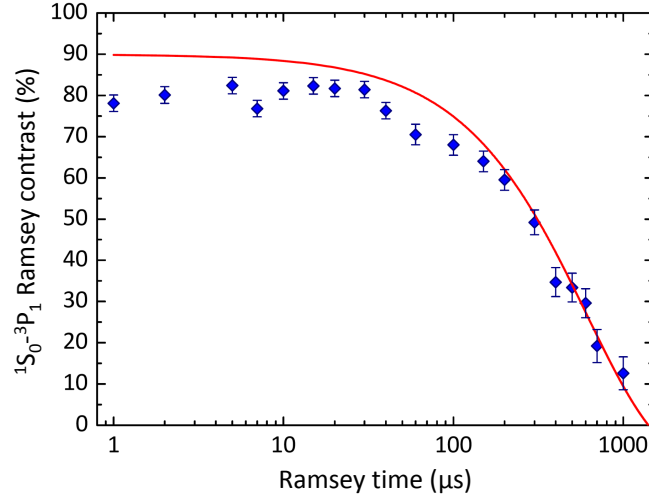


Figure 6.13: Ramsey contrast on the 1S_0 , $m_f = 5/2 \leftrightarrow ^3P_1$, $F = 7/2$, $m_f = 7/2$ carrier transition measured by quantum logic spectroscopy (blue data points). An overall contrast reduction of 10% results from imperfect mapping pulses. For Ramsey times between $1 \mu\text{s}$ and $100 \mu\text{s}$ the contrast suffers from high frequency noise of the laser (see also figure 5.11). For Ramsey times beyond $100 \mu\text{s}$ the contrast is at the theoretical limit, set by the natural lifetime of the excited state. The red line indicates an ideal Ramsey contrast, only limited by the natural lifetime of the excited state and imperfect state detection.

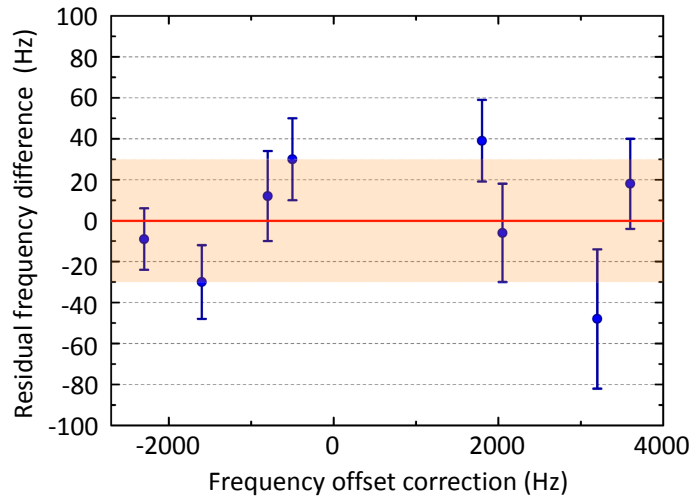


Figure 6.14: Residual frequency differences. The y axis presents the residuals of the 8 frequency data sets, extrapolated to $B = 0$. The inferred frequency offset between laser and transition is shown on the x axis. The scatter of the data points leads to a statistical uncertainty of 30 Hz (1σ) according to the standard deviation. Laser frequency variations during the experiment could lead to an error of up to 12 Hz. Therefore a total uncertainty of 42 Hz is assumed.

For the evaluation the Ramsey experiments on both ions and the comb measurements were averaged separately and the errors were summed up. Data points where the comb measurement was not reliable were omitted. The error bars of each data set are calculated from the scatter of the 50 reconstructed transition frequencies. The error bars are slightly bigger than what is expected from quantum projection noise. Plotting the 8 mean transition frequencies versus the mean magnetic field and interpolating the data linearly to $B = 0$ leads to the transition frequency. The residual frequency differences of the 8 data sets are presented in figure 6.14.

Systematic frequency shifts

In the following section a summary of the relevant frequency shifts of both transitions is given. In view of the spectral width of the transition, only significant frequency shifts are considered. Systematic effects with shifts and uncertainties that are expected to be substantially smaller than 1 Hz are briefly mentioned at the end for the sake of completeness. A detailed evaluation of all relevant frequency shifts of the 729 nm transition can be found in [34] and references therein.

729 nm reference

There are three absolute frequency measurements of the $S_{1/2} \leftrightarrow D_{5/2}$ transition in $^{40}\text{Ca}^+$ mentioned in literature. The mean frequency with a conservative estimate of its uncertainty is 411 042 129 776 396.6(8.7) Hz. In order to ensure that there is no overlooked systematic frequency shift on the 729 nm transition which would distort the results, a transition frequency comparison between single calcium ions in lab 1, lab 2 and the university was made. For this purpose Ramsey experiments on the $S_{1/2}, m_j = \pm 1/2 \leftrightarrow D_{5/2}, m_j = \pm 3/2$ transitions with a Ramsey time of 3 ms were carried out in each experiment to measure the frequency difference between the 729 nm laser and the ions. The frequency difference between the two 729 nm lasers in lab 1 and the university was recorded with an optical beat note between them. Therefore the 729 nm light from the university was sent via a noise-cancelled, 400 m long optical fiber to lab 1. The transition frequency difference between the labs for a measurement duration of 6 hours is presented in figure 6.15. Putting everything together the $S_{1/2} \leftrightarrow D_{5/2}$ transition frequencies in all three experiments agreed well within 1 Hz. Consequently an additional uncertainty of 1 Hz of the S-D transition frequency is taken into account for the evaluation of the $^1\text{S}_0 \leftrightarrow ^3\text{P}_1, F = 7/2$ transition frequency in $^{27}\text{Al}^+$.

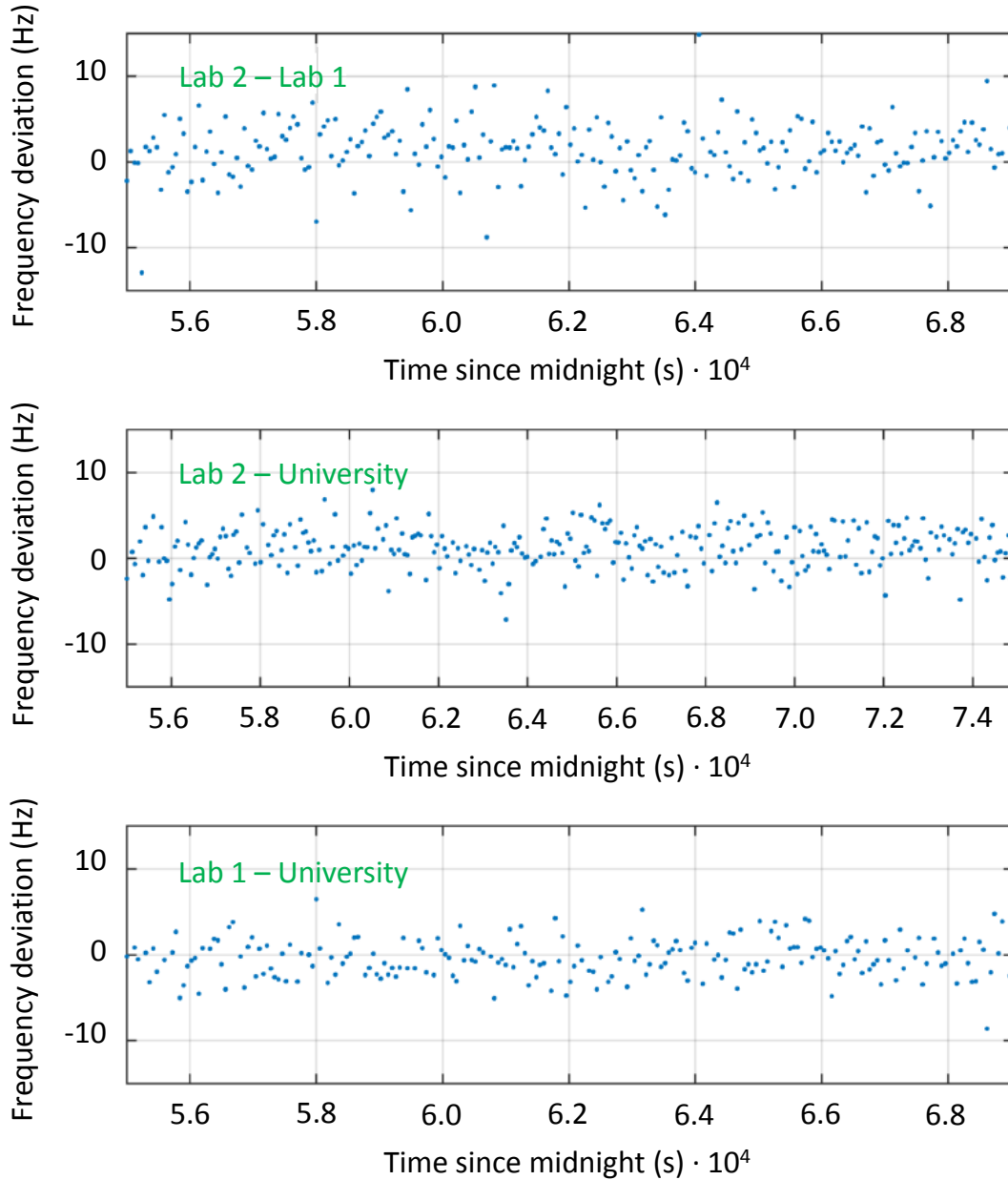


Figure 6.15: Comparison of the 729 nm transition frequencies in lab 1, lab 2 and the linear trap experiment at the university, inferred from Ramsey experiments on the $S_{1/2}$, $m_j = \pm 1/2 \leftrightarrow D_{5/2}$, $m_j = \pm 3/2$ transitions with a Ramsey time of 3 ms for a period of 6 hours. The 729 nm light from the university lab was sent along a 400 m long path-length stabilized optical fiber and the frequency difference was detected via an optical beat note in lab 1. The data points represent the measured frequency difference without any correction of systematic effects. Taking different electric quadrupole shifts into account, all three signals agree well within 1 Hz. The residual deviations can be explained by slightly different quadratic Zeeman shifts, different AC Stark shifts caused by black body radiation and a gravitational shift $\frac{\Delta\nu}{\nu} = \frac{g\Delta h}{c^2}$ of 0.2 Hz from an elevation difference of $\Delta h = 4.5$ m between the IQOQI labs and the university lab [34].

Electric quadrupole shift

The electric quadrupole shift has two contributions. First the electric field gradient resulting from the axial confinement and second an additional electric field gradient resulting from the presence of the second ion. The combined first- and second-order shift on the $S_{1/2}, m_j = \pm 1/2 \leftrightarrow D_{5/2}, m_j = \pm 3/2$ transition is calculated to be 2.7(0.003) Hz for the confinement used during the experiments. The error is dominated by the uncertainty of the ion to ion distance.

Since electronic states with $J > 1/2$ can have a finite electric quadrupole moment [14], the 3P_1 state in $^{27}\text{Al}^+$ can be also shifted in energy. The electric quadrupole moment of the 3P_1 state is not known. Although it is expected to be small, a conservative estimate of $<1.5ea_0^2$ is made. An upper bound of the shift can be calculated by using equation 6.4 and assuming electronic states $^3P_1, J = 1, m_j = \pm 1$ and therefore ignoring the nuclear spin. This would lead to frequency shifts < 11.25 Hz. Even though the sign of the shift (-) is known, a symmetric error is given.

Second order Zeeman shift

Coupling of the $D_{5/2}, m_j = \pm 3/2$ levels in $^{40}\text{Ca}^+$ with the corresponding sublevels of the $D_{3/2}$ state introduces a small quadratic frequency shift, which can be calculated by second order perturbation theory to [80]

$$\Delta\nu = \kappa \frac{(\mu_B B)^2}{\hbar^2 \nu_{FS}} \quad (6.7)$$

where ν_{FS} is the fine structure splitting, J_m is the larger one of the J numbers and a constant $\kappa = \frac{(J_m - L + S)(J_m + L - S)(L + S + 1 + J_m)(L + S + 1 - J_m)}{4J_m^2(2J_m - 1)(2J_m + 1)}(J_m^2 - m_j^2)$ depending on the magnetic sublevel m_j . For an average magnetic field of 4.0464(1) G during the measurements the $m_j = \pm 3/2$ levels ($\kappa = 4/25$) were up-shifted by 2.821(0.005) Hz.

The quadratic Zeeman shift of the $^3P_1, F = 7/2, m_f = \pm 7/2$ levels in $^{27}\text{Al}^+$ can be determined in a similar way. All levels besides the 3P_0 and 3P_2 states are separated by optical frequencies and therefore do not contribute significantly. Since the 3P_0 does not have any $F = 7/2$ components, only the coupling to the 3P_2 state needs to be considered. With a fine structure splitting of 3.71(1) THz [54] the $^3P_1, F = 7/2, m_f = \pm 7/2$ levels ($\kappa = 1/4$) were down-shifted by 2.16(1) Hz. The error is due to the uncertainty in the hyperfine splitting which is expected to be less than 10 GHz.

Minor Frequency shifts

There are several systematic effects which shift both transition frequencies by negligible amounts. For the sake of completeness they are briefly mentioned. During the Ramsey experiments all

laser fields are turned off by switching off the RF that drives the AOMs in the corresponding paths. Each path consists of a double pass and a single pass AOM. The combined attenuation of the transmitted light is about 90 dB. There are two sorts of stray light that still reach the ions, either stray light from the zero order beam of the AOM or light that is close to resonance resulting from insufficiently switching off the RF. Resulting AC Stark shifts from all involved lasers as well as from black body radiation are expected to be well below 1 Hz [81]. The Stark shift contribution from the ion's thermal motion and micromotion, leading to the experience of a non zero mean-squared electric field, is on the order of a few mHz [34]. The second order Doppler shift caused by the secular motion of the ions is of the same size. The gravitational shift resulting from an elevation difference between the calcium and the aluminium ion of less than 10 μm is below 1 μHz . The Ramsey phase error resulting from the finite phase resolution of the pulse box is also well below 1 Hz. Slight variations in the Ramsey contrast of the $S_{1/2}, m_j = \pm 1/2 \leftrightarrow D_{5/2}, m_j = \pm 3/2$ transition are negligible. The Ramsey contrast on the aluminium transition is known for each interrogation because of the four different phases of the second Ramsey pulse. All significant frequency shifts are listed in table 6.1.

Effect	Ca shift (uncertainty) [Hz]	Al shift (uncertainty) [Hz]
Literature	0 (8.7)	- (-)
Lab comparison	0 (1)	- (-)
2nd order Zeeman	+2.821 (0.005)	-2.16 (0.01)
Electric quadrupole	-2.7 (0.003)	0 (11.25)
Statistics	- (-)	0 (42)
Total shift	+0.121 (10)	-2.16 (54)

Table 6.1: Error budget of both transition frequencies. Significant systematic frequency shifts and their uncertainties are presented in units of Hz. The individual shifts are added up, the uncertainties are added and rounded up to an integer number. Shifts and uncertainties in the 729 nm transition are up-scaled with respect to the frequency ratio of both transitions and added to the 267 nm transition error budget. Treating the uncertainties of both transitions as independent errors leads to a combined uncertainty of 61 Hz.

Putting everything together the absolute frequency of the $^1S_0 \leftrightarrow ^3P_1, F = 7/2$ transition in $^{27}\text{Al}^+$ is 1 122 842 857 334 691(61) Hz. The uncertainty is well below the natural linewidth of the transition.

Determination of the Landé g-factor

The set of 8 frequency measurements provides four frequency values for each of the $^1S_0, m_f = \pm 5/2 \leftrightarrow ^3P_1, F = 7/2, m_f = \pm 7/2$ transitions. From this, the mean values for each transition frequency are calculated. The statistical error bars are calculated by the standard deviation. The Landé g-factor of the excited state is inferred from the frequency difference of the two transitions, and the magnetic field which was calibrated with 729 nm transition.

The ion trap creates an AC magnetic field at 32 MHz at the position of the ions. The magnetic field, calibrated by the Zeeman splitting of the $S_{1/2}, m_j = \pm 1/2 \leftrightarrow D_{5/2}, m_j = \pm 3/2$ transitions in $^{40}\text{Ca}^+$, increases by 9.7(1.2) $\mu\text{G}/\text{W}$ when increasing the RF power, going into the helical resonator. This effect is expected to be smaller for aluminium since the Zeeman splitting of ground and excited state is smaller compared to the case of calcium. During the experiments the trap was operated at 1 W. Since this effect is rather small ($\sim 10^{-6}$), it is not taken into account. Consequently a conservative error is given. The magnetic field gradient along the trap axis of 29(8) mG/m, which was calibrated by Ramsey correlation spectroscopy with a string of calcium ions, is also negligibly small. Finally the Landé g-factor yields to $g_{^3P_1, F=7/2} = 0.42884(1)$. The measured value is 0.06 % bigger than the calculated value of $3/7$.

6.4 Observation of the $^1S_0 \leftrightarrow ^3P_0$ clock transition

At the end of this work a first signal of the clock transition in $^{27}\text{Al}^+$ was observed. To detect the electronic excitation of the $^1S_0 \leftrightarrow ^3P_0$ clock transition, a 1 ms long excitation pulse was introduced into the experimental sequence directly before the quantum logic state mapping happens. In the case of no excitation on the clock transition the blue sideband pulse on the intercombination transition can be carried out and the resulting phonon gets mapped to the internal state of the calcium which is detected by electron shelving. In the case of the aluminium ion being in the excited clock state, the blue sideband pulse on the intercombination transition will remain without consequences.

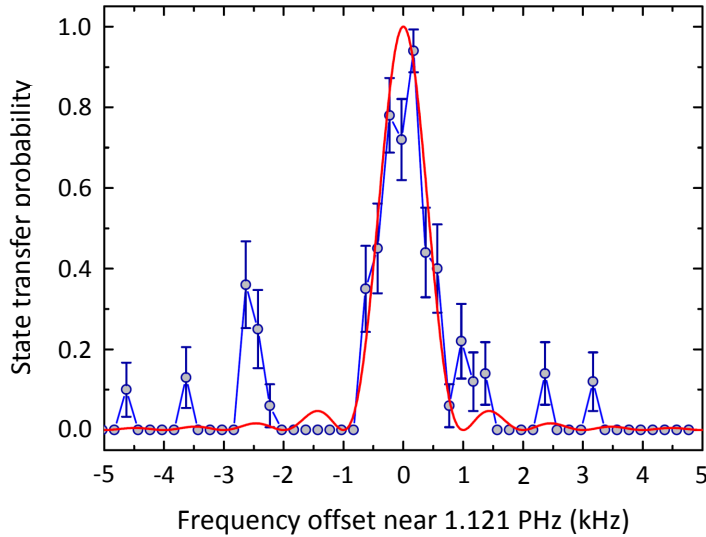


Figure 6.16: Excitation spectrum on the $^{27}\text{Al}^+$ $^1S_0, m_f = -5/2 \leftrightarrow ^3P_0, m_f = -3/2$ clock transition observed via quantum logic spectroscopy with a co-trapped $^{40}\text{Ca}^+$ ion. With 1 ms long excitation pulses a state change probability of ~ 0.9 was achieved on resonance. Consequently the pulse area on resonance was about π . Each data point consists of 20 experimental cycles. The error bars are calculated from quantum projection noise. The spike at -2.5 kHz arises from a collision of one of the ions with the background gas (observed on the EMCCD camera). The small spikes can be explained by poor statistics. The red line is a Fourier transform of the excitation pulse.

Since no method to initialize the aluminium ion in the ground state was used so far, the aluminium ion is either in the ground or the excited state at the beginning of each experimental cycle. Therefore it is useful to look at the state change probability from shot to shot. An excitation spectrum is presented in figure 6.16. The $^1S_0, m_f = -5/2 \leftrightarrow ^3P_0, m_f = -3/2$ transition was driven with a sigma polarized beam along the quantization axis. In order to get rid of false detections where ground state cooling was not successful, each experiment was

repeated twice while during the second run the clock laser was turned off. Only experiments with the same outcome contribute to the signal. However, collision events with the background gas can lead to false counts since the outcome of the state detection is random if the ions are not crystallized. The spectral width of the peak of about 800 Hz FWHM is Fourier-limited. The laser beam with a power of 1.5 mW was focused to a Gaussian beam waist of 65 μm FWHM at the ion. The corresponding Rabi frequency in the center of the beam was estimated to a few kHz. During the experiments involving the clock transition the formation of AlH^+ ions was observed after 15 minutes on average. At experiments only using the intercombination transition this was rarely a problem. A possible explanation therefore is that the chemistry only occurs when the ion is in the excited state. The time which the ion spends in the excited state is about 50% for the clock transition and about 0.1% for the intercombination transition. The AlH^+ ionic molecule can be photo-dissociated with two pulsed lasers at 360 nm and 266 nm [82] but not with the lasers available, which requires to release the ions and reload a mixed ion crystal.

7 Summary and outlook

The work presented in this thesis covers a large amount of technical work as well as three publications in the field of precision spectroscopy and atomic physics.

The technical part describes the construction of a new ion trap which was optimized for precision spectroscopy. Furthermore, a total of eleven laser systems were set up for the means of precision spectroscopy with trapped aluminium and calcium ions.

The main scientific results of this work cover three major topics: During the implementation of laser ablation loading of ions a technique to detect the presence of a hot ion in the trap was developed. This method provides information of the sympathetic cooling dynamics and allows us to trace back the initial energy of the hot ion. Statistical analysis of the sympathetic cooling times were carried out. Furthermore the limitations for the cooling times were discussed and different strategies to decrease the cooling times were pointed out.

Moreover, a method to investigate systematic frequency shifts in an ion string was developed. With ion strings containing up to 20 $^{40}\text{Ca}^+$ ions, Ramsey experiments with Ramsey times up to 300 ms were carried out. Oscillations in the parity signal between two ions give some indication about their difference in transition frequency. Thereby relative systematic frequency shifts between the ions could be determined with sub-Hertz resolution. This method allows one to investigate the homogeneity of the quantization magnetic field along the ion string with high resolution which is important for multi-ion frequency standards. The main focus was to investigate the electric quadrupole shift, which is the biggest systematic frequency shift in calcium ion strings for typical experimental parameters. Meanwhile another systematic effect, the AC Zeeman effect, emerged, which caused frequency shifts up to 2 Hz among the calcium ions and needs further investigation for a complete understanding. Finite element simulations of the AC magnetic field, produced by the trap drive, at the position of the ions would be useful. In conclusion a powerful method to investigate systematic frequency shifts in ion strings was presented.

Once a mixed crystal could be loaded, the two optical transitions in $^{27}\text{Al}^+$ were observed via quantum logic spectroscopy with a co-trapped $^{40}\text{Ca}^+$ ion. The frequency of the $^1\text{S}_0 \leftrightarrow ^3\text{P}_1$, $F = 7/2$ transition was measured and the g-factor of the excited ($g_{^3\text{P}_1, F=7/2}$) state was determined using the clock transition in $^{40}\text{Ca}^+$ as a frequency reference and a magnetic field sensor. The transition frequency was measured with an accuracy well below the natural linewidth of the transition, using Ramsey's method of separate oscillatory fields.

Finally the $^1S_0 \leftrightarrow ^3P_0$ clock transition in $^{27}\text{Al}^+$ was observed via quantum logic spectroscopy, which was the second time worldwide to my knowledge.

During experiments using the clock transition the formation of AlH^+ molecular ions, which can not be photo-dissociated with the lasers present in the lab, became an obstacle since it is time consuming to load another mixed ion crystal. This molecular ion can be photo-dissociated with two pulsed lasers at 360 nm and 266 nm [82] which would make the work much more efficient. The 266 nm light could be produced by frequency doubling of the ablation laser at 532 nm.

So far, the internal state of the $^{27}\text{Al}^+$ ion was detected via quantum logic spectroscopy via the intercombination transition. The detection fidelity is limited by high frequency noise of the diode laser which drives the transition and should be replaced by either a laser diode that allows for a faster feedback or a fiber laser which is intrinsically more stable. This would also improve the fidelity of the pump pulses and therefore make optical pumping more efficient.

Other detection methods like [83] that do not rely on sideband cooling and could speed up the measurements and enhance the detection fidelity. Sympathetic cooling of the aluminium ion during longer interrogations could reduce melting events of the ion crystal caused by collisions with the background gas. Faster recrystallization can be achieved by lowering the trapping confinement for a short amount of time after a collision.

Efficient cooling of the radial modes is crucial for coherent operations on the $\Delta m = 0$ transitions in $^{27}\text{Al}^+$ in this setup. Sympathetic Raman [11] or EIT cooling could help to cool the ion crystal to a near 3D ground state. Furthermore these cooling techniques allow one to reduce uncertainties in motional frequency shifts and therefore make aluminium ion clocks operating at the 10^{-19} level possible [11].

A Appendix

Table of fundamental constants according to CODATA [84].

Quantity	Symbol	Numerical value	Unit
speed of light in vacuum	c	299792458	m/s
magnetic constant	μ_0	$4\pi \cdot 10^{-7}$	N/A^2
electric constant $1/\mu_0 c^2$	ϵ_0	$8.854187817... \times 10^{-12}$	F/M
Newtonian constant of gravitation	G	$6.67408(31) \times 10^{-11}$	$m^3/kg \cdot s$
Planck constant	h	$6.626070040(81) \times 10^{-34}$	$J \cdot s$
$h/2\pi$	\hbar	$1.054571800(13) \times 10^{-34}$	$J \cdot s$
elementary charge	e	$1.6021766208(98) \times 10^{-19}$	C
magnetic flux quantum $h/2e$	Φ_0	$2.067833831(13) \times 10^{-15}$	Wb
conductance quantum $2e^2/h$	G_0	$7.7480917310(18) \times 10^{-5}$	S
electron mass	m_e	$9.10938356(11) \times 10^{-31}$	kg
proton mass	m_p	$1.672621898(21) \times 10^{-27}$	kg
proton-electron mass ratio	m_p/m_e	1836.15267389(17)	
fine-structure constant $e^2/4\pi\epsilon_0\hbar c$	α	$7.2973525664(17) \times 10^{-3}$	
inverse fine-structure constant	α^{-1}	137.035999139(31)	
Rydberg constant $\alpha^2 m_e c/2h$	R_∞	10973731.568508(65)	$1/m$
Avogadro constant	N_A	$6.022140857(74) \times 10^{23}$	$1/mol$
molar gas constant	R	8.3144598(48)	$J/mol \cdot K$
Boltzmann constant R/N_A	k_B	$1.38064852(79) \times 10^{-23}$	J/K
Stefan-Boltzmann constant $(\pi^2/60)k^4/\hbar^3 c^2$	σ	$5.670367(13) \times 10^{-8}$	$W/m^2 \cdot K^4$
electron volt (e/C) J	eV	$1.6021766208(98) \times 10^{-19}$	J
(unified) atomic mass unit $\frac{1}{12}m(^{12}C)$	u	$1.660539040(20) \times 10^{-27}$	kg

B Journal publications

- M. Guggemos, D. Heinrich, O. A. Herrera-Sancho, R. Blatt, and C. Roos. Sympathetic cooling and detection of a hot trapped ion by a cold one. *New Journal of Physics*, 17(10):103001, 2015.
- M. Guggemos, D. Heinrich, O. A. Herrera-Sancho, R. Blatt, and C. F. Roos. Quantum logic spectroscopy with a $^{27}\text{Al}^+$ / $^{40}\text{Ca}^+$ ion crystal (to be submitted to NJP)
- M. Guggemos, C. Hempel, R. Blatt, and C. F. Roos. Ramsey correlation spectroscopy with long ion strings (to be published)

Bibliography

- [1] J. Jespersen and J. Fitz-Randolph. *From Sundials to Atomic Clocks: understanding Time and Frequency*. Dover Publications Inc., 2003.
- [2] J. Curie and P. Curie. Development, via compression, of electric polarization in hemihedral crystals with inclined faces. *Bulletin de la Societe de Mineralogique de France*, 3:90–93, 1880.
- [3] I. I. Rabi, J. R. Zacharias, S. Millman, and P. Kusch. A New Method of Measuring Nuclear Magnetic Moment. *Phys. Rev.*, 53:318, 1938.
- [4] N. F. Ramsey. History of atomic clocks. *JOURNAL OF RESEARCH of the National Bureau of Standards*, 88:301–320, 1983.
- [5] N. F. Ramsey. A molecular beam resonance method with separated oscillatory fields. *Phys. Rev.*, 78:695–699, 1950.
- [6] G. Santarelli, P. Laurent, and P. Lemonde. Quantum projection noise in an atomic fountain: A high stability cesium frequency standard. *Physical Review Letters*, 82:4619–4622, 1999.
- [7] A. Clairon, C. Salomon, S. Guellati, and W. D. Phillips. Ramsey Resonance in a Zacharias Fountain. *Europhysics Letters (EPL)*, 16(2):165–170, 1991.
- [8] Th. Udem, R. Holzwarth, and T. W. Hänsch. Optical frequency metrology. *Nature*, 416:233–237, 2002.
- [9] C. W. Chou, D. Hume, and J. Koelemeij. Frequency comparison of two high-accuracy Al^+ optical clocks. *Phys. Rev. Lett.*, 104:070802, 2010.
- [10] B. J. Bloom, T. L. Nicholson, and J. R. Williams. An optical lattice clock with accuracy and stability at the 10^{-18} level. *Nature*, 506:71–75, 2014.
- [11] J.-S. Chen, S. M. Brewer, and C. W. Chou. Sympathetic Ground State Cooling and Time-dilation Shifts in an $^{27}\text{Al}^+$ Optical Clock. *Phys. Rev. Lett.*, 118:053002, 2017.

- [12] P. Kómár, E. M. Kessler, and M. Bishof. A quantum network of clocks. *Nature Physics*, 10:582–587, 2014.
- [13] J. Wübbena, S. Amairi, O. Mandel, and P.O. Schmidt. Sympathetic cooling of mixed-species two-ion crystals for precision spectroscopy. *Phys. Rev. A - Atomic, Molecular, and Optical Physics*, 85:043412, 2012.
- [14] A. Ludlow, M. Boyd, and J. Ye. Optical atomic clocks. *Rev. Mod. Phys.*, 87:637–701, 2015.
- [15] C. W. Chou, D. Hume, T. Rosenband, and D. Wineland. Optical clocks and relativity. *Science*, 329:1630–1633, 2010.
- [16] T. Rosenband, D. Hume, and C. W. Chou. Alpha-Dot or Not: Comparison of Two Single Atom Optical Clocks. *Proceedings of the 7th Symposium Frequency Standards and Metrology*, pages 20–33, 2012.
- [17] P. K. Ghosh. *Ion Traps*. Oxford University Press, 1996.
- [18] J. P. Home. Quantum Science and Metrology with Mixed-Species Ion Chains. *Advances in Atomic, Molecular and Optical Physics*, 62:231–277, 2013.
- [19] C. Roos. *Controlling the quantum state of trapped ions*. PhD thesis, University of Innsbruck, 2000.
- [20] D. James. Quantum dynamics of cold trapped ions with application to quantum computation. *Applied Physics B-Lasers and Optics*, 66:181–190, 1998.
- [21] C. Roos. Personal communication, 2016.
- [22] D. Leibfried, R. Blatt, C. Monroe, and D. Wineland. Quantum dynamics of single trapped ions. *Rev. Mod. Phys.*, 75:281–324, 2003.
- [23] Claude Cohen-Tannoudji, Bernard Diu and Frank Laloe. *Quantum mechanics*. John Wiley and Sons, 2006.
- [24] C. A. Blockley, D. F. Walls, and H. Risken. Quantum collapses and revivals in a quantized trap. *EPL (Europhysics Letters)*, 17(6):509–514, 1992.
- [25] Mark Fox. *Quantum Optics: An Introduction*. Oxford University Press, 2006.
- [26] H. J. Carmichael. *Statistical Methods in Quantum Optics 1: Master Equations and Fokker-Planck Equations*. Springer, 2002.

-
- [27] G. Lindblad. On the generators of quantum dynamical semigroups. *Comm. Math. Phys.*, 48:119–130, 1976.
- [28] T. Monz. *Quantum information processing beyond ten ion-qubits*. PhD thesis, University of Innsbruck, 2011.
- [29] C. Hempel. *Digital quantum simulation, Schrodinger cat state spectroscopy and setting up a linear ion trap*. PhD thesis, University of Innsbruck, 2014.
- [30] P. Schindler. *Quantum computation and simulation with trapped ions using dissipation*. PhD thesis, University of Innsbruck, 2013.
- [31] D. Kleppner. Norman Ramsey and his method. *Phys. Today*, 66(1):25, 2013.
- [32] P. Jurcevic. *Quantum Computation and Many-body Physics with Trapped Ions*. PhD thesis, University of Innsbruck, 2016.
- [33] J. Benhelm. *Precision spectroscopy and quantum information processing with trapped calcium ions*. PhD thesis, University of Innsbruck, 2008.
- [34] M. Chwalla. *Precision spectroscopy with Ca^+ ions in a Paul trap*. PhD thesis, University of Innsbruck, 2009.
- [35] G. Kirchmair. *Quantum non-demolition measurements and quantum simulation*. PhD thesis, University of Innsbruck, 2010.
- [36] T. Brage, P. Judge, and A. Aboussaïd. Hyperfine Induced Transitions as Diagnostics of Isotopic Composition and Densities of Low-Density Plasmas. *The Astrophysical Journal*, 500:507, 1998.
- [37] P. Staantum, I. Jensen, and R. Martinussen. Lifetime measurement of the metastable $3d\ ^2D_{5/2}$ state in the $^{40}\text{Ca}^+$ ion using the shelving technique on a few-ion string. *Phys. Rev. A*, 69:032503, 2004.
- [38] M. Chwalla, J. Benhelm, and K. Kim. Absolute Frequency Measurement of the $^{40}\text{Ca}^+$ $4s\ ^2S_{1/2}$ - $3d\ ^2D_{5/2}$ Clock Transition. *Phys. Rev. Lett.*, 102:023002, 2009.
- [39] Y. Huang, J. Cao, and P. Liu. Hertz-level measurement of the $^{40}\text{Ca}^+$ $4s\ ^2S_{1/2}$ - $3d\ ^2D_{5/2}$ clock transition frequency with respect to the SI second through the Global Positioning System. *Phys. Rev. A*, 85:030503, 2012.
- [40] K. Matsubara, H. Hachisu, and Yi. Li. Direct comparison of a Ca^+ single-ion clock against a Sr lattice clock to verify the absolute frequency measurement. *Optics Express*, 20:22034–22041, 2012.

- [41] Y. Huang, H. Guan, and P. Liu. Frequency comparison of two $^{40}\text{Ca}^+$ Optical Clocks with an uncertainty at the 10^{-17} Level. *Phys. Rev. Lett.*, 116:013001, 2016.
- [42] G. Tommaseo, T. Pfeil, and G. Revalde. The g_j -factor in the ground state of Ca^+ . *European Physical Journal D*, 25:113–121, 2003.
- [43] M. Ramm, T. Pruttivarasin, and M. Kokish. Precision measurement method for branching fractions of excited $P_{1/2}$ states applied to $^{40}\text{Ca}^+$. *Phys. Rev. Lett.*, 111:023004, 2013.
- [44] F. Diedrich, J. C. Bergquist, W. M. Itano, and D. J. Wineland. Laser cooling to the zero-point energy of motion. *Phys. Rev. Lett.*, 62:403–406, 1989.
- [45] C. Roos, Th. Zeiger, and H. Rohde. Quantum state engineering on an optical transition and decoherence in a paul trap. *Phys. Rev. Lett.*, 83:4713–4716, 1999.
- [46] W. Itano. External-Field Shifts of the $^{199}\text{Hg}^+$ Optical Frequency Standard. *Journal of Research of the National Institute of Standards and Technology*, 105(6):829–837, 2000.
- [47] N. J. Stone. Nuclear Magnetic Dipole and Electric Quadrupole Moments: Their Measurement and Tabulation as Accessible Data. *Journal of Physical and Chemical Reference Data*, 44:031215, 2015.
- [48] T. Rosenband, P.O. Schmidt, and D. Hume. Observation of the $^1\text{S}_0 - ^3\text{P}_0$ clock transition in $^{27}\text{Al}^+$. *Phys. Rev. Lett.*, 98:220801, 2007.
- [49] H. Dehmelt. Mono-Ion oscillator as potential ultimate laser frequency standard. *IEEE Transactions on Instrumentation and Measurement*, 31:83–87, 1982.
- [50] N. Yu, H. Dehmelt, and W. Nagourney. The $3 ^1\text{S}_0 - 3 ^3\text{P}_0$ transition in the aluminum isotope ion $^{26}\text{Al}^+$. *Proceedings of the National Academy of Sciences*, 89:7289, 1992.
- [51] T. Rosenband, W. Itano, and P. O. Schmidt. Blackbody radiation shift of the $^{27}\text{Al}^+ ^1\text{S}_0 - ^3\text{P}_0$ transition. in *Proceedings of the 20th European Time and Frequency Forum*, pages 289–291, 2006.
- [52] T. Rosenband, D. Hume, and P.O. Schmidt. Frequency Ratio of Al^+ and Hg^+ Single-Ion Optical Clocks; Metrology at the 17th Decimal Place. *Science*, 319:1808–1812, 2008.
- [53] E. Träbert and A. Wolf. Measurement of the B^+ and Al^+ intercombination and Sc^{12+} forbidden transition rates at a heavy-ion storage ring. *J.Phys. B.: At. Mol. Opt. Phys.*, 32(2):537, 1999.
- [54] NIST. Atomic Spectra Database.

-
- [55] P. Jönsson. Multi-configuration Hartree- and Dirac-Fock Calculations of Atomic Hyperfine Structures. *Physica Scripta*, 48:678–687, 1993.
- [56] P. Jönsson and C. Froese Fischer. Large-scale multiconfiguration Hartree-Fock calculations of hyperfine-interaction constants for low-lying states in beryllium, boron, and carbon. *Phys. Rev. A*, 48(6):4113–4123, 1993.
- [57] P. Jönsson, C. G. Wahlström, and C. Froese Fischer. A program for computing magnetic dipole and electric quadrupole hyperfine constants from MCHF wavefunctions. *Computer Physics Communications*, 74:399–414, 1993.
- [58] P. Jönsson, F. A. Parpia, and C. Froese Fischer. HFS92: A program for relativistic atomic hyperfine structure calculations. *Computer Physics communications*, 96:301–310, 1996.
- [59] William M. Haynes. *CRC Handbook of Chemistry and Physics 96th Edition*. CRC, New York, 2015.
- [60] W. Itano, J. Bergquist, J. J. Bollinger, and D. Wineland. Quantum projection noise: Population fluctuations in two-level systems. *Phys. Rev. A*, 47:3554–3570, 1993.
- [61] G. Kirchmair. Frequency stabilization of a Titanium-Sapphire laser for precision spectroscopy on Calcium ions. Diploma thesis, University of Innsbruck, 2006.
- [62] H. Nakai, W. Jin, and M. Kawamura. Hyperfine Structure of ^{27}Al by High-Resolution Ultraviolet Laser Spectroscopy. *Jpn. J. Appl. Phys.*, 46(2):815–816, 2007.
- [63] D. Hume. *Two-Species Ion Arrays for Quantum Logic Spectroscopy*. PhD thesis, University of Colorado, 2010.
- [64] Y. Colombe, D. Slichter, and A. Wilson. Single-mode optical fiber for high-power, low-loss UV transmission. *Optics Express*, 22:19783–19793, 2014.
- [65] R. Drever and J. Hall. Laser Phase and Frequency Stabilization Using an Optical Resonator. *Applied Physics B*, 31:97–105, 1983.
- [66] J. L. Hall, M. Taubman, and J. Ye. *Laser Stabilization*. in *Optics Handbook*, Optical Society of America, pp. 27.1-27.24., 2000.
- [67] J. Alnis, A. Matveev, and N. Kolachevsky. Subhertz linewidth diode lasers by stabilization to vibrationally and thermally compensated ultralow-expansion glass Fabry-Perot cavities. *Phys. Rev. A*, 77:053809, 2008.
- [68] M. Schiemangk, S. Spießberger, and A. Wicht. Accurate frequency noise measurement of free-running lasers. *Applied Optics*, 53:7138–7143, 2014.

- [69] L. S. Ma, P. Jungner, J. Ye, and J. L. Hall. Delivering the same optical frequency at two places: accurate cancellation of phase noise introduced by an optical fiber or other time-varying path. *Optics Letters*, 19:1777–1779, 1994.
- [70] G. Domenico, S. Schilt, and P. Thomann. Simple approach to the relation between laser frequency noise and laser line shape. *Applied Optics*, 49:4801–4807, 2010.
- [71] F. M. Mitschke and L. F. Mollenauer. Discovery of the soliton self-frequency shift. *Optics Letters*, 11:659–661, 1986.
- [72] B. Casabone. *Two Ions Coupled to an Optical Cavity : from an Enhanced Quantum Computer Interface towards Distributed Quantum Computing Dissertation*. PhD thesis, University of Innsbruck, 2015.
- [73] M. Guggemos, D. Heinrich, O. A. Herrera-Sancho, R. Blatt, and C. Roos. Sympathetic cooling and detection of a hot trapped ion by a cold one. *New Journal of Physics*, 17(10):103001, 2015.
- [74] D. Berkeland, J. Miller, and J. Bergquist. Minimization of ion micromotion in a Paul trap. *Journal of Applied Physics*, 83(10):5025–5033, 1998.
- [75] P.O. Schmidt, T. Rosenband, and C. Langer. Spectroscopy Using Quantum Logic. *Science*, 309:749–752, 2005.
- [76] J. H. Wesenberg, R. J. Epstein, and D. Leibfried. Fluorescence during Doppler cooling of a single trapped atom. *Phys. Rev. A - Atomic, Molecular, and Optical Physics*, 76:053416, 2007.
- [77] A. A. Madej, J. E. Bernard, and P. Dubé. Absolute frequency of the $^{88}\text{Sr}^+$ $5s\ ^2\text{S}_{1/2}$ - $4d\ ^2\text{D}_{5/2}$ reference transition at 445 THz and evaluation of systematic shifts. *Phys. Rev. A - Atomic, Molecular, and Optical Physics*, 70:012507, 2004.
- [78] G. P. Barwood, H. S. Margolis, and G. Huang. Measurement of the Electric Quadrupole Moment of the $4d\ ^2\text{D}_{5/2}$ Level in $^{88}\text{Sr}^+$. *Phys. Rev. Lett.*, 93:133001, 2004.
- [79] P. Dube, A. Madej, Z. Zhou, and J. Bernard. Evaluation of systematic shifts of the $^{88}\text{Sr}^+$ single-ion optical frequency standard at the 10^{-17} level. *Phys. Rev. A - Atomic, Molecular, and Optical Physics*, 87:023806, 2013.
- [80] I. I. Sobelman. *Atomic spectra and radiative transitions*. Springer Series on Atoms and Plasmas, 1992.
- [81] Y. Yu, B. Suo, and H. Fan. Finite-field calculation of the polarizabilities and hyperpolarizabilities of Al^+ . *Phys. Rev. A*, 88:052518, 2013.

- [82] C. Seck, E. Hohenstein, and C. Lien. Rotational state analysis of AlH^+ by two-photon dissociation. *Journal of Molecular Spectroscopy*, 300:108–111, 2014.
- [83] D. Hume, C. W. Chou, and D. R. Leibbrandt. Trapped-ion state detection through coherent motion. *Phys. Rev. Lett.*, 107:243902, 2011.
- [84] Peter J. Mohr, David B. Newell, and Barry N. Taylor. CODATA Recommended Values of the Fundamental Physical Constants: 2014. *Rev. Mod. Phys.*, 88:1527–1605, 2016.

Acknowledgements

Setting up a new ion trapping experiment with two ion species in a formerly empty laboratory is certainly an uncomfortable way to do a PhD. Retrospectively I can say that it was once more worth going down the more difficult road. As my PhD comes to its end the foundation for an optical frequency standard in Innsbruck based on aluminium and calcium ions was laid. Since this work would not have been possible without the help of many people inside and outside the institute I will take the opportunity to thank all of them for their contribution.

First, I want to thank Rainer Blatt for receiving me in his group and for his confidence in my work. He let me free in setting up the experiment according to my perceptions, which was an enriching experience for me.

Second, I want to thank Christian Roos for co-supervising this work. Many interesting discussions and especially his theoretical support greatly contributed to the experimental results.

Moreover I want to thank all my colleagues in the group who helped with words and deeds. Especially I want to thank Daniel Heinrich for many important contributions, primarily on the experimental control. I also want to thank the people from the quantum simulation experiment in lab 1 for providing stable 729 nm light. My successor Milena Guevara-Bertsch, who joined the group at the end of my PhD, has already made useful contributions to the last achievements of this work.

Furthermore I want to thank Piet Schmidt for all the friendly communication and for sharing a lot of useful information about the aluminium ion. In addition I want to thank Jook Walraven for improving my understanding in atomic physics.

Moreover I want to thank my office mate Ben Lanyon for many funny and interesting conversations as well as for improving my English skills.

Building the experimental setup involved the guys from the fine-mechanical and electrical workshops, namely Stefan Haslwanter, Gerhard Hendl, Andreas Strasser and Bernhard Öttl. The collaboration with them brightened everyday life.

I also want to thank the people responsible for the administrative tasks namely Markus Knabl, Doris Corona, Elisabeth Huck, Patricia Moser, Nikolaus Falschlunger, Valentin Staubmann and David Jorda.

Furthermore I want to thank the guys who joined me stopping by at a pub for many funny and interesting conversations.

Very important to me is to balance work and recreation. Alpinism is not only a hobby for

me but more a way of life. Big up to my friends for many unforgettable adventures in the mountains.

Finally, I want to express my gratitude to my parents for all their support and encouragement.

“The struggle itself (towards the heights) is enough to fill a man’s heart. One must imagine Sisyphus happy.” - Albert Camus